

Numerical Analysis of Turbulent Flow around the Ship Hulls using STAR-CCM+

By

Doyal Kumar Sarker

Student ID: 1017122003

Submitted to the

Department of Naval Architecture and Marine Engineering

In partial fulfillment of the requirements for the degree of

MASTER OF SCIENCE

in

Naval Architecture and Marine Engineering



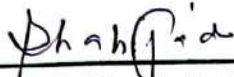


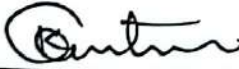

Bangladesh University of Engineering and Technology, (BUET)

6th June, 2021

Certificate of Approval

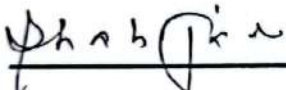
The thesis titled "Numerical Analysis of Turbulent Flow around the Ship Hulls using STAR-CCM+" submitted by Doyal Kumar Sarker, Student ID: 1017122003, Session: October, 2017 to the Department of Naval Architecture and Marine Engineering, Bangladesh University of Engineering and Technology (BUET), Dhaka-1000, Bangladesh has been accepted as satisfactory in partial fulfillment of the requirements for the degree of Master of Science in Naval Architecture and Marine Engineering on 6th June, 2021.

Board of Examiners

- 
1. **Dr. Md. Shahjada Tarafder** Chairman
Professor (Supervisor)
Department of Naval Architecture and Marine Engineering
Bangladesh University of Engineering and Technology, Dhaka
- 
2. **Head** Member
Department of Naval Architecture and Marine Engineering (Ex-Officio)
Bangladesh University of Engineering and Technology, Dhaka
- 
3. **Dr. Md. Mashud Karim** Member
Professor
Department of Naval Architecture and Marine Engineering
Bangladesh University of Engineering and Technology, Dhaka
- 
4. **Dr. Goutam Kumar Saha** Member
Professor
Department of Naval Architecture and Marine Engineering
Bangladesh University of Engineering and Technology, Dhaka
- 
5. **Dr. Mohammad Ali** Member
Professor (External)
Department of Mechanical Engineering
Bangladesh University of Engineering and Technology, Dhaka

Certificate of Research

This is to certify that the candidate has done this work and it was not submitted elsewhere for the award of any degree or diploma.



Supervisor

Dr. Md. Shahjada Tarafder
Professor
Department of Naval Architecture and Marine Engineering (NAME)
Bangladesh University of Engineering and Technology (BUET)
Dhaka 1000, Bangladesh

Declaration

I do hereby declare that I, the candidate, have done this work and it was not submitted elsewhere for the award of any degree or diploma.

Signature of the Candidate

Doyal Kumar

Doyal Kumar Sarker

Student ID: 1017122003

Dedicated To

*My Beloved Parents
and Respected Teachers*

Acknowledgement

I would like to express my profound gratitude to my thesis supervisor Dr. Md. Shahjada Tarafder, Professor of the department of Naval Architecture and Marine Engineering, Bangladesh University of Engineering and Technology, Dhaka for giving me the opportunity to work on a very interesting topic. Without his continuous support, ideas, guidelines and encouragements this challenging work would not have been possible to be completed successfully.

I want to thank Dr. Goutam Kumar Saha, Professor of the department of Naval Architecture and Marine Engineering, for giving me the chance to use the necessary computer resources during my thesis work.

I am also thankful to Srikanth Swamy, support engineer at CD-adapco for his valuable suggestions and guidelines throughout this study and also his assistance with the commercial CFD code STAR-CCM+.

I would like to thank all others who are directly or indirectly related to this thesis by sharing their ideas, suggestions and thus supporting us. Finally, I am grateful to my parents and other family members for their constant encouragement and support.

Doyal Kumar Sarker

6th June, 2021

Abstract

The analyses of turbulent flow around the ship hulls which include Wigley hull, Kriso container ship (KCS), Series 60, HSVA tanker and a catamaran hull are conducted for various Froude numbers using a commercial computational fluid dynamics (CFD) code STAR-CCM+. The finite volume method (FVM) is employed to discretize the governing equations of fluid flow and the SIMPLE (semi-implicit method for pressure linked equations) algorithm is applied to get the solution of pressure-velocity coupling equations. The k - ε turbulence model is chosen to give the closure to the Reynolds Averaged Navier Stokes (RANS) equations and the volume of fluid (VOF) method is applied to capture the interface between the two phases. Dynamic fluid body interaction (DFBI) module is used to simulate the motion of rigid body (ship hull) which is unconstrained to sink and trim. A trimmed cell mesher technique is used to produce hexahedral cell and prism layer mesher model is applied to resolve the turbulent flow accurately near the solid wall of the hulls.

The present numerical results (wave profile, wave pattern and resistance) obtained from STAR CMM+ for each mono hull are compared with those of its available experimental results and the agreement is found to be quite satisfactory. The sinkage and trim are calculated only for Wigley and KCS hull and are compared with the experiment. The predicted wave pattern is composed of transverse and diverging waves and looks very similar to Kelvin wave pattern. Moreover, the grid dependency study is carried out for Wigley, KCS and Series 60 hulls and as expected the finer are the grids, the better is the accuracy found with a cost of longer computation time.

In case of catamaran, the wave-making resistance of the catamaran hull exhibits broadly similar trends to those of the published monohull results as well as the experiment. However, the magnitude of the wave elevation of the inner side of the catamaran hull is slightly higher than that of the outer side at the first crest of the bow. This difference is mainly due to the wave-interference effects.

Above all, the standard two-equation k - ε turbulence model with near-wall function is used to predict the turbulent flow characteristics which are very close to experimental results and could be considered as a powerful tool for analyzing the viscous fluid flow.

Table of Contents

Certificate of Approval	ii
Certificate of Research	iii
Declaration	iv
Acknowledgement	vi
Abstract	vii
Table of Contents	viii
List of Figures	xi
List of Tables	xiv
Nomenclature	xv
Chapter 1: Introduction	1
1.1 Background	1
1.2 Literature Review	1
1.3 Objectives of the Thesis	5
1.4 Thesis Structure.....	6
Chapter 2: Mathematical Modeling of Flow around Ship Hull	7
2.1 Reynolds Averaged Navier-Stokes Equations	7
2.2 Turbulence Modeling	12
2.2.1 $k-\varepsilon$ Turbulence Model	15
2.3 Near Wall modeling and wall function	16
2.4 Free-Surface Flows	18
2.5 Hull Resistance.....	19
2.6 Hull Induced Waves	20
2.7 Rigid Body Dynamics	21
2.7.1 Sinkage and Trim.....	22
Chapter 3: Numerical Methods	24
3.1 Discretization Process	24

3.1.1	Geometric and Physical Modeling.....	24
3.1.2	Domain Discretization	24
3.2	Discretization of Governing Equations by FVM	25
3.3	Solution of Discretized Equations.....	29
3.4	Collocated Grid Arrangement	29
3.5	Semi Implicit Method for Pressure –Linked Equation (SIMPLE).....	30
3.5.1	Solution Algorithm	33
3.6	Convergence.....	37
3.7	Grid Dependence and Validation	38
3.7.1	Grid Dependence Test.....	39
3.7.2	Validation Procedure	40
Chapter 4:	Computational Setup	41
4.1	Co-ordinate System	41
4.2	Boundary Conditions.....	41
4.3	Mesh Generation	43
4.3.1	Surface Mesh	44
4.3.2	Volume Mesh.....	45
4.4	Physics Modeling	49
4.4.1	Space Modeling	49
4.4.2	Time Modeling.....	49
4.4.3	Materials Modeling.....	49
4.4.4	Multiphase Flow Modeling.....	50
4.4.5	VOF Waves.....	51
4.4.6	Turbulence Modeling.....	52
4.4.7	Wall Treatment Modeling.....	53
4.5	DFBI Modeling	55
4.6	Solver Setting	55

Chapter 5: Results and Discussions	57
5.1 Wigley Hull	57
5.2 KCS Hull	70
5.3 Series 60 Hull	82
5.4 HSVA Tanker.....	88
5.5 Catamaran Hull	91
Chapter 6: Conclusions	96
References	97
Appendix A	I
Derivation of Turbulent Kinetic Energy, k	I
Appendix B	I
Numerical Scheme to predict Body Motion.....	I
Appendix C	VIII
Residual Convergence.....	VIII
Appendix D	X
Time History of Resistance	X
Appendix E	XIII
Outline of Simulation Setup.....	XIII

List of Figures

Fig. 2.1: Boundary layer velocity profile [29] -----	16
Fig. 2.2: The bow and stern wave systems [32]-----	20
Fig. 2.3: Representation of Ship motion with 6 DOF [30] -----	21
Fig. 3.1: A three dimensional control volume with CVs face [40]-----	25
Fig. 3.2: Illustration of an implicit method [25] -----	28
Fig. 3.3: Collocated grid arrangement of velocity componenets [25] -----	30
Fig. 3.4: Nodal indexing of elemental cell in three dimensions [25] -----	30
Fig. 3.5: Solution algorithm of Transient SIMPLE Scheme [25, 36]-----	36
Fig. 4.1: Coordinate system used in this present study -----	41
Fig. 4.2: Computational domain and its boundary conditions -----	42
Fig. 4.3: Surface mesh of the computational domain -----	44
Fig. 4.4: Surface mesh of the KCS hull -----	45
Fig. 4.5: Finite volume mesh applied to the domain and hull model -----	46
Fig. 4.6: Refined mesh scene at the free surface-----	47
Fig. 4.7: Mesh applied at the bow and stern regions -----	47
Fig. 4.8: Generated prism layers with the core mesh-----	48
Fig. 4.9: Iso surface generated by multiphase modeling-----	50
Fig. 4.10: Free surface at initialization stage of simulation. -----	51
Fig. 5.1: Computational Domain of Wigley Hull-----	58
Fig. 5.2: Mesh structure for flow computation domain -----	58
Fig. 5.3: Grid distribution on the surface of Wigley hull -----	59
Fig. 5.4: Comparison of total resistance coefficient for Wigley hull.-----	60
Fig. 5.5: Comparison of sinkage and trim for Wigley hull -----	61
Fig. 5.6: Pressure distribution over the surface of Wigley hull -----	62
Fig. 5.7: Wave profile along the Wigley mono hull with experimental results.-----	63
Fig. 5.8: Kelvin Wave pattern at different Froude numbers for Wigley hull -----	64
Fig. 5.9: Kelvin Wave pattern comparison for Wigley hull-----	65
Fig. 5.10: Grid dependency on wave profile of Wigley hull -----	69
Fig. 5.11: Computational Domain of KCS hull -----	71
Fig. 5.12: Mesh structure of flow computation domain -----	71
Fig. 5.13: Grid Distribution on the KCS hull-----	72
Fig. 5.14: Convergence history of Resistance of KCS hull at $Fn = 0.26$ -----	72

Fig. 5.15: Comparison of total resistance coefficients of KCS hull. -----	73
Fig. 5.16: Comparison of (a) Sinkage and (b) Trim for KCS hull -----	74
Fig. 5.17: Pressure distribution over the surface of Wigley hull -----	76
Fig. 5.18: Kelvin Wave pattern for KCS hull at different Froude numbers-----	77
Fig. 5.19: Comparison of Kelvin wave pattern of KCS hull between CFD (bottom) and EFD (top) -----	78
Fig. 5.20: Wave profile along the KCS hull -----	78
Fig. 5.21: Transverse wave cut of KCS hull-----	79
Fig. 5.22: Grid dependency study of wave profile for KCS hull -----	81
Fig. 5.23: Grid distribution on the surface of Series 60 hull -----	82
Fig. 5.24: Mesh structure for flow computation of Series 60 hull-----	83
Fig. 5.25: Comparison of total resistance coefficient of Series 60 hull-----	83
Fig. 5.26: Wave profile along the Series 60 hull at different Froude numbers -----	84
Fig. 5.27: Kelvin Wave pattern for Series 60 hull at different Froude numbers -----	85
Fig. 5.28: Comparison of wave pattern between Huang[57] (Left) and present study (Right)	86
Fig. 5.29: Grid dependency on wave profile for Series 60 hull-----	87
Fig. 5.30: Surface mesh on the HSVA Tanker-----	88
Fig. 5.31: Computational domain of HSVA Tanker -----	89
Fig. 5.32: Mesh structure for flow computation of HSVA Tanker-----	89
Fig. 5.33: Comparison of total resistance coefficient for HSVA tanker-----	90
Fig. 5.34: Wave profile along the HSVA hull at different Froude numbers -----	90
Fig. 5.35: Computational domain of the wigley catamaran hull-----	91
Fig. 5.36: Volume mesh with refinement at the hull separation and wake region -----	92
Fig. 5.37: Wave resistance coefficient comparison of Wigley catamaran hull-----	92
Fig. 5.38: Kelvin Wave pattern at different Froude numbers of Wigley catamaran ($s/L= 0.4$) -----	93
Fig. 5.39: Wave profile along the Wigley catamaran hull ($s/L= 0.4$)-----	94
Fig. 5.40: Pressure distribution on the surface of Catamaran hull -----	95
Fig. C.1: Residual convergence of Wigley hull-----	VIII
Fig. C.2: Residual convergence of KCS hull-----	VIII
Fig. C.3: Residual convergence of Series 60 hull -----	VIII
Fig. C.4: Residual convergence of HSVA tanker hull -----	VIII
Fig. C.5: Residual convergence of Wigley catamaran hull-----	VIII
Fig. D.1: Time history of Total, Residual and Frictional Resistance of Wigley hull-----	X

Fig. D.2: Time history of Total, Residual and Frictional Resistance of KCS hull----- X
Fig. D.3: Time history of Total Resistance of Series 60 hull ----- XI
Fig. D.4: Time history of Total, Residual and Frictional Resistance of Catamaran hull----- XII

List of Tables

Table 4.1: Overall thickness of a prism layer for KCS.....	48
Table 4.2: Material properties for multiphase modeling	50
Table 5.1: Main Particulars of Wigley Hull.....	57
Table 5.2: Relative error analysis of resistance coefficient for Wigley hull	61
Table 5.3: Grid properties for CT, CF, and CW	66
Table 5.4: Grid convergence study of CT, CF, and CW for Wigley hull.....	66
Table 5.5: Verification of CT, CF, and CW for Wigley hull	68
Table 5.6: Validation of CT, CF, and CW for Wigley hull.....	69
Table 5.7: Grid convergence study of wave profile for Wigley hull	70
Table 5.8: Verification and validation of wave profile for Wigley hull	70
Table 5.9: Main particulars of KCS hull form	70
Table 5.10: Relative error analysis of total resistance coefficient for KCS hull	74
Table 5.11: Relative error analysis of Sinkage and Trim for KCS hull.....	75
Table 5.12: Grid properties for CT, Sinkage, and Trim	79
Table 5.13: Grid convergence study for CT, Sinkage, and trim for KCS hull	80
Table 5.14: Verification of CT, Sinkage, and trim for KCS hull	80
Table 5.15: Validation of CT, Sinkage, and trim for KCS hull.....	81
Table 5.16: Main Particulars of Series 60 Hull.....	82
Table 5.17: Grid properties for CT at $F_n = 0.30$	86
Table 5.18: Grid convergence study for CT Series 60 hull.....	86
Table 5.19: Verification of CT for Series 60 hull	87
Table 5.20: Validation of CT for Series 60 hull.....	87
Table 5.21: Main Particulars of HSVA.....	88

Nomenclature

Acronyms

Symbol	Description
<i>CFD</i>	Computational Fluid Dynamics
<i>CDS</i>	Central Differencing Scheme
<i>CVs</i>	Control Volumes
<i>DFBI</i>	Dynamic Fluid Body Interaction
<i>DNS</i>	Direct Numerical Simulation
<i>DOF</i>	Degree of Freedom
<i>EFD</i>	Experimental Fluid Dynamics
<i>FVM</i>	Finite Volume Method
<i>GCI</i>	Grid Convergence Index
<i>HSVA</i>	Hamburgische Schiffbau Versuchsanstalt / Hamburg Ship Model Basin
<i>ITTC</i>	International Towing Tank Conference
<i>KCS</i>	KRISO Container Ship
<i>KRISO</i>	Korean Institute of Ships and Ocean Engineering
<i>LES</i>	Large Eddy Simulation
<i>QUICK</i>	Quadratic Upstream Interpolation for Convective Kinematics
<i>RANSE</i>	Reynolds Averaged Navier Stokes Equations
<i>RE</i>	Richardson Extrapolation
<i>SIMPLE</i>	Semi Implicit Method for Pressure Linked Equations
<i>SST</i>	Shear Stress Transport
<i>VOF</i>	Volume of Fluid
<i>V&V</i>	Verification and Validation

Roman Symbols

Symbol	Description	Unit
<i>AP</i>	Aft Perpendicular	[–]
<i>B</i>	Beam of the Ship	[<i>m</i>]
<i>C_B</i>	Block Coefficient	[–]
<i>C_F</i>	Frictional Resistance	[–]

C_O	Courant Number	$[-]$
C_P	Pressure Coefficient	$[-]$
C_R	Residuary Coefficient	$[-]$
C_T	Total Resistance Coefficient	$[-]$
C_W	Wave Resistance Coefficient	$[-]$
C_μ	Eddy Viscosity Coefficient	$[-]$
$C_{\varepsilon 1}, C_{\varepsilon 2}$	Constant in Turbulence Model	$[-]$
D	Depth	$[m]$
FP	Forward Perpendicular	$[-]$
F_n	Froude Number	$[-]$
g	Gravitational Acceleration	$[ms^{-2}]$
I_{xx}, I_{yy}, I_{zz}	Moment of Inertia	$[kgm^2]$
I_{xy}, I_{yz}, I_{zx}	Product of Inertia	$[kgm^2]$
J	Jacobian Transformation	$[-]$
k	Turbulent Kinetic Energy	$[m^2s^{-2}]$
L	Characteristic Length	$[m]$
L_{PP}	Length Between Perpendiculars	$[m]$
p	Pressure	$[Pa]$
\bar{p}	Average Pressure	$[Pa]$
p'	Fluctuating Pressure	$[Pa]$
Q	Production of Turbulent Kinetic Energy	$[-]$
r_i	Grid Refinement Ration	$[-]$
R_T	Total Resistance	$[N]$
R_F	Frictional Resistance	$[N]$
R_R	Residuary Resistance	$[N]$

R_k	Convergence Ratio	$[-]$
R_n	Reynolds Number	$[-]$
S_{wet}	Hull Wetted Surface Area	$[m^2]$
S	Simulation Result	$[-]$
S_ϕ	Source Term	$[-]$
T	Draft	$[m]$
t	Time	$[sec]$
\mathbf{U}	Velocity Vector	$[m/s, m/s, m/s]$
u	Velocity Component	$[m/s]$
u^+	Dimensionless Velocity	$[-]$
u_*	Friction Velocity	$[m/s]$
U_{SN}	Numerical Uncertainty	$[-]$
U_I	Iterative Uncertainty	$[-]$
U_G	Grid Uncertainty	$[-]$
y	Distance to Wall	$[m]$
y^+	Non-Dimensional Wall Distance	$[-]$

Greek Symbols

Symbol	Description	Unit
α	Constant	$[-]$
Δ	Displacement	$[N]$
Δt	Time Step	$[sec]$
$\Delta x, \Delta y, \Delta z$	Grid Spacing	$[m]$
ε	Dissipation Rate of Turbulent Kinetic Energy	$[m^2 / s^3]$
μ	Dynamic Viscosity	$[Nsm^{-2}]$
μ_t	Turbulent Viscosity	$[Nsm^{-2}]$

ν	Kinematic Viscosity	$[m^2 / s]$
ρ	Fluid Density	$[kg / m^3]$
τ_w	Wall Shear Stress	$[Pa]$
ϕ	Transport Variable	$[-]$
κ	Von Karman Constant	$[-]$
τ_{ij}	Viscous Stress Term	$[Pa]$
Γ	Diffusion Coefficient	$[-]$
σ	Sinkage	$[m]$
φ	Roll Angle	$[deg]$
θ	Trim Angle	$[deg]$
ψ	Yaw Angle	$[deg]$
δ	Boundary Layer Thickness	$[m]$
δ_{RE}	Grid Discretization Error	$[-]$

Chapter 1

Introduction

1.1 Background

The recent advances in Computational Fluid Dynamics (CFD) for incompressible flow are gradually proving to be invaluable asset for design and analysis of ship, submarines, underwater missiles, low speed transport aircrafts and a wide variety of equipment design in process industry. Accurate prediction of turbulent flow is of great practical interest in the overall performance of ship hull to be designed. The ship hull advances in water continuously incorporate with air and water and a free surface generated between these two phases. The surface wave due to the existence of this free surface, the presence of turbulent boundary layers are very common characteristics for which the flow around the ship hull is being extremely complicated and the hydrodynamic behaviors of a ship hull are significantly related to the surrounding flows [1]. Modeling the flow taking the turbulence effects into account to evaluate the hydrodynamic performance of the concepts is always being a prioritize research area in the ship engineering and academia.

Towing tank test is performed to analyze the hydrodynamic performance like resistance, sinkage, trim, wave profile etc. at corresponding speeds, which are crucial to establishing reliable propulsive power from the ship design viewpoint and this test method is more accurate and reliable. But there are some challenging areas like the readily available towing tank and the cost associated with the towing test are common. The towing tank flow characteristics differ from full scale and also prediction full-scale performance from towing tank at equivalent Froude number is challenging. The rapid technological advances of CFD resources are implemented for the development of high-performance hull forms under the realistic rough environment conditions. Numerical predictions also assure a new era of design and optimization by providing a great deal of information on the flow with considerably fewer resources and time [2]. These achievability motivates to use the CFD tool to investigate the complex flow characteristics which govern a lot of key factors over the body like resistance, sea keeping analysis.

Providing a great detail of flow fields, the CFD tool solves the viscous flow problems by offering both model ship and full scale results. Several viscous flow approximations in ship engineering field such as Direct Numerical Simulation (DNS), Large Eddy Simulation (LES),

and Reynolds Averaged Navier Stokes (RANS) have emerged with increasing computing power. Among these but not limited to, for the analyses of the turbulent flow over the ship hull, the RANS approximation is the most computationally efficient and a common technique for evaluating the ship hydrodynamic behaviors. To ensure the quality of the applied approximation method, a systematic approach like the comparison between computation and experiment could be a favorable way [2].

The study is focused on the investigation of the turbulent flow around the ship hulls including the **mono and multi hulls** (Wigley, KCS, Series 60, HSVA Tanker and Catamaran hulls). Finite volume method (FVM) based commercial CFD software STAR-CCM+ is used to perform the whole simulation and SIMPLE (semi-implicit method for pressure linked equations) algorithm is applied to get the solution of pressure-velocity coupling equations. $k - \varepsilon$ two equations turbulence model is used to give the closure of Reynolds Averaged Navier Stokes (RANS) equation to extract the velocity and pressure fields. Volume of Fluid (VOF) multiphase model is implemented to determine the position of free surface between air and water phases.

1.2 Literature Review

The understanding of the physics of fluid turbulence is far from complete and Reynolds Averaged Navier Stokes (RANS) methodology coupled to statistical turbulence model is often very useful and reliable for computation of statistically stationary turbulent flows. Modeling the turbulence in order to close the RANS equations has been paid much attention. However, there is no single turbulence model which can predict reliably all kinds of turbulent flows. Every model have its own pros and cons. The **$k - \varepsilon$ model** [3-4] is the most widely known and extensively used two-equation eddy viscosity model. In case free shear layer flows with relatively small pressure gradients, this model has given good results. The transport equations for this model are solved to get two scalar properties: the turbulent kinetic energy, k and the dissipation rate (ε) of the turbulent kinetic energy. To define the eddy viscosity function another two equation **$k - \omega$ model** [3-4] was originated in parallel with the prior turbulence model. This model shows a good settlement with experiment in the logarithmic region of the boundary layer profile for trivial adverse pressure gradient flows. However, it is difficult to implement enough control over the local free stream turbulence to avoid small free stream dissipation rate of this model, ω in the complex Navier-Stokes computation and consequently, haziness arise in the predicted results. When flow separation is expected, the **shear stress**

transport (SST) model [5] modify the turbulent eddy viscosity function to improve the prediction of separated flows. A serious deficiency occurs in two equation models: under predict the retardation and separation of the boundary layer due to adverse pressure gradients. This deficiency can be mitigated by modeling the transport of the shear stress as being proportional to that of the turbulent kinetic energy. The **One equation turbulence** [6] (Spalarts-Allamaras) model provide a simpler alternative to two equation turbulence models. For 2-D mixing layer, wake flow, flat boundary layers this model gives reasonably good predictions [7].

Azcueta [8] computed turbulent free-surface flows around ships and floating bodies where for modeling turbulence, the standard k-epsilon model with wall function was applied. To locate the free surface, the volume of fluid (VOF), an interface-capturing method was used. It was found that total resistance for the Series-60 model in free condition was 10% larger than in fixed condition.

Adjali et al. [9] numerically simulated free surface water waves generated by moving bodies. Turbulence was modeled using the shear stress k-omega SST model and the free surface motion was simulated by volume of fluid technique. Numerically obtained results were compared well with the experimental data.

Tarafder and Mursaline [10] simulated two dimensional steady viscous flow past the circular and circular cylinder at low Reynolds numbers. To reduce the computational cost, a simplified pressure correction was extracted and appropriate under-relaxation factors were used. The solution of the governing equations of the flow was carried out using SIMPLE algorithm. From the numerical results of bubble length, separation angle, total drag in case of square and circular cylinders, it was found that square shaped cylinder is more bluff than a circular one.

Tarafder and Mursaline [11] simulated the turbulent flow around two-dimensional bodies using the finite volume method with non-orthogonal body fitted grid. The k - ϵ turbulence model and wall functions were used to bridge the solution variables at the near wall cells and the corresponding quantities on the wall. The solution was carried out using the SIMPLE algorithm with a simplified pressure correction equation for collocated arrangement for scalar and vector variables.

Zhao et al. [1] studied viscous flow around the hull with free surface solving the Reynolds-Averaged Navier-Stokes (RANS) equations. The agreement between numerical and

experimental results indicated that the CFD model is capable to simulate the viscous flows around the ship hulls with an acceptable accuracy level.

Pranzitelli et al. [12] simulated free surface flow around a semi-displacing motor yacht advancing steadily in calm water. The volume of fluid method (VOF) was implemented in Reynolds-Averaged Navier-Stokes (RANS) equations and this VOF method correctly predicted both the free surface shape and the total resistance.

Perez et al. [13] validated resistance and wave profile at six Froude numbers with the application of CFD code ANSYS-CFX 11.0. The study showed a good agreement for resistance, but the wave profiles along the hull were not in satisfactory level. To determine the suitable turbulence model for the highest and lowest Froude numbers, a statistical hypothesis test was conducted. For the lowest Froude number, 0.25, better agreement in resistance prediction was found using $k - \varepsilon$ model while for the highest Froude number, 0.408, satisfactory result was found applying the $k - \omega$ model followed by the SST.

Karim et al. [14] studied effect of free surface waves and wave induced separation on a 3D surface piercing rudder with NACA 0012, 0018, 0024 airfoils using CFD code ANSYS Fluent. The SST $k - \omega$ turbulence model captured the boundary layer and volume of fluid (VOF) method tracked the free surface successfully. The research indicated that at the higher Froude number wave patterns are dependent on the Froude number rather than thickness of the body.

Karim and Naz [15] investigated the viscous flow the ship hull while the propeller action was taken into consideration. Firstly, the bare hull condition was focused to predict the free surface elevation and the resistance components. A zonal approach with the solver was applied at the three zones: “potential flow solver”, “boundary layer solver” and “Navier-Stokes solver” in the region outside the boundary layer and wake, the thin boundary layer near to the ship hull, and wake region respectively.

Ozdemir et al. [16] performed a CFD analysis to simulate free surface flow around the KCS hull using $k - \varepsilon$ turbulence model where the RANS equations and non-linear free surface boundary conditions were discretized with the aid of finite volume scheme. To create the solution domain, an unstructured mesh was generated. The calculated total resistance coefficient for the finer grid was satisfactory with the margin of 2.77% of the experimental one and Residual resistance coefficient was calculated with an error of 7.45% for fine grid. The $k - \varepsilon$ turbulence model provided good results in fully turbulent free surface flows around the ships.

Ahmed [17] used RANSE code CFX to simulate the incompressible turbulent free surface flow around the complex hull form DTMB 5415 at two different speeds. The standard $k - \varepsilon$ model was used in the CFX model and to build the hybrid grid for the RANSE code solver, a grid generator ICEM CFD was applied. In the computational grid generation, the domain was meshed with structured hexahedral grid while the hull surface was meshed with unstructured tetrahedral grid.

Wang and Walter [18] performed simulations of marine propeller using a transition-sensitive turbulence model to better resolve the propeller flow characteristics. Fully turbulent flow simulations were also performed for comparison purposes at various propeller load conditions. Results showed that the applied transition-sensitive turbulence model is better able to resolve blade-surface stresses, flow separations, and tip-vortex originations, and consequently, improve the prediction accuracy in propeller performance, especially under high-load conditions.

Karim et al. [19] simulated the surface wave generated by flow around submerged hydrofoils at different depth to compute wave amplitude, lift and drag. Volume of fluid (VOF) technique was used to determine the free surface effect of the water and the Semi Implicit Method for Pressure Linked Equations-Consistent (SIMPLEC) was implemented for pressure-velocity coupling. The discretization of momentum, volume fraction, turbulent kinetic energy, and turbulent dissipation rate was carried out by second order upwind scheme.

Chao-bang and Wen-cai [20] calculated the resistance of a high-speed displacement ship taking the effect of sinkage and trim and viscosity of fluid into account. A free surface flow field was evaluated by solving Reynolds averaged Navier-Stokes (RANS) equations with volume of fluid (VOF) method. The sinkage and trim were computed by equating the vertical force and pitching moment to the hydrostatic restoring force and moment.

Tu et al. [21] predicted ship resistance, sinkage and trim in calm water by using unsteady RANS method. Grid convergence study was also carried out to determine the grid effect on the results. The resistance coefficient was well agreed with experiment, but the obtained trim and sinkage differed more from the experiment.

In the field of naval architecture, one of the major challenges to extract the resistance components of catamaran hull is the effect of complex wave interference between the two demi hulls. The selection of the hull form, separation between the mono hulls are consideration factor in predicting the hydrodynamic behaviors including resistance, sinkage, and trim. Insel and

Molland [22] investigated the total resistance components, trim, sinkage, and wave pattern of mathematically defined Wigley hull form for a wide range of Froude numbers taking different hull separation to length ratios. These results are extensively used as experimental reference data for many numerical studies.

To clarify the characteristics of flow field around the high speed catamaran in calm water, a numerical study was conducted by Kwag [23]. Free surface with nonlinearity condition in Navier-Stokes solver was applied and the grid generation was based on Marker and Cell method in the computation. The extracted results depicted that at the low hull separation value, the wave interference becomes stronger and at the high hull separation, the wave interference almost diminish that looks like to the wave pattern of the mono hull. Wave resistance coefficient showed a good agreement with experimental data.

Tarafder and Suzuki [24] solved a non-linear free surface flow problem for Wigley catamaran hull using potential based boundary element method. Mono hulls were considered as lifting body due to the difference between the interior flow and exterior flow of each mono hull. At the bow side, the inner region wave profile has been found higher than the outer region wave profile. This was resulted from the wave interference between the hulls. The wave resistance coefficients were calculated for three different hull separation to length ratios ($s/L = 0.2, 0.3, 0.4$) at the Froude numbers ranging 0.2-1.0 and found acceptable trends to those published literatures.

1.3 Objectives of the Thesis

The objectives of the present research are as follows:

- i. To compute the resistance of different types of mono hulls (Wigley, Series 60, KCS and HSV A tanker) and multi-hulls (Catamaran) using STAR-CCM+.
- ii. To compute the sinkage, trim and wave pattern around the aforesaid hulls.
- iii. To validate the computed results with the available experimental results.
- iv. To study the uncertainty of the computed results.

1.4 Thesis Structure

The thesis is organized in the following way. There are total 6 (Six) chapters in this thesis. The **current chapter** presents a general background providing the motivation, the review some of the published literatures, and the objectives of the present work.

In the **chapter 2**, a complete set of governing equations for modeling the fluid flow, turbulence modeling, and the rigid body dynamics are explained.

In the **chapter 3**, a general transport equation is developed and a numerical scheme is applied to discretize that equation. The solution algorithm for the discretized equation is discussed in details. In the same chapter, total verification and validation (V&V) studies are mentioned.

In the **chapter 4**, the total simulation set up in the STAR-CCM+ are described. The set-up processes started from the defining the coordinate system, computational domain creation, defining the boundary conditions, mesh generation, physics modeling and the solver setting.

In the **chapter 5**, results of total resistance coefficients, wave profile, and wave patterns for four mono hulls (Wigley, KCS, Series 60, and HSV A tanker) are presented and compared with those of its available experimental results. Sinkage and trim are calculated only for the Wigley and KCS hulls and presented in this chapter as well. Moreover, verification and validation (V&V) studies are performed in case of Wigley, KCS and Series 60 hull which are also discussed in the chapter 5. The wave making resistance for the Wigley catamaran hull, inner and outer wave profile along the hull are extracted and presented in this chapter.

Finally, in the **chapter 6**, a conclusion of the whole thesis is offered.

Chapter 2

Mathematical Modeling of Flow around Ship Hull

Computational Fluid Dynamics (CFD) is the branch of fluid dynamics providing a cost-effective means of simulating real flows by the numerical solution of the governing equations. The governing equations [25] of 3-dimensional turbulent flows for an incompressible fluid around a ship can be represented by the continuity and momentum equations as follows:

$$\frac{\partial u}{\partial x} + \frac{\partial v}{\partial y} + \frac{\partial w}{\partial z} = 0 \quad (2.1)$$

$$\rho \left(\frac{\partial u}{\partial t} + u \frac{\partial u}{\partial x} + v \frac{\partial u}{\partial y} + w \frac{\partial u}{\partial z} \right) = -\frac{\partial p}{\partial x} + \mu \left(\frac{\partial^2 u}{\partial x^2} + \frac{\partial^2 u}{\partial y^2} + \frac{\partial^2 u}{\partial z^2} \right) \quad (2.2)$$

$$\rho \left(\frac{\partial v}{\partial t} + u \frac{\partial v}{\partial x} + v \frac{\partial v}{\partial y} + w \frac{\partial v}{\partial z} \right) = -\frac{\partial p}{\partial y} + \mu \left(\frac{\partial^2 v}{\partial x^2} + \frac{\partial^2 v}{\partial y^2} + \frac{\partial^2 v}{\partial z^2} \right) \quad (2.3)$$

$$\rho \left(\frac{\partial w}{\partial t} + u \frac{\partial w}{\partial x} + v \frac{\partial w}{\partial y} + w \frac{\partial w}{\partial z} \right) = -\frac{\partial p}{\partial z} + \mu \left(\frac{\partial^2 w}{\partial x^2} + \frac{\partial^2 w}{\partial y^2} + \frac{\partial^2 w}{\partial z^2} \right) \quad (2.4)$$

Equations (2.2) to (2.4) are called the Navier Stokes equations, where ρ and μ are the density and the kinematic viscosity of the fluid. p is the pressure exerted by the fluid and u, v, w are the instantaneous velocity components along the x, y and z directions respectively.

In the fluid motion, the inertia forces are sufficiently large to amplify the disturbance and a transition to turbulence occurs at the high Reynolds number. The velocity and all other flow properties are varying in a random and chaotic way. The random nature of flow and the inherent non-linearity in the Navier-Stokes (NS) equations precludes an analytical description of flow computation.

2.1 Reynolds Averaged Navier-Stokes Equations

Turbulence consists of random fluctuation of various flow properties and for best purposes, a procedure introduced by Reynolds [26] that all quantities are expressed as sum of mean fluctuating parts. This is called Reynolds decomposition.

$$\varphi = \bar{\varphi} + \varphi' \quad (2.5)$$

where $\bar{\varphi}$ and φ' are the mean and fluctuating terms respectively. The mean or time averaged $\bar{\varphi}$ is defined by,

$$\bar{\varphi} = \frac{1}{\Delta t} \int_0^{\Delta t} \varphi dt \quad (2.6)$$

The time average of the mean value

$$\overline{\bar{\varphi}} = \frac{1}{\Delta t} \int_0^{\Delta t} \bar{\varphi} dt = \bar{\varphi} \quad (2.7)$$

The time average of the fluctuating term

$$\overline{\varphi'} = \frac{1}{\Delta t} \int_0^{\Delta t} \varphi' dt = \frac{1}{\Delta t} \int_0^{\Delta t} (\varphi - \bar{\varphi}) dt = 0 \quad (2.8)$$

Other time averaging term for variable φ and ψ can be written as follows:

$$\overline{\overline{\varphi\varphi'}} = \frac{1}{\Delta t} \int_0^{\Delta t} \overline{\varphi\varphi'} dt = \frac{1}{\Delta t} \overline{\varphi} \int_0^{\Delta t} \varphi' dt = \overline{\varphi\varphi'} = 0 \quad (2.9)$$

$$\overline{\varphi + \psi} = \frac{1}{\Delta t} \int_0^{\Delta t} (\varphi + \psi) dt = \bar{\varphi} + \bar{\psi} \quad (2.10)$$

$$\overline{\varphi\psi} = \overline{(\bar{\varphi} + \varphi')(\bar{\psi} + \psi')} = \overline{\bar{\varphi}\bar{\psi} + \bar{\varphi}\psi' + \varphi'\bar{\psi} + \varphi'\psi'} = \bar{\varphi}\bar{\psi} + \overline{\varphi'\psi'} \quad (2.11)$$

$$\overline{\overline{\varphi\psi}} = \overline{\bar{\varphi}\bar{\psi} + \varphi'\bar{\psi}'} = \overline{\bar{\varphi}\bar{\psi}} \quad (2.12)$$

$$\frac{\partial \overline{\varphi}}{\partial t} = \frac{\partial \bar{\varphi}}{\partial t} \overline{\overline{\varphi'\psi'}} = \frac{1}{\Delta t} \int_0^{\Delta t} \varphi'\psi' dt \quad (2.13)$$

Decomposition the flow properties in mean and fluctuating terms give:

$$\begin{aligned} u &= \bar{u} + u' \\ v &= \bar{v} + v' \\ w &= \bar{w} + w' \\ p &= \bar{p} + p' \end{aligned} \quad (2.14)$$

Substituting these decomposition terms into the continuity and momentum equations and following the time averaging properties, the Reynolds form of continuity equation becomes

$$\frac{\partial}{\partial t}(\bar{\rho} + \rho') + \frac{\partial}{\partial x}(\bar{u} + u')(\bar{\rho} + \rho') + \frac{\partial}{\partial y}(\bar{v} + v')(\bar{\rho} + \rho') + \frac{\partial}{\partial z}(\bar{w} + w')(\bar{\rho} + \rho') = 0 \quad (2.15)$$

$$\frac{\partial}{\partial t}(\bar{\rho} + \rho') = \frac{\partial \bar{\rho}}{\partial t} \quad (2.16)$$

$$\frac{\partial}{\partial x}(\bar{u} + u')(\bar{\rho} + \rho') = \frac{\partial}{\partial x}(\bar{u}\bar{\rho} + \bar{u}\rho' + u'\bar{\rho} + u'\rho') = \frac{\partial}{\partial x}(\bar{u}\bar{\rho} + \overline{u'\rho'}) \quad (2.17)$$

$$\frac{\partial}{\partial y}(\bar{v} + v')(\bar{\rho} + \rho') = \frac{\partial}{\partial y}(\bar{v}\bar{\rho} + \overline{v'\rho'}) \quad (2.18)$$

$$\frac{\partial}{\partial z}(\bar{w} + w')(\bar{\rho} + \rho') = \frac{\partial}{\partial z}(\bar{w}\bar{\rho} + \overline{w'\rho'}) \quad (2.19)$$

$$\frac{\partial \bar{\rho}}{\partial t} + \frac{\partial}{\partial x}(\bar{u}\bar{\rho} + \overline{u'\rho'}) + \frac{\partial}{\partial y}(\bar{v}\bar{\rho} + \overline{v'\rho'}) + \frac{\partial}{\partial z}(\bar{w}\bar{\rho} + \overline{w'\rho'}) = 0 \quad (2.20)$$

Reynolds form of momentum equation for x -component,

$$\begin{aligned} & \frac{\partial}{\partial t}[(\bar{\rho} + \rho')(\bar{u} + u')] + \frac{\partial}{\partial x}[(\bar{\rho} + \rho')(\bar{u} + u')(\bar{u} + u')] \\ & + \frac{\partial}{\partial y}[(\bar{\rho} + \rho')(\bar{u} + u')(\bar{v} + v')] + \frac{\partial}{\partial z}[(\bar{\rho} + \rho')(\bar{u} + u')(\bar{w} + w')] \\ & = -\frac{\partial}{\partial x}(\bar{p} + p') + \frac{\partial}{\partial x} \left[2\mu \frac{\partial}{\partial x}(\bar{u} + u') + \frac{2}{3}\mu \left\{ \frac{\partial}{\partial x}(\bar{u} + u') + \frac{\partial}{\partial y}(\bar{v} + v') + \frac{\partial}{\partial z}(\bar{w} + w') \right\} \right] \\ & + \frac{\partial}{\partial y} \left[\mu \left\{ \frac{\partial}{\partial y}(\bar{u} + u') + \frac{\partial}{\partial x}(\bar{v} + v') \right\} \right] + \frac{\partial}{\partial z} \left[\mu \left\{ \frac{\partial}{\partial z}(\bar{u} + u') + \frac{\partial}{\partial x}(\bar{w} + w') \right\} \right] \end{aligned} \quad (2.21)$$

$$\begin{aligned} & \frac{\partial}{\partial t}(\bar{\rho}u + \rho'u') + \frac{\partial}{\partial x}(\bar{\rho}u\bar{u} + 2\bar{u}\rho'u' + \bar{\rho}u'u' + \rho'u'u') \\ & + \frac{\partial}{\partial y}(\bar{\rho}u\bar{v} + \bar{\rho}u'v' + \bar{v}\rho'u' + \bar{u}\rho'v' + \rho'u'v') + \frac{\partial}{\partial z}(\bar{\rho}u\bar{w} + \bar{\rho}u'w' + \bar{w}\rho'u' + \bar{u}\rho'w' + \rho'u'w') \\ & = -\frac{\partial \bar{p}}{\partial x} + \frac{\partial}{\partial x} \left[2\mu \frac{\partial \bar{u}}{\partial x} + \frac{2}{3}\mu \left(\frac{\partial \bar{u}}{\partial x} + \frac{\partial \bar{v}}{\partial y} + \frac{\partial \bar{w}}{\partial z} \right) \right] + \frac{\partial}{\partial y} \left[\mu \left\{ \frac{\partial \bar{u}}{\partial y} + \frac{\partial \bar{v}}{\partial x} \right\} \right] + \frac{\partial}{\partial z} \left[\mu \left\{ \frac{\partial \bar{u}}{\partial z} + \frac{\partial \bar{w}}{\partial x} \right\} \right] \\ & = -\frac{\partial \bar{p}}{\partial x} + \frac{\partial \bar{\tau}_{xx}}{\partial x} + \frac{\partial \bar{\tau}_{yx}}{\partial y} + \frac{\partial \bar{\tau}_{zx}}{\partial z} \end{aligned} \quad (2.22)$$

$$\frac{\partial}{\partial t}(\bar{\rho}u + \rho'u') + \frac{\partial}{\partial x}(\bar{\rho}u\bar{u} + \overline{u'\rho'u'}) + \frac{\partial}{\partial y}(\bar{\rho}u\bar{v} + \overline{u'\rho'v'}) + \frac{\partial}{\partial z}(\bar{\rho}u\bar{w} + \overline{u'\rho'w'})$$

$$\begin{aligned}
 &= -\frac{\partial \bar{p}}{\partial x} + \frac{\partial}{\partial x} \left(\bar{\tau}_{xx} - \overline{u\rho'u'} - \overline{\rho'u'u'} - \overline{\rho'u'u'} \right) + \frac{\partial}{\partial y} \left(\bar{\tau}_{yx} - \overline{\rho'u'v'} - \overline{v\rho'u'} - \overline{\rho'u'v'} \right) \\
 &+ \frac{\partial}{\partial z} \left(\bar{\tau}_{zx} - \overline{\rho'u'w'} - \overline{w\rho'u'} - \overline{\rho'u'w'} \right)
 \end{aligned} \tag{2.23}$$

Similarly the y and z components

$$\begin{aligned}
 &\frac{\partial}{\partial t} (\overline{\rho v} + \overline{\rho'v'}) + \frac{\partial}{\partial x} (\overline{\rho v u} + \overline{v\rho'u'}) + \frac{\partial}{\partial y} (\overline{\rho v v} + \overline{v\rho'v'}) + \frac{\partial}{\partial z} (\overline{\rho v w} + \overline{v\rho'w'}) \\
 &= -\frac{\partial \bar{p}}{\partial y} + \frac{\partial}{\partial x} \left(\bar{\tau}_{yx} - \overline{u\rho'v'} - \overline{\rho'v'u'} - \overline{\rho'v'u'} \right) + \frac{\partial}{\partial y} \left(\bar{\tau}_{yy} - \overline{\rho'u'v'} - \overline{v\rho'v'} - \overline{\rho'v'v'} \right) \\
 &+ \frac{\partial}{\partial z} \left(\bar{\tau}_{zy} - \overline{\rho'v'w'} - \overline{w\rho'v'} - \overline{\rho'v'w'} \right)
 \end{aligned} \tag{2.24}$$

$$\begin{aligned}
 &\frac{\partial}{\partial t} (\overline{\rho w} + \overline{\rho'w'}) + \frac{\partial}{\partial x} (\overline{\rho w u} + \overline{w\rho'u'}) + \frac{\partial}{\partial y} (\overline{\rho w v} + \overline{w\rho'v'}) + \frac{\partial}{\partial z} (\overline{\rho w w} + \overline{w\rho'w'}) \\
 &= -\frac{\partial \bar{p}}{\partial w} + \frac{\partial}{\partial x} \left(\bar{\tau}_{zx} - \overline{w\rho'w'} - \overline{\rho'w'u'} - \overline{\rho'w'u'} \right) + \frac{\partial}{\partial y} \left(\bar{\tau}_{zy} - \overline{\rho'w'v'} - \overline{v\rho'w'} - \overline{\rho'w'v'} \right) \\
 &+ \frac{\partial}{\partial z} \left(\bar{\tau}_{zz} - \overline{\rho'w'w'} - \overline{w\rho'w'} - \overline{\rho'w'w'} \right)
 \end{aligned} \tag{2.25}$$

These Equations (2.23), (2.24), and (2.25) are called Reynolds Averaged Navier-Stokes equation for unsteady, compressible flows

Where,

$$\bar{\tau}_{xx} = 2\mu \frac{\partial \bar{u}}{\partial x} + \frac{2}{3}\mu \left(\frac{\partial \bar{u}}{\partial x} + \frac{\partial \bar{v}}{\partial y} + \frac{\partial \bar{w}}{\partial z} \right) \tag{2.26}$$

$$\bar{\tau}_{yy} = 2\mu \frac{\partial \bar{v}}{\partial y} + \frac{2}{3}\mu \left(\frac{\partial \bar{u}}{\partial x} + \frac{\partial \bar{v}}{\partial y} + \frac{\partial \bar{w}}{\partial z} \right) \tag{2.27}$$

$$\bar{\tau}_{zz} = 2\mu \frac{\partial \bar{w}}{\partial z} + \frac{2}{3}\mu \left(\frac{\partial \bar{u}}{\partial x} + \frac{\partial \bar{v}}{\partial y} + \frac{\partial \bar{w}}{\partial z} \right) \tag{2.28}$$

$$\bar{\tau}_{xy} = \bar{\tau}_{yx} = \mu \left(\frac{\partial \bar{u}}{\partial y} + \frac{\partial \bar{v}}{\partial x} \right) \tag{2.29}$$

$$\bar{\tau}_{xz} = \bar{\tau}_{zx} = \mu \left(\frac{\partial \bar{u}}{\partial z} + \frac{\partial \bar{w}}{\partial x} \right) \tag{2.30}$$

$$\bar{\tau}_{yz} = \bar{\tau}_{zy} = \mu \left(\frac{\partial \bar{v}}{\partial z} + \frac{\partial \bar{w}}{\partial y} \right) \tag{2.31}$$

For **unsteady and incompressible flow** the continuity and momentum equation becomes,

$$\frac{\partial \bar{u}}{\partial x} + \frac{\partial \bar{v}}{\partial y} + \frac{\partial \bar{w}}{\partial z} = 0 \quad (2.32)$$

x- Component of momentum equation

$$\begin{aligned} & \rho \left[\frac{\partial}{\partial t} (\bar{u} + u') + \frac{\partial}{\partial x} (\bar{u} + u') (\bar{u} + u') + \frac{\partial}{\partial y} (\bar{u} + u') (\bar{v} + v') + \frac{\partial}{\partial z} (\bar{u} + u') (\bar{w} + w') \right] \\ &= -\frac{\partial}{\partial x} (\bar{p} + p') + \frac{\partial}{\partial x} \left[2\mu \frac{\partial}{\partial x} (\bar{u} + u') \right] + \frac{\partial}{\partial y} \left[\mu \left\{ \frac{\partial}{\partial y} (\bar{u} + u') + \frac{\partial}{\partial x} (\bar{v} + v') \right\} \right] \\ &+ \frac{\partial}{\partial z} \left[\mu \left\{ \frac{\partial}{\partial z} (\bar{u} + u') + \frac{\partial}{\partial x} (\bar{w} + w') \right\} \right] \end{aligned} \quad (2.33)$$

$$\begin{aligned} & \rho \left[\frac{\partial \bar{u}}{\partial t} + \frac{\partial}{\partial x} (\bar{u}\bar{u} + \overline{u'u'}) + \frac{\partial}{\partial y} (\bar{u}\bar{v} + \overline{u'v'}) + \frac{\partial}{\partial z} (\bar{u}\bar{w} + \overline{u'w'}) \right] \\ &= -\frac{\partial \bar{p}}{\partial x} + \frac{\partial}{\partial x} \left[2\mu \frac{\partial \bar{u}}{\partial x} \right] + \frac{\partial}{\partial y} \left[\mu \left(\frac{\partial \bar{u}}{\partial y} + \frac{\partial \bar{v}}{\partial x} \right) \right] + \frac{\partial}{\partial z} \left[\mu \left(\frac{\partial \bar{u}}{\partial z} + \frac{\partial \bar{w}}{\partial x} \right) \right] \\ &= -\frac{\partial \bar{p}}{\partial x} + \frac{\partial \bar{\tau}_{xx}}{\partial x} + \frac{\partial \bar{\tau}_{yx}}{\partial y} + \frac{\partial \bar{\tau}_{zx}}{\partial z} \end{aligned} \quad (2.34)$$

$$\rho \left[\frac{\partial \bar{u}}{\partial t} + \frac{\partial \bar{u}\bar{u}}{\partial x} + \frac{\partial \bar{u}\bar{v}}{\partial y} + \frac{\partial \bar{u}\bar{w}}{\partial z} \right] = -\frac{\partial \bar{p}}{\partial x} + \frac{\partial}{\partial x} (\bar{\tau}_{xx} - \rho \overline{u'u'}) + \frac{\partial}{\partial y} (\bar{\tau}_{yx} - \rho \overline{u'v'}) + \frac{\partial}{\partial z} (\bar{\tau}_{zx} - \rho \overline{u'w'}) \quad (2.35)$$

y- Component of momentum equation

$$\rho \left[\frac{\partial \bar{v}}{\partial t} + \frac{\partial \bar{v}\bar{u}}{\partial x} + \frac{\partial \bar{v}\bar{v}}{\partial y} + \frac{\partial \bar{v}\bar{w}}{\partial z} \right] = -\frac{\partial \bar{p}}{\partial y} + \frac{\partial}{\partial x} (\bar{\tau}_{xy} - \rho \overline{u'v'}) + \frac{\partial}{\partial y} (\bar{\tau}_{yy} - \rho \overline{v'v'}) + \frac{\partial}{\partial z} (\bar{\tau}_{zy} - \rho \overline{v'w'}) \quad (2.36)$$

z- Component of momentum equation

$$\rho \left[\frac{\partial \bar{w}}{\partial t} + \frac{\partial \bar{w}\bar{u}}{\partial x} + \frac{\partial \bar{w}\bar{v}}{\partial y} + \frac{\partial \bar{w}\bar{w}}{\partial z} \right] = -\frac{\partial \bar{p}}{\partial z} + \frac{\partial}{\partial x} (\bar{\tau}_{xz} - \rho \overline{u'w'}) + \frac{\partial}{\partial y} (\bar{\tau}_{yz} - \rho \overline{v'w'}) + \frac{\partial}{\partial z} (\bar{\tau}_{zz} - \rho \overline{w'w'}) \quad (2.37)$$

These equations (2.35), (2.36), and (2.37) are called Reynolds Averaged Navier-Stokes equation for unsteady incompressible flow.

Where,

$$\bar{\tau}_{xx} = 2\mu \frac{\partial \bar{u}}{\partial x} \quad (2.38)$$

$$\bar{\tau}_{yy} = 2\mu \frac{\partial \bar{u}}{\partial y} \quad (2.39)$$

$$\bar{\tau}_{zz} = 2\mu \frac{\partial \bar{u}}{\partial z} \quad (2.40)$$

$$\bar{\tau}_{xy} = \bar{\tau}_{yx} = \mu \left(\frac{\partial \bar{u}}{\partial y} + \frac{\partial \bar{v}}{\partial x} \right) \quad (2.41)$$

$$\bar{\tau}_{xz} = \bar{\tau}_{zx} = \mu \left(\frac{\partial \bar{u}}{\partial z} + \frac{\partial \bar{w}}{\partial x} \right) \quad (2.42)$$

$$\bar{\tau}_{yz} = \bar{\tau}_{zy} = \mu \left(\frac{\partial \bar{v}}{\partial z} + \frac{\partial \bar{w}}{\partial y} \right) \quad (2.43)$$

Here all the instantaneous quantities are replaced by their corresponding time-averaged quantities. But there are appearances of new additional six quantities (**Reynolds stress tensor**) in the equation and also there are no new equations. In general, there are already four unknown mean-flow properties i.e. pressure and three velocity components and now along with six new unknowns, hence in total there are ten unknowns. And, unfortunately the system has only four equations (Continuity and three momentum equations). So, it is needed to find enough equations to close the system.

2.2 Turbulence Modeling

Modeling the turbulence is referred as the process of finding a closure to the Reynolds Averaged Navier-Stokes equations. The additional Reynolds stress terms represent the effect of the fluctuating velocity components of the mean velocity field. To modeling the turbulence, a more popular approach called eddy-viscosity or turbulent viscosity will be presented here. In this closure approach, differential equations or transport equations are derived for each of the Reynolds stresses.

Boussinesq [27] suggested that the apparent turbulent shearing stress might be related to the rate of mean strain through an apparent scalar turbulent or eddy viscosity. For Reynolds stress tensor, the Boussinesq hypotheses,

$$-\overline{\rho u' u'} = 2\mu_t \frac{\partial \bar{u}}{\partial x} - \frac{2}{3} \rho k \quad (2.44)$$

$$-\overline{\rho v' v'} = 2\mu_t \frac{\partial \bar{u}}{\partial y} - \frac{2}{3} \rho k \quad (2.45)$$

$$-\overline{\rho w' w'} = 2\mu_t \frac{\partial \bar{u}}{\partial z} - \frac{2}{3} \rho k \quad (2.46)$$

$$-\rho\overline{u'v'} = -\rho\overline{v'u'} = \mu_t \left(\frac{\partial\bar{u}}{\partial y} + \frac{\partial\bar{v}}{\partial x} \right) \quad (2.47)$$

$$-\rho\overline{u'w'} = -\rho\overline{w'u'} = \mu_t \left(\frac{\partial\bar{u}}{\partial z} + \frac{\partial\bar{w}}{\partial x} \right) \quad (2.48)$$

$$-\rho\overline{v'w'} = -\rho\overline{w'v'} = \mu_t \left(\frac{\partial\bar{v}}{\partial z} + \frac{\partial\bar{w}}{\partial y} \right) \quad (2.49)$$

Where μ_t is turbulent viscosity and k is called the *turbulent kinetic energy* and expressed as

$$k = \frac{1}{2}(\overline{u'u'} + \overline{v'v'} + \overline{w'w'}) = \frac{1}{2}(\overline{u'^2} + \overline{v'^2} + \overline{w'^2}) \quad (2.50)$$

The hypothesis provided by Boussinesq, replaces the Reynolds stress when put into the momentum equations but it generates two new unknowns k and μ_t . Both k and μ_t vary point to point in the flow.

Substituting Equations (2.44), (2.45), (2.46), (2.47), (2.48), and (2.49) into the Equations (2.35), (2.36), and (2.37) the Reynolds Averaged momentum equation of x -component becomes,

$$\begin{aligned} \frac{\partial\bar{u}}{\partial t} + \frac{\partial\bar{u}\bar{u}}{\partial x} + \frac{\partial\bar{u}\bar{v}}{\partial y} + \frac{\partial\bar{u}\bar{w}}{\partial z} &= -\frac{1}{\rho} \frac{\partial\bar{p}}{\partial x} + \frac{1}{\rho} \frac{\partial}{\partial x} (\bar{\tau}_{xx} - \rho\overline{u'u'}) + \frac{1}{\rho} \frac{\partial}{\partial y} (\bar{\tau}_{yx} - \rho\overline{u'v'}) + \frac{1}{\rho} \frac{\partial}{\partial z} (\bar{\tau}_{zx} - \rho\overline{u'w'}) \\ &= -\frac{1}{\rho} \frac{\partial\bar{p}}{\partial x} + \frac{1}{\rho} \frac{\partial}{\partial x} \left(2\mu \frac{\partial\bar{u}}{\partial x} - \rho\overline{u'u'} \right) + \frac{1}{\rho} \frac{\partial}{\partial y} \left[\mu \left(\frac{\partial\bar{u}}{\partial y} + \frac{\partial\bar{v}}{\partial x} \right) - \rho\overline{u'v'} \right] + \frac{1}{\rho} \frac{\partial}{\partial z} \left[\mu \left(\frac{\partial\bar{u}}{\partial z} + \frac{\partial\bar{w}}{\partial x} \right) - \rho\overline{u'w'} \right] \end{aligned} \quad (2.51)$$

Simplifying the right hand side of the above equation:

$$\begin{aligned} \frac{1}{\rho} \frac{\partial}{\partial x} \left(2\mu \frac{\partial\bar{u}}{\partial x} - \rho\overline{u'u'} \right) &= \frac{1}{\rho} \frac{\partial}{\partial x} \left(2\mu \frac{\partial\bar{u}}{\partial x} + 2\mu_t \frac{\partial\bar{u}}{\partial x} - \frac{2}{3} \rho k \right) \\ &= \frac{\partial}{\partial x} \left[2(\nu + \nu_t) \frac{\partial\bar{u}}{\partial x} \right] - \frac{1}{\rho} \frac{\partial}{\partial x} \left(\frac{2}{3} \rho k \right) \end{aligned} \quad (2.52)$$

$$\begin{aligned} \frac{1}{\rho} \frac{\partial}{\partial y} \left[\mu \left(\frac{\partial\bar{u}}{\partial y} + \frac{\partial\bar{v}}{\partial x} \right) - \rho\overline{u'v'} \right] + \frac{1}{\rho} \frac{\partial}{\partial z} \left[\mu \left(\frac{\partial\bar{u}}{\partial z} + \frac{\partial\bar{w}}{\partial x} \right) - \rho\overline{u'w'} \right] \\ = \frac{1}{\rho} \frac{\partial}{\partial y} \left[\mu \left(\frac{\partial\bar{u}}{\partial y} + \frac{\partial\bar{v}}{\partial x} \right) + \mu_t \left(\frac{\partial\bar{u}}{\partial y} + \frac{\partial\bar{v}}{\partial x} \right) \right] + \frac{1}{\rho} \frac{\partial}{\partial z} \left[\mu \left(\frac{\partial\bar{u}}{\partial z} + \frac{\partial\bar{w}}{\partial x} \right) + \mu_t \left(\frac{\partial\bar{u}}{\partial z} + \frac{\partial\bar{w}}{\partial x} \right) \right] \end{aligned}$$

$$\begin{aligned}
 &= \frac{1}{\rho} \frac{\partial}{\partial y} \left[(\mu + \mu_t) \frac{\partial \bar{u}}{\partial y} \right] + \frac{1}{\rho} \frac{\partial}{\partial z} \left[(\mu + \mu_t) \frac{\partial \bar{u}}{\partial z} \right] + \frac{1}{\rho} \frac{\partial}{\partial x} \left[(\mu + \mu_t) \frac{\partial \bar{v}}{\partial y} \right] + \frac{1}{\rho} \frac{\partial}{\partial x} \left[(\mu + \mu_t) \frac{\partial \bar{w}}{\partial z} \right] \\
 &= \frac{\partial}{\partial y} \left[(\nu + \nu_t) \frac{\partial \bar{u}}{\partial y} \right] + \frac{\partial}{\partial z} \left[(\nu + \nu_t) \frac{\partial \bar{u}}{\partial z} \right] + \frac{\partial}{\partial x} \left[(\nu + \nu_t) \frac{\partial \bar{v}}{\partial y} \right] + \frac{\partial}{\partial x} \left[(\nu + \nu_t) \frac{\partial \bar{w}}{\partial z} \right] \quad (2.53)
 \end{aligned}$$

After rearranging the momentum equation of x -component becomes

$$\begin{aligned}
 \frac{\partial \bar{u}}{\partial t} + \frac{\partial \bar{u}\bar{u}}{\partial x} + \frac{\partial \bar{u}\bar{v}}{\partial y} + \frac{\partial \bar{u}\bar{w}}{\partial z} &= -\frac{1}{\rho} \frac{\partial \bar{p}}{\partial x} + \frac{\partial}{\partial x} \left[(\nu + \nu_t) \frac{\partial \bar{u}}{\partial x} \right] + \frac{\partial}{\partial y} \left[(\nu + \nu_t) \frac{\partial \bar{u}}{\partial y} \right] + \frac{\partial}{\partial z} \left[(\nu + \nu_t) \frac{\partial \bar{u}}{\partial z} \right] \\
 &\quad - \frac{1}{\rho} \frac{\partial}{\partial x} \left(\frac{2}{3} \rho k \right) + \frac{\partial}{\partial x} \left[(\nu + \nu_t) \left(\frac{\partial \bar{u}}{\partial x} + \frac{\partial \bar{v}}{\partial y} + \frac{\partial \bar{w}}{\partial z} \right) \right] \\
 &= -\frac{1}{\rho} \frac{\partial \bar{p}}{\partial x} + \frac{\partial}{\partial x} \left[(\nu + \nu_t) \frac{\partial \bar{u}}{\partial x} \right] + \frac{\partial}{\partial y} \left[(\nu + \nu_t) \frac{\partial \bar{u}}{\partial y} \right] + \frac{\partial}{\partial z} \left[(\nu + \nu_t) \frac{\partial \bar{u}}{\partial z} \right] - \frac{1}{\rho} \frac{\partial}{\partial x} \left(\frac{2}{3} \rho k \right) \\
 &= -\frac{1}{\rho} \frac{\partial}{\partial x} \left(\bar{p} + \frac{2}{3} \rho k \right) + \frac{\partial}{\partial x} \left[(\nu + \nu_t) \frac{\partial \bar{u}}{\partial x} \right] + \frac{\partial}{\partial y} \left[(\nu + \nu_t) \frac{\partial \bar{u}}{\partial y} \right] + \frac{\partial}{\partial z} \left[(\nu + \nu_t) \frac{\partial \bar{u}}{\partial z} \right] \quad (2.54)
 \end{aligned}$$

$$\frac{\partial \bar{u}}{\partial t} + \frac{\partial \bar{u}\bar{u}}{\partial x} + \frac{\partial \bar{u}\bar{v}}{\partial y} + \frac{\partial \bar{u}\bar{w}}{\partial z} = -\frac{1}{\rho} \frac{\partial \bar{P}}{\partial x} + \frac{\partial}{\partial x} \left[(\nu + \nu_t) \frac{\partial \bar{u}}{\partial x} \right] + \frac{\partial}{\partial y} \left[(\nu + \nu_t) \frac{\partial \bar{u}}{\partial y} \right] + \frac{\partial}{\partial z} \left[(\nu + \nu_t) \frac{\partial \bar{u}}{\partial z} \right] \quad (2.55)$$

y-component

$$\frac{\partial \bar{v}}{\partial t} + \frac{\partial \bar{v}\bar{u}}{\partial x} + \frac{\partial \bar{v}\bar{v}}{\partial y} + \frac{\partial \bar{v}\bar{w}}{\partial z} = -\frac{1}{\rho} \frac{\partial \bar{P}}{\partial y} + \frac{\partial}{\partial x} \left[(\nu + \nu_t) \frac{\partial \bar{v}}{\partial x} \right] + \frac{\partial}{\partial y} \left[(\nu + \nu_t) \frac{\partial \bar{v}}{\partial y} \right] + \frac{\partial}{\partial z} \left[(\nu + \nu_t) \frac{\partial \bar{v}}{\partial z} \right] \quad (2.56)$$

z-component

$$\frac{\partial \bar{w}}{\partial t} + \frac{\partial \bar{w}\bar{u}}{\partial x} + \frac{\partial \bar{w}\bar{v}}{\partial y} + \frac{\partial \bar{w}\bar{w}}{\partial z} = -\frac{1}{\rho} \frac{\partial \bar{P}}{\partial z} + \frac{\partial}{\partial x} \left[(\nu + \nu_t) \frac{\partial \bar{w}}{\partial x} \right] + \frac{\partial}{\partial y} \left[(\nu + \nu_t) \frac{\partial \bar{w}}{\partial y} \right] + \frac{\partial}{\partial z} \left[(\nu + \nu_t) \frac{\partial \bar{w}}{\partial z} \right] \quad (2.57)$$

Where,

$$\bar{P} = \text{Modified pressure} = \bar{p} + \frac{2}{3} \rho k$$

$$\nu = \text{Molecular kinematic viscosity} = \frac{\mu}{\rho}$$

$$\nu_t = \text{Turbulent kinematic viscosity} = \frac{\mu_t}{\rho}$$

In these equations, the viscosity is replaced by the sum of molecular viscosity and turbulent viscosity. Now the main task of the closure form is to find the distribution of turbulent viscosity or turbulent kinematic viscosity in the solution domain. And this can be done by solving two differential or transport equation referred as two-equation models. One represent the generation and transport of turbulence and other represent the transport of dissipation of turbulence [26].

2.2.1 $k-\varepsilon$ Turbulence Model

$k-\varepsilon$ Turbulence model is widely used for turbulent flow condition to simulate the mean flow characteristics. Jones and Launder [3] were the first to derive the equations that constitute the model. Further analyses leading to modifications of the constants were carried out by Launder and Sharma [4]. The $k-\varepsilon$ model focuses on the mechanisms that affect the turbulent kinetic energy (per unit mass) k . The complete derivation for turbulent kinetic energy is given in **Appendix A**. The other parameter ε is the dissipation rate of k . If k and ε are known we can model the turbulent viscosity as:

$$\mu_t = \rho C_\mu \frac{k^2}{\varepsilon} \quad \text{or} \quad \nu_t = C_\mu \frac{k^2}{\varepsilon} \quad (2.58)$$

The differential transport equations required for the standard $k-\varepsilon$ model, for the case of constant fluid property can be are

$$\frac{\partial k}{\partial t} + \bar{u} \frac{\partial k}{\partial x} + \bar{v} \frac{\partial k}{\partial y} + \bar{w} \frac{\partial k}{\partial z} = \frac{\partial}{\partial x} \left[\left(\nu + \frac{\nu_t}{\sigma_k} \right) \frac{\partial k}{\partial x} \right] + \frac{\partial}{\partial y} \left[\left(\nu + \frac{\nu_t}{\sigma_k} \right) \frac{\partial k}{\partial y} \right] + \frac{\partial}{\partial z} \left[\left(\nu + \frac{\nu_t}{\sigma_k} \right) \frac{\partial k}{\partial z} \right] + Q - \varepsilon \quad (2.59)$$

$$\frac{\partial \varepsilon}{\partial t} + \bar{u} \frac{\partial \varepsilon}{\partial x} + \bar{v} \frac{\partial \varepsilon}{\partial y} + \bar{w} \frac{\partial \varepsilon}{\partial z} = \frac{\partial}{\partial x} \left[\left(\nu + \frac{\nu_t}{\sigma_\varepsilon} \right) \frac{\partial \varepsilon}{\partial x} \right] + \frac{\partial}{\partial y} \left[\left(\nu + \frac{\nu_t}{\sigma_\varepsilon} \right) \frac{\partial \varepsilon}{\partial y} \right] + \frac{\partial}{\partial z} \left[\left(\nu + \frac{\nu_t}{\sigma_\varepsilon} \right) \frac{\partial \varepsilon}{\partial z} \right] + C_{\varepsilon 1} \frac{\varepsilon}{k} Q - C_{\varepsilon 2} \frac{\varepsilon^2}{k} \quad (2.60)$$

Where, σ_k (**turbulent Prandtl number**) is a closure coefficient and Q is the rate of production of k due to Reynolds stress and mean flow,

$$Q = 2\nu_t \left[\left(\frac{\partial \bar{u}}{\partial x} \right)^2 + \left(\frac{\partial \bar{v}}{\partial y} \right)^2 + \left(\frac{\partial \bar{w}}{\partial z} \right)^2 \right] + \nu_t \left[\left(\frac{\partial \bar{u}}{\partial y} + \frac{\partial \bar{v}}{\partial x} \right)^2 + \left(\frac{\partial \bar{v}}{\partial z} + \frac{\partial \bar{w}}{\partial y} \right)^2 + \left(\frac{\partial \bar{w}}{\partial x} + \frac{\partial \bar{u}}{\partial z} \right)^2 \right] \quad (2.61)$$

Standard value of model constants of the $k-\varepsilon$ turbulence model used in the model equations are:

$$C_{\mu}=0.09 \quad C_{\varepsilon 1}=1.44 \quad C_{\varepsilon 2}=1.92 \quad \sigma_k=1.0 \quad \sigma_{\varepsilon}=1.3 \quad (2.62)$$

2.3 Near Wall modeling and wall function

Due to the presence of solid boundary or walls, increasing importance of viscous effects are caused to change the structure of turbulent flow. Near wall region have larger gradients in the solution variables, and momentum and other scalar transports occur more vigorously, Salim [29]. Based on corresponding wall y^+ value, it can be seen that the viscosity affected region is constitute of three zones which is well explained from Fig. 2.1.

- Viscous sublayer
- Buffer layer or blending region
- Fully turbulent or log-law region

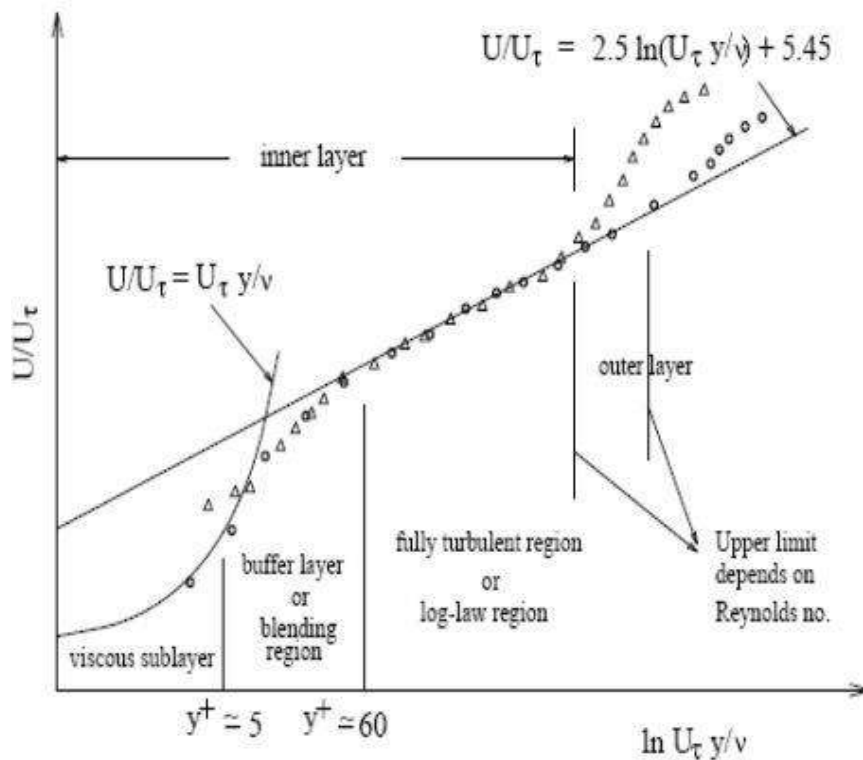


Fig. 2.1: Boundary layer velocity profile [29]

At the solid wall the fluid is stationary and the behavior of the fluid closest to the wall is dominated by the viscous effects. This viscous sub-layer is in practice extremely thin ($y^+ < 5$)

and we assume the shear stress is approximately constant and equal to the wall shear stress τ_w throughout the layer. So,

$$\mu \frac{\partial \bar{u}}{\partial y} \cong \tau_w \quad (2.63)$$

$$\int \mu \partial \bar{u} = \int \tau_w \partial y \text{ or } \mu \bar{u} = \tau_w y + C \quad (2.64)$$

If $y=0$ then $\bar{u}=0$ get $C=0$ it comes $\bar{u} = \frac{\tau_w y}{\mu}$

Introducing two important non dimensional parameters u^+ and y^+ defined by

$$u^+ = \frac{\bar{u}}{u_*} \text{ and } y^+ = \frac{u_* y}{\nu} \quad (2.65)$$

Where $u_* =$ Friction velocity in the near wall region $= u_* = \sqrt{\frac{\tau_w}{\rho}}$

After using this two non-dimensional parameter in the equation we get,

$$u^+ u_* = \frac{\tau_w \nu y^+}{\mu u_*} \Rightarrow u^+ \frac{\tau_w}{\rho} = \frac{\tau_w \nu y^+}{\mu} \Rightarrow u^+ = y^+ \quad (2.66)$$

Because of this linear relationship between velocity and wall distance of the fluid layer adjacent is also known as the **laminar sub-layer**.

Outside the viscous sub-layer ($30 < y^+ < 500$) a region exist where viscous and turbulent effects are both important. The shear stress vary slowly with distance from the wall, and within thus inner region it is assumed to be constant and equal to the wall shear stress.

Considering Prandtl's mixing length hypothesis

$$-\overline{u'v'} = \left[l_m \left(\frac{\partial \bar{u}}{\partial y} \right) \right]^2 \quad (2.67)$$

Where the mixing length is given by

$l_m = \kappa y$ where κ is called **Von-Karman constant**.

And $-\overline{u'v'} = u_*^2$

After putting this into Equation (2.67) get

$$\kappa^2 y^2 \left(\frac{\partial \bar{u}}{\partial y} \right)^2 = u_*^2 \quad (2.68)$$

$$\kappa y \left(\frac{\partial \bar{u}}{\partial y} \right) = u_* \quad (2.69)$$

$$\kappa \frac{\partial u^+}{\partial y^+} = \frac{1}{y^+} \quad (2.70)$$

Integrating this equation between 0 to y^+ get

$$u^+ = \frac{1}{\kappa} \ln y^+ + B \quad (2.71)$$

Numerical values for the constants are found from measurements: Von-Karman constant $\kappa \approx 0.4$ and the additive constant $B \approx 5.5$ for smooth wall, wall roughness causes a decrease in the value of B . The above Equation (2.71) is called the **log-law**.

2.4 Free-Surface Flows

A ship hull moving in the water must incorporate both water, air, and the boundary between them. The position of the boundary is known only at the initial time; its location at later times has to be determined as part of the solution. The most frequently used method to capture the free surface in ship hydrodynamics is the Volume of Fluid (VOF) technique.

The VOF model [30] description assumes that all immiscible fluid phases present in a control volume share velocity, pressure and temperature fields. Therefore, the same set of basic governing equations describing mass, momentum, and energy transport in a single-phase flow is solved. In this volume of fluid (VOF) method, in addition to the conservation equations for mass and momentum, it is required to solve an equation for the filled fraction of each control volume, α so that $\alpha=1$ in filled control volumes (CVs) and $\alpha=0$ in empty CVs. From the continuity equation, the evolution of α is governed by the transport equation:

$$\frac{\partial \alpha}{\partial t} + \text{div} (\alpha \mathbf{v}) = 0 \quad (2.72)$$

Both fluids act as a single fluid whose properties vary in space according to the volume fraction of each phase [31], i.e.:

$$\begin{aligned}\rho &= \rho_1\alpha + \rho_2(1-\alpha) \\ \mu &= \mu_1\alpha + \mu_2(1-\alpha)\end{aligned}\tag{2.73}$$

The interface is simply the location where the fluid properties change abruptly. Then, a modified set of the Navier-Stokes equations can be used for the averaged fluid properties,

$$\frac{\partial u_i}{\partial t} + u_j \frac{\partial u_i}{\partial x_j} = -\frac{1}{\rho} \frac{\partial p}{\partial x_i} + \nu \frac{\partial^2 u_i}{\partial x_j \partial x_j} + S_i\tag{2.74}$$

This formulation of the Navier-Stokes equations contains an additional source term, S_i , accounting for the momentum exchange across the interface due to surface tension forces. This surface tension force has to be modelled correctly which can be a problem and expressed by

$$F_{fs} = \int_{\Omega} \sigma \kappa \text{grad } c \, d\Omega\tag{2.75}$$

where, surface curvature, $\kappa = -\text{div} \left(\frac{\text{grad } c}{|\text{grad } c|} \right)$

2.5 Hull Resistance

The ship hull experience the force of combination of both air and water against its movement called the total hull resistance. The total resistance has its two major components. The frictional resistance comes from the frictional or shear forces generated by the water flow and acts on the hull surface. The pressure developed normal to the surface is responsible to push the water from the hull surface and this developed pressure is the source of other component: residuary resistance. The traditional RANSE solver software divides the total resistance into a Reynolds number (R_n) dependent component, Frictional coefficient (C_F) and Froude number (F_n) dependent component, residuary resistance coefficient (C_R)

$$C_T = C_F(R_n) + C_R(F_n)\tag{2.76}$$

where C_T denotes total resistance coefficient while C_R is the residual resistance coefficient and C_F is frictional resistance coefficient. And,

$$R_n = \frac{\rho UL}{\mu} \text{ and } F_n = \frac{U}{\sqrt{gL}}\tag{2.77}$$

The coefficients are non-dimensionalized by

$$C_x = \frac{P_x}{1/2 \rho V^2} \tag{2.78}$$

where x in the subscript of C_x may refer to any resistance component. Total Resistance coefficient C_T is defined by,

$$C_T = \frac{R_T}{\frac{1}{2} \rho S U^2} \tag{2.79}$$

The pressure/residuary resistance coefficient can be split into

$$C_R = C_W + C_{VP} \tag{2.80}$$

where C_W is the wave resistance coefficient and C_{VP} is the viscous pressure resistance coefficient. Note that a fully submerged body inside a fluid of infinite depth has zero wave resistance (no free-surface effect) and the pressure resistance coefficient in this case becomes equal to the viscous pressure resistance coefficient.

2.6 Hull Induced Waves

The ship hull moves on the undistributed water surface crates the varying pressure field is caused for the wave generation. The water creates both diverging waves spread outward from the hull and transverse wave following behind the stern of the ship hull known as the Kelvin wave pattern. The pattern of wave change as the speed changes and consequently the wave length, the relative location of crest and trough of bow and stern waves are also changed. The bow wave system starts with a crest aft of the bow and stern wave system starts with a trough forward of the stern as shown in Fig. 2.2.

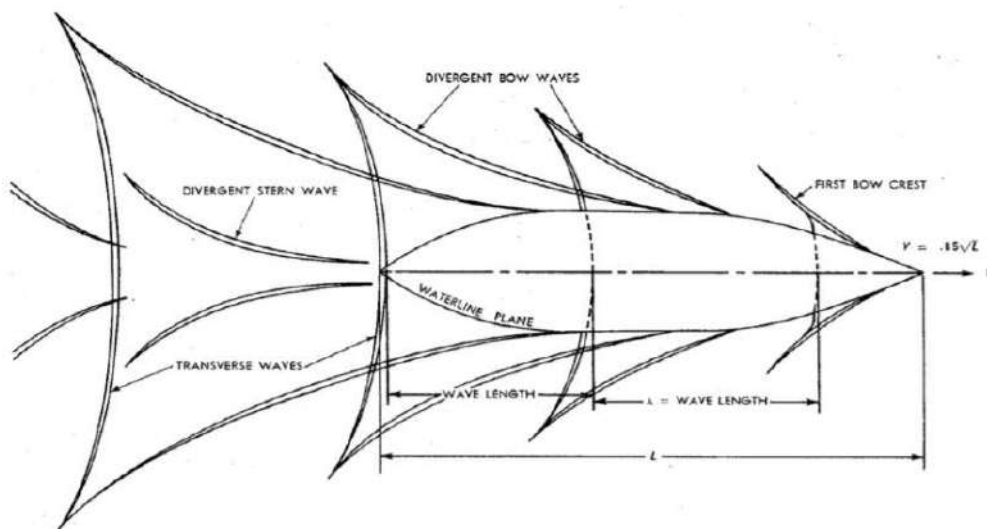


Fig. 2.2: The bow and stern wave systems [32]

A higher wave height generates when crest of the bow and stern wave coincide and therefore wave resistance will be higher. The opposite i.e. a lower wave height generates when crest of bow wave coincides with the trough of stern wave (vice versa) and wave resistance will be lower. These interference effect between the wave systems is reason for the hump and hollow condition in the resistance curve [33-34].

2.7 Rigid Body Dynamics

In modeling ship dynamics, the ship hull is assumed as rigid body with zero speed and has 6 degrees of freedoms (DOF) with three translational and three rotational motions as shown in Fig. 2.3.

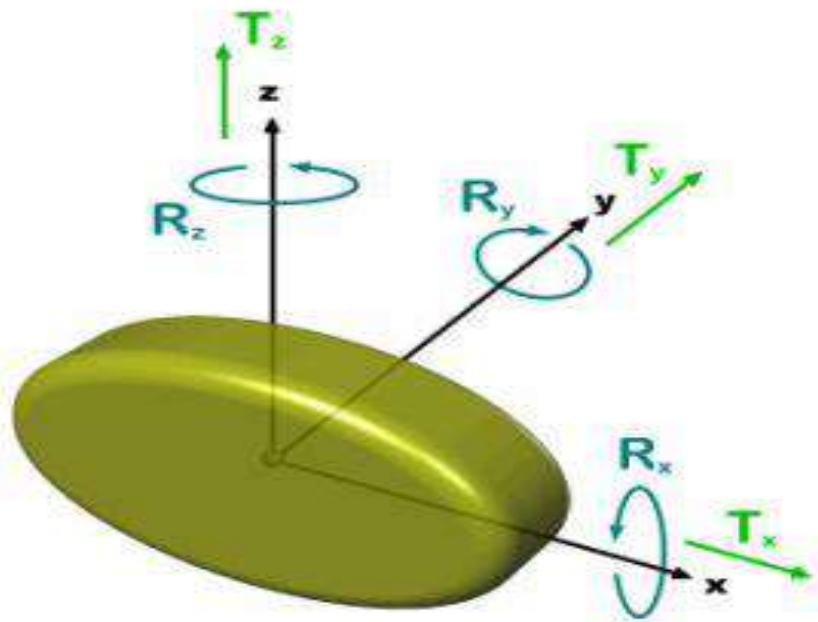


Fig. 2.3: Representation of Ship motion with 6 DOF [30]

Xing-Kaeding, Y. [35] described that the equations of the rigid body motion are coupled with the flow solver for computing the interaction between fluid flow and rigid body motion. The motion of the rigid body is strongly influenced by the forces acting on the body surface from the fluid flow around the body. The forces acting on the body consist of field forces and surface forces. The surface forces can be integrated from the pressure and shear forces acting on the body surface and the field forces are usually regarded as gravity force. The resultant force \mathbf{F} can be computed by the following expression:

$$\mathbf{F} = \int_s (\mathbf{T} - p\mathbf{l}) \cdot \mathbf{n} \, dS + mg \quad (2.81)$$

Here, \mathbf{F} is the total fluid force determined by integrating the pressure field and viscous stresses, obtained from the RANS equations. \mathbf{T} stands for the viscous stress tensor whose components are τ_{ij} (acts on each CV face) introduced in section 2.1, p is the pressure, \mathbf{n} the normal vector to each control volume (CV) face, and S the CV face area.

Field forces do not contribute to the moment around the center of mass, but the moments due to surface forces (pressure and shear forces) need to be integrated:

$$\mathbf{M} = \int_s (\mathbf{r} - \mathbf{r}_G) \times (\mathbf{T} - p\mathbf{l}) \cdot \mathbf{n} \, dS \quad (2.82)$$

Here the vector \mathbf{r} represents the position of a certain point on the body surface and \mathbf{r}_G the position of the mass center of the body.

2.7.1 Sinkage and Trim

In response to the resultant force and moment, STAR-CCM+ simulate the motion of the rigid body by solving the governing equation and also find the new position of the body. DFBI module allows to calculate the free motion in which selected motions are taken as active to be calculated and other motions are remain as frozen/constrained. The motion solver calculates the motion and the vertices of the grids are moved simultaneously (STAR-CCM+ user guide 2011 [30]).

The equation for the translation of the center of mass:

$$m \frac{d\mathbf{v}}{dt} = \mathbf{f} \quad (2.83)$$

Where m represents the mass of the body, \mathbf{f} is the resultant force acting on the body and \mathbf{v} is the velocity of the center of mass.

The equation of rotation of the body:

$$\mathbf{M} \frac{d\bar{\omega}}{dt} + \bar{\omega} \times \mathbf{M} \bar{\omega} = \mathbf{n} \quad (2.84)$$

where \mathbf{M} is the tensor of the moments of inertia, $\bar{\omega}$ is the angular velocity of the rigid body and \mathbf{n} is the resultant moment acting on the body. The tensor of the moments of inertia is expanded as:

$$\mathbf{M} = \begin{pmatrix} M_{xx} & M_{xy} & M_{xz} \\ M_{xy} & M_{yy} & M_{yz} \\ M_{xz} & M_{yz} & M_{zz} \end{pmatrix} \quad (2.85)$$

Only principal diagonal components (M_{xx}, M_{yy}, M_{zz}) are used for the simulation. The governing equations for one-DOF rotating and translating body are given, which are solved by DFBI translation and motion solver to calculate the sinkage and trim of the hull. When the forces and moments are acquired by Equations (2.81) and (2.82), the motions of ship can be calculated by Equations (2.83) and (2.84). The numerical scheme of the body motions (Translational and Rotational) are derived in the **Appendix B**.

Chapter 3

Numerical Methods

The complex fluid flows and related phenomenon have already been developed by partial differential equation in Chapter 2. These complex equations cannot be solved analytically except in special case. Therefore numerical techniques are needed to solve these problem on the computer and so arise the discretization method: a method of approximating the differential equations by a system of algebraic equations for the variables at some set of discrete locations in space and time. This chapter will present discretization approaches, CFD technique, source of error and uncertainty which are based on Tu et al. [25] and Moukalled et al. [36].

3.1 Discretization Process

The numerical solution of a partial differential equation consists of finding the values of dependent variable ϕ at specified points from which its distribution over the domain of interest can be constructed. These points are called grid element. The resulting nodes or variable are generally positioned at cell centroids. The distribution of ϕ is hence discretized and converting the governing equation into a set of algebraic equations for the discrete values of ϕ as the discretization process and the specific methods employed to bring about this conversion as the discretization methods [36].

3.1.1 Geometric and Physical Modeling

A physical phenomenon cannot generally be considered as understood unless it can be mathematically formulated and this formulation tested and validated. A three dimensional domain could be turned into a two dimensional depiction, or symmetry can be taken into account to decrease the size of the study domain. In some cases, physical components may be removed and replaced with appropriate mathematical representation [36].

3.1.2 Domain Discretization

The geometric discretization of the physical domain results in a mesh on which the conservation equations are eventually solved. This requires the subdivision of the domain into discrete cells or elements that completely fill the computational domain to yield a grid or mesh system. The mesh system is composed of discrete elements defined by a set of vertices and boundary by faces. The mesh can be described from different perspectives.

At the most elementary level it is a list of vertices or points representing locations in one dimensional, two dimensional, or three dimensional. Elements are completely bounded by faces that are generally shared by neighboring element, except at the boundaries. The mesh faces, which are stored in a list, are of two types: (i) interior faces that are shared by (or connect) two elements, and (ii) boundary faces that coincide with the domain boundary; these boundary faces have only one contiguous element. While interior faces are derived from information related to the element topology, it is essential to provide boundary faces as they define the domain physical boundary. In two dimensions faces are described in terms of their defining points. In three dimensions the defining points describe edges that bound the face. The direction of the normal to an interior face is usually defined based on the topology of the neighboring elements. On the other hand, the direction of the normal to a boundary face always points outward of the domain [36].

3.2 Discretization of Governing Equations by FVM

The finite volume method (FVM) discretizes the integral form of the conservation equations directly in the physical space. It was initially introduced by the researchers such as McDonald [37] and MacCormack and Pauullay [38] for the solution of two-dimensional time-dependent Euler equations, and later extended to three-dimensional flows by Rizzi and Inouye [39]. The computational domain is subdivided into a finite number of contiguous control volumes, where the resulting statements express the exact conservation of relevant properties for each of the control volumes. At the centroid of each of the control volumes, the variable values are calculated. Interpolation is used to express variable values at the control volume surface in terms of the center values and suitable quadrature formulae are applied to approximate the surface and volume integrals [38]. An algebraic equation for each of the control volumes can be obtained, in which a number of the neighboring nodal values appeared.

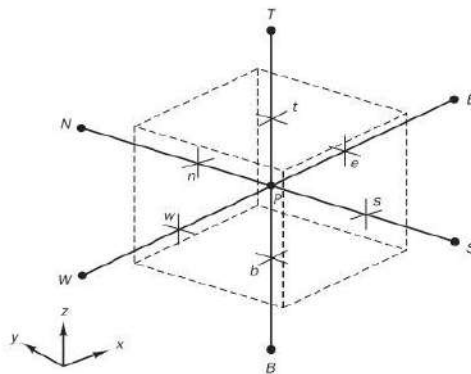


Fig. 3.1: A three dimensional control volume with CVs face [40]

The governing equations of fluid flow can be generalized by introducing a generic transport variable ϕ as there are significant commonalities between the fluid flow equations and written in the following form [25]:

$$\frac{\partial \phi}{\partial t} + \frac{\partial(u\phi)}{\partial x} + \frac{\partial(v\phi)}{\partial y} + \frac{\partial(w\phi)}{\partial z} = \frac{\partial}{\partial x} \left[\Gamma \frac{\partial \phi}{\partial x} \right] + \frac{\partial}{\partial y} \left[\Gamma \frac{\partial \phi}{\partial y} \right] + \frac{\partial}{\partial z} \left[\Gamma \frac{\partial \phi}{\partial z} \right] + S_\phi \quad (3.1)$$

Continuity

$$\phi = 1; \Gamma = 0; S_\phi = 0 \quad (3.2)$$

Momentum

$$\phi = u, v, w; \Gamma = \nu + \nu_t; S_\phi = -\frac{1}{\rho} \frac{\partial p}{\partial x}, -\frac{1}{\rho} \frac{\partial p}{\partial y}, -\frac{1}{\rho} \frac{\partial p}{\partial z} \quad (3.3)$$

Turbulent quantity

$$\phi = k, \varepsilon; \Gamma = \nu + \frac{\nu_t}{\sigma_k}, \nu + \frac{\nu_t}{\sigma_\varepsilon}; S_\phi = Q - \varepsilon, C_{\varepsilon 1} \frac{\varepsilon}{k} Q - C_{\varepsilon 2} \frac{\varepsilon^2}{k} \quad (3.4)$$

Here Γ is the diffusion coefficient and S_ϕ is the source term.

Eqn. (3.1) contains an unsteady term $\frac{\partial \phi}{\partial t}$ which can be approximated by applying the first-order forward-difference [40] scheme.

$$\frac{\partial \phi}{\partial t} = \frac{\phi_P^{n+1} - \phi_P^n}{\Delta t} \quad (3.5)$$

Where Δt is the incremental time step and the superscripts n and $n+1$ denote the previous and current time levels respectively.

By applying the finite volume-method based on the elemental volume (Fig. 3.1) the remaining term in Equation (3.1) become,

$$\begin{aligned} \frac{\partial(u\phi)}{\partial x} &= \frac{1}{\Delta V} \int_V \frac{\partial(u\phi)}{\partial x} dV = \frac{1}{\Delta V} \int_A (u\phi) dA^x \approx \frac{1}{\Delta V} \sum_{i=1}^6 (u\phi)_i A_i^x \\ &= \frac{1}{\Delta V} \left[(u\phi)_e A_e^x - (u\phi)_w A_w^x \right] \quad [\text{The projection area in the y and z direction are zero}] \end{aligned}$$

$$= \frac{1}{\Delta V} \left[(u_e \phi_e A_E - u_w \phi_w A_W) \right] \quad (3.6)$$

Using the Taylor series expansion, the interface values ϕ_e and ϕ_w at the respective cell face e and w can be obtained via linear interpolation between the neighboring points as

$$\phi_e = \frac{\phi_P + \phi_E}{2} \quad \phi_w = \frac{\phi_P + \phi_W}{2} \quad (3.7)$$

Using these relationship, Equation (3.6) becomes,

$$\frac{\partial(u\phi)}{\partial x} = \frac{1}{\Delta V} \left(u_e A_E \frac{\phi_P + \phi_E}{2} - u_w A_W \frac{\phi_P + \phi_W}{2} \right) \quad (3.8)$$

Similarly,

$$\frac{\partial(v\phi)}{\partial y} = \frac{1}{\Delta V} \left(v_n A_N \frac{\phi_P + \phi_N}{2} - v_s A_S \frac{\phi_P + \phi_S}{2} \right) \quad (3.9)$$

$$\frac{\partial(w\phi)}{\partial z} = \frac{1}{\Delta V} \left(w_t A_T \frac{\phi_P + \phi_T}{2} - w_b A_B \frac{\phi_P + \phi_B}{2} \right) \quad (3.10)$$

For the right hand side of Equation (3.1)

$$\begin{aligned} \frac{\partial}{\partial x} \left[\Gamma \frac{\partial \phi}{\partial x} \right] &= \frac{1}{\Delta V} \int_V \frac{\partial}{\partial x} \left(\Gamma \frac{\partial \phi}{\partial x} \right) dV = \frac{1}{\Delta V} \int_A \left(\Gamma \frac{\partial \phi}{\partial x} \right) dA^x \approx \frac{1}{\Delta V} \sum_{i=1}^6 \left(\Gamma \frac{\partial \phi}{\partial x} \right)_i A_i^x \\ &= \frac{1}{\Delta V} \left[\left(\Gamma \frac{\partial \phi}{\partial x} \right)_e A_e^x - \left(\Gamma \frac{\partial \phi}{\partial x} \right)_w A_w^x \right] \\ &= \frac{1}{\Delta V} \left[\left(\Gamma \frac{\partial \phi}{\partial x} \right)_e A_E - \left(\Gamma \frac{\partial \phi}{\partial x} \right)_w A_W \right] \end{aligned} \quad (3.11)$$

Assuming the linear gradient profile spanning the nodal points between P and E and between P and W to sufficiently approximate the first-order derivatives at e and w , the diffusive fluxes are evaluated as

$$\left(\Gamma \frac{\partial \phi}{\partial x} \right)_e A_E = \Gamma_e A_E \left(\frac{\phi_E - \phi_P}{\delta x_{PE}} \right) \quad (3.12)$$

$$\left(\Gamma \frac{\partial \phi}{\partial x} \right)_w A_W = \Gamma_w A_W \left(\frac{\phi_P - \phi_W}{\delta x_{PW}} \right) \quad (3.13)$$

Substituting these values into Equation (3.11)

$$\frac{\partial}{\partial x} \left[\Gamma \frac{\partial \phi}{\partial x} \right] = \frac{1}{\Delta V} \left[\Gamma_e A_E \left(\frac{\phi_E - \phi_P}{\delta x_{PE}} \right) - \Gamma_w A_W \left(\frac{\phi_P - \phi_W}{\delta x_{PW}} \right) \right] \quad (3.14)$$

Similarly,

$$\frac{\partial}{\partial y} \left[\Gamma \frac{\partial \phi}{\partial y} \right] = \frac{1}{\Delta V} \left[\Gamma_n A_N \left(\frac{\phi_N - \phi_P}{\delta x_{NE}} \right) - \Gamma_s A_S \left(\frac{\phi_P - \phi_S}{\delta x_{SW}} \right) \right] \quad (3.15)$$

$$\frac{\partial}{\partial z} \left[\Gamma \frac{\partial \phi}{\partial z} \right] = \frac{1}{\Delta V} \left[\Gamma_t A_T \left(\frac{\phi_T - \phi_P}{\delta x_{TE}} \right) - \Gamma_b A_B \left(\frac{\phi_P - \phi_B}{\delta x_{BW}} \right) \right] \quad (3.16)$$

And finally the remaining part,

$$\frac{1}{\Delta V} \int S_\phi dV = S_\phi \quad (3.17)$$

Where S_ϕ is assumed to be constant within the finite-control volume ΔV . Now it should be noted that a suitable time-marching procedure needs to appropriately update the property ϕ at the central point P and the neighboring points through time. Considering a time-marching procedure that requires the solution for all the variable at the time level $n+1$ and the Eqn. (3.1) can be written as,

$$\begin{aligned} & \frac{\phi_P^{n+1} - \phi_P^n}{\Delta t} + u_e^{n+1} A_E \frac{\phi_P^{n+1} + \phi_E^{n+1}}{2} - u_w^{n+1} A_W \frac{\phi_P^{n+1} + \phi_W^{n+1}}{2} + v_n^{n+1} A_N \frac{\phi_P^{n+1} + \phi_N^{n+1}}{2} - v_s^{n+1} A_S \frac{\phi_P^{n+1} + \phi_S^{n+1}}{2} \\ & + w_t^{n+1} A_T \frac{\phi_P^{n+1} + \phi_T^{n+1}}{2} - w_b^{n+1} A_B \frac{\phi_P^{n+1} + \phi_B^{n+1}}{2} = \Gamma_e^{n+1} A_E \left(\frac{\phi_E^{n+1} - \phi_P^{n+1}}{\delta x_{PE}} \right) - \Gamma_w^{n+1} A_W \left(\frac{\phi_P^{n+1} - \phi_W^{n+1}}{\delta x_{PW}} \right) \\ & + \Gamma_n^{n+1} A_N \left(\frac{\phi_N^{n+1} - \phi_P^{n+1}}{\delta x_{NE}} \right) - \Gamma_s^{n+1} A_S \left(\frac{\phi_P^{n+1} - \phi_S^{n+1}}{\delta x_{SW}} \right) + \Gamma_t^{n+1} A_T \left(\frac{\phi_T^{n+1} - \phi_P^{n+1}}{\delta x_{TE}} \right) - \Gamma_b^{n+1} A_B \left(\frac{\phi_P^{n+1} - \phi_B^{n+1}}{\delta x_{BW}} \right) + S_\phi^{n+1} \Delta V \end{aligned} \quad (3.18)$$

The property ϕ at the central point P as well as the properties at the neighboring points are required to be solved simultaneously and possibly coupling with other flow variables such as pressure and temperature appearing in the source term S_ϕ at the current time level within the same difference equation illustrated in the Fig. 3.2. In this implicit approach, the unknowns must be obtained by means of a simultaneous solution of the difference equations applied at all grid nodal points at a time level [25].

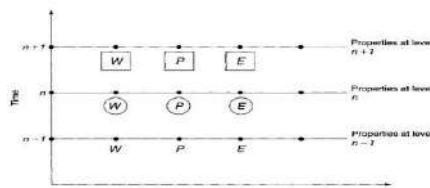


Fig. 3.2: Illustration of an implicit method [25]

3.3 Solution of Discretized Equations

The incompressible form of the conservation equations of governing the fluid flow are already derived. Solution to the governing equations is complicated by the lack of an independent equation for pressure. In each of the momentum equations, the fluid flow is driven by the contribution of the pressure gradients. With the additional equation provided by the continuity equation, the system of equations is self-contained; there are four equations for four dependents u, v, w , and p but no independent transport equation for pressure. The implication here is that the continuity and momentum equations are all required to solve for the velocity and pressure fields in an incompressible flow. In order to link the pressure with the velocity for an incompressible flow, one possible way is to construct the pressure field so as to guarantee conservation of the continuity equation [25]. The most popular schemes for pressure-velocity coupling for an incompressible flow belongs to the class of iterative methods, which is in a scheme called **SIMPLE** (Semi-Implicit Method for Pressure-Linkage Equations). This scheme was developed for practical engineering solutions by Patankar and Spalding [41]. However, this scheme must be extended to transient calculation due the problem contains unsteady term.

In this scheme, a guessed pressure field is used to solve the momentum equation. A pressure correction equation deduced from the continuity equation, is then solved to obtain a pressure correction field, which in turns is used to update the velocity and pressure fields. These guessed fields are progressively improved through the iteration process until convergence is achieved for the velocity and pressure fields.

3.4 Collocated Grid Arrangement

In the collocated grid arrangement (Fig. 3.3), all the flow-field variables including the velocities are stored at the same set of nodal points. Since many of the terms in each of the equations are essentially identical, the number of coefficients that must be computed and stored is minimized and the programming is simplified by this arrangement choice. A set of control volumes can be designed to fit the boundary including the discontinuity. Other arrangements of the variables lead to some of the variables being located at singularities of the grid, which may lead to singularities in the discretized equations. In a collocated grid, the coefficients of this equation cannot be directly computed, they are approximated by interpolation from the coefficients of the neighboring nodes.

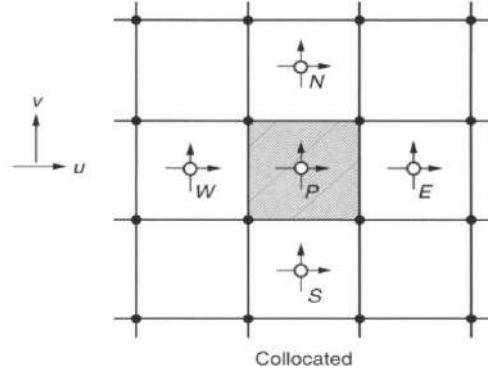


Fig. 3.3: Collocated grid arrangement of velocity components [25]

3.5 Semi Implicit Method for Pressure –Linked Equation (SIMPLE)

The problems associated with the non-linearities in the equation set and the pressure–velocity linkage can be resolved by adopting an iterative solution strategy such as the SIMPLE algorithm.

For the control volume shown in Fig. 3.4, the application of the finite-volume method to the continuity equation produces the following discretized form [42] of the equation

$$(u_{i,j,k} - u_{i-1,j,k})\Delta y\Delta z + (v_{i,j,k} - v_{i,j-1,k})\Delta x\Delta z + (w_{i,j,k} - w_{i,j,k-1})\Delta x\Delta y = 0 \quad (3.19)$$

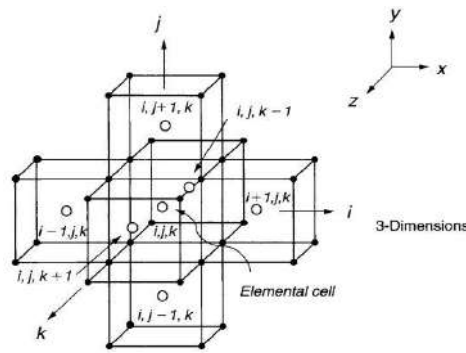


Fig. 3.4: Nodal indexing of elemental cell in three dimensions [25]

x -momentum equation

$$\frac{\partial u}{\partial t} + \frac{\partial(uu)}{\partial x} + \frac{\partial(uv)}{\partial y} + \frac{\partial(uw)}{\partial z} + \frac{1}{\rho} \frac{\partial p}{\partial x} = \nu \left(\frac{\partial^2 u}{\partial x^2} + \frac{\partial^2 u}{\partial y^2} + \frac{\partial^2 u}{\partial z^2} \right) \quad (3.20)$$

Integrating over the u -control volume, we can write,

$$\frac{\Delta x \Delta y \Delta z}{\Delta t} (u_{i,j,k} - u_{i,j,k}^n) + \iint \left[\frac{\partial}{\partial x} \left(u^2 - \nu \frac{\partial u}{\partial x} \right) + \frac{\partial}{\partial y} \left(uv - \nu \frac{\partial u}{\partial y} \right) + \frac{\partial}{\partial z} \left(uw - \nu \frac{\partial u}{\partial z} \right) \right] dx dy dz + \iint \frac{1}{\rho} \frac{\partial p}{\partial x} dx dy dz = 0 \quad (3.21)$$

Applying the Green's theorem to the above expression

$$\frac{\Delta x \Delta y \Delta z}{\Delta t} (u_{i,j,k} - u_{i,j,k}^n) + \left(L_{i+\frac{1}{2},j,k} - L_{i-\frac{1}{2},j,k} \right) \Delta y \Delta z + \left(M_{i,j+\frac{1}{2},k} - M_{i,j-\frac{1}{2},k} \right) \Delta x \Delta z + \left(N_{i,j,k+\frac{1}{2}} - N_{i,j,k-\frac{1}{2}} \right) \Delta x \Delta y + \frac{1}{\rho} \frac{\partial p}{\partial x} \Delta V = 0 \quad (3.22)$$

Where,

$$\left. \begin{aligned} L &= u^2 - \nu \frac{\partial u}{\partial x} \\ M &= uv - \nu \frac{\partial u}{\partial y} \\ N &= uw - \nu \frac{\partial u}{\partial z} \end{aligned} \right\} \quad (3.23)$$

are the axial, transverse and vertical fluxes of x-momentum.

$$L_{i+\frac{1}{2},j,k} = \frac{1}{4} (u_{i+1,j,k} + u_{i,j,k})^2 - \nu \frac{(u_{i+1,j,k} - u_{i,j,k})}{\Delta x} \quad (3.24)$$

$$L_{i-\frac{1}{2},j,k} = \frac{1}{4} (u_{i,j,k} + u_{i-1,j,k})^2 - \nu \frac{(u_{i,j,k} - u_{i-1,j,k})}{\Delta x} \quad (3.25)$$

$$M_{i,j+\frac{1}{2},k} = \frac{1}{4} (u_{i,j+1,k} + u_{i,j,k}) (v_{i+1,j,k} + v_{i,j,k}) - \nu \frac{(u_{i,j+1,k} - u_{i,j,k})}{\Delta y} \quad (3.26)$$

$$M_{i,j-\frac{1}{2},k} = \frac{1}{4} (u_{i,j,k} + u_{i,j-1,k}) (v_{i+1,j-1,k} + v_{i,j-1,k}) - \nu \frac{(u_{i,j,k} - u_{i,j-1,k})}{\Delta y} \quad (3.27)$$

$$N_{i,j,k+\frac{1}{2}} = \frac{1}{4} (u_{i,j,k+1} + u_{i,j,k}) (w_{i+1,j,k} + w_{i,j,k}) - \nu \frac{(u_{i,j,k+1} - u_{i,j,k})}{\Delta z} \quad (3.28)$$

$$N_{i,j,k-\frac{1}{2}} = \frac{1}{4} (u_{i,j,k} + u_{i,j,k-1}) (w_{i+1,j,k-1} + w_{i,j,k-1}) - \nu \frac{(u_{i,j,k} - u_{i,j,k-1})}{\Delta z} \quad (3.29)$$

Substituting above terms in Equation (3.22) get

$$\begin{aligned} & \frac{\Delta x \Delta y \Delta z}{\Delta t} (u_{i,j,k} - u_{i,j,k}^n) \\ & + u_{i,j,k} \left\{ \frac{1}{4} (u_{i+1,j,k} + u_{i,j,k}) \Delta y \Delta z + \frac{\nu \Delta y \Delta z}{\Delta x} \right\} + u_{i+1,j,k} \left\{ \frac{1}{4} (u_{i+1,j,k} + u_{i,j,k}) \Delta y \Delta z - \frac{\nu \Delta y \Delta z}{\Delta x} \right\} \\ & - u_{i,j,k} \left\{ \frac{1}{4} (u_{i,j,k} + u_{i-1,j,k}) \Delta y \Delta z - \frac{\nu \Delta y \Delta z}{\Delta x} \right\} - u_{i-1,j,k} \left\{ \frac{1}{4} (u_{i,j,k} + u_{i-1,j,k}) \Delta y \Delta z + \frac{\nu \Delta y \Delta z}{\Delta x} \right\} \end{aligned}$$

$$\begin{aligned}
 & +u_{i,j,k} \left\{ \frac{1}{4} (v_{i+1,j,k} + v_{i,j,k}) \Delta x \Delta z + \frac{\nu \Delta x \Delta z}{\Delta y} \right\} + u_{i,j+1,k} \left\{ \frac{1}{4} (v_{i+1,j,k} + v_{i,j,k}) \Delta x \Delta z - \frac{\nu \Delta x \Delta z}{\Delta y} \right\} \\
 & -u_{i,j,k} \left\{ \frac{1}{4} (v_{i+1,j-1,k} + v_{i,j-1,k}) \Delta x \Delta z - \frac{\nu \Delta x \Delta z}{\Delta y} \right\} - u_{i,j-1,k} \left\{ \frac{1}{4} (v_{i+1,j-1,k} + v_{i,j-1,k}) \Delta x \Delta z + \frac{\nu \Delta x \Delta z}{\Delta y} \right\} \\
 & +u_{i,j,k} \left\{ \frac{1}{4} (w_{i+1,j,k} + w_{i,j,k}) \Delta x \Delta y + \frac{\nu \Delta x \Delta y}{\Delta z} \right\} + u_{i,j,k+1} \left\{ \frac{1}{4} (w_{i+1,j,k} + w_{i,j,k}) \Delta x \Delta y - \frac{\nu \Delta x \Delta y}{\Delta z} \right\} \\
 & -u_{i,j,k} \left\{ \frac{1}{4} (w_{i+1,j,k-1} + w_{i,j,k-1}) \Delta x \Delta y - \frac{\nu \Delta x \Delta y}{\Delta z} \right\} - u_{i,j,k-1} \left\{ \frac{1}{4} (w_{i+1,j,k-1} + w_{i,j,k-1}) \Delta x \Delta y + \frac{\nu \Delta x \Delta y}{\Delta z} \right\} + \frac{1}{\rho} \frac{\partial p}{\partial x} \Delta V = 0 \quad (3.30)
 \end{aligned}$$

or,

$$\begin{aligned}
 & \left[\frac{\Delta x \Delta y \Delta z}{\Delta t} + \frac{1}{4} (u_{i+1,j,k} + u_{i,j,k}) \Delta y \Delta z - \frac{1}{4} (u_{i,j,k} + u_{i-1,j,k}) \Delta y \Delta z + \frac{1}{4} (v_{i+1,j,k} + v_{i,j,k}) \Delta x \Delta z \right. \\
 & - \frac{1}{4} (v_{i+1,j-1,k} + v_{i,j-1,k}) \Delta x \Delta z + \frac{1}{4} (w_{i+1,j,k} + w_{i,j,k}) \Delta x \Delta y - \frac{1}{4} (w_{i+1,j,k-1} + w_{i,j,k-1}) \Delta x \Delta y \\
 & \left. + \frac{\nu \Delta y \Delta z}{\Delta x} + \frac{\nu \Delta y \Delta z}{\Delta x} + \frac{\nu \Delta x \Delta z}{\Delta y} + \frac{\nu \Delta x \Delta z}{\Delta y} + \frac{\nu \Delta x \Delta y}{\Delta z} + \frac{\nu \Delta x \Delta y}{\Delta z} \right] u_{i,j,k} \\
 & + \left[u_{i+1,j,k} \left\{ \frac{1}{4} (u_{i+1,j,k} + u_{i,j,k}) \Delta y \Delta z - \frac{\nu \Delta y \Delta z}{\Delta x} \right\} - u_{i-1,j,k} \left\{ \frac{1}{4} (u_{i,j,k} + u_{i-1,j,k}) \Delta y \Delta z + \frac{\nu \Delta y \Delta z}{\Delta x} \right\} \right. \\
 & + u_{i,j+1,k} \left\{ \frac{1}{4} (v_{i+1,j,k} + v_{i,j,k}) \Delta x \Delta z - \frac{\nu \Delta x \Delta z}{\Delta y} \right\} - u_{i,j-1,k} \left\{ \frac{1}{4} (v_{i+1,j-1,k} + v_{i,j-1,k}) \Delta x \Delta z + \frac{\nu \Delta x \Delta z}{\Delta y} \right\} \\
 & \left. + u_{i,j,k+1} \left\{ \frac{1}{4} (w_{i+1,j,k} + w_{i,j,k}) \Delta x \Delta y - \frac{\nu \Delta x \Delta y}{\Delta z} \right\} - u_{i,j,k-1} \left\{ \frac{1}{4} (w_{i+1,j,k-1} + w_{i,j,k-1}) \Delta x \Delta y + \frac{\nu \Delta x \Delta y}{\Delta z} \right\} \right] \\
 & - \frac{\Delta x \Delta y \Delta z}{\Delta t} u_{i,j,k}^n + \frac{1}{\rho} \frac{\partial p}{\partial x} \Delta V = 0 \quad (3.31)
 \end{aligned}$$

The above equation can be written as,

$$\left(\frac{\Delta x \Delta y \Delta z}{\Delta t} + a_{i,j,k}^u \right) u_{i,j,k} = \sum a_{nb}^u u_{nb} + b^u - \frac{1}{\rho} \frac{\partial p}{\partial x} \Delta V \quad (3.32)$$

In this equation $\sum a_{nb}^u u_{nb}$ signifies all the convective and diffusive contribution from the neighboring nodes. The coefficients $a_{i,j,k}^u$ and a_{nb}^u contain grid size. $b^u = \frac{\Delta x \Delta y \Delta z}{\Delta t} u_{i,j,k}^n$.

Similarly for y and z momentum equation can be written as

$$\left(\frac{\Delta x \Delta y \Delta z}{\Delta t} + a_{i,j,k}^v \right) v_{i,j,k} = \sum a_{nb}^v u_{nb} + b^v - \frac{1}{\rho} \frac{\partial p}{\partial y} \Delta V \quad (3.33)$$

$$\left(\frac{\Delta x \Delta y \Delta z}{\Delta t} + a_{i,j,k}^w \right) w_{i,j,k} = \sum a_{nb}^w u_{nb} + b^w - \frac{1}{\rho} \frac{\partial p}{\partial y} \Delta V \quad (3.34)$$

3.5.1 Solution Algorithm

When solving an unsteady problem, the time step is chosen so that an accurate history is obtained. Due to the non-linearity and coupling of the underlying differential equations iterative solution is the only choice. For an unsteady flow and time accuracy is required, iteration must be continued within each time step until the entire system of non-linear equations is satisfied to within a narrow tolerance. The iterative SIMPLE calculation process begins by guessing the pressure field, p^* . During the iterative process, the discretized momentum equations are solved using the guessed pressure field [25]. Applying the finite-volume method, the equations for the x, y, and z momentum that yield the velocity components u^* , v^* , and w^* , can be expressed in the same algebraic equations same as Equations (3.32), (3.33), and (3.34)

$$\left(\frac{\Delta x \Delta y \Delta z}{\Delta t} + a_{i,j,k}^u \right) u_{i,j,k}^* = \sum a_{nb}^u u_{nb}^* + b^{u'} - \frac{1}{\rho} \frac{\partial p^*}{\partial x} \Delta V \quad (3.35)$$

$$\left(\frac{\Delta x \Delta y \Delta z}{\Delta t} + a_{i,j,k}^v \right) v_{i,j,k}^* = \sum a_{nb}^v v_{nb}^* + b^{v'} - \frac{1}{\rho} \frac{\partial p^*}{\partial y} \Delta V \quad (3.36)$$

$$\left(\frac{\Delta x \Delta y \Delta z}{\Delta t} + a_{i,j,k}^w \right) w_{i,j,k}^* = \sum a_{nb}^w w_{nb}^* + b^{w'} - \frac{1}{\rho} \frac{\partial p^*}{\partial z} \Delta V \quad (3.37)$$

Here, we simplify the above expressions by introducing a_{nb} to represent the presence of neighboring coefficients, and u_{nb}^* , v_{nb}^* , and w_{nb}^* to denote the neighboring nodal velocity components. If we define the correction p' as the difference between the correct pressure field and the guessed pressure field, we obtain

$$p = p^* + p' \quad (3.38)$$

Similarly, we can also define for the velocity components

$$\left. \begin{aligned} u &= u^* + u' \\ v &= v^* + v' \\ w &= w^* + w' \end{aligned} \right\} \quad (3.39)$$

The algebraic form of the correct velocities can also be similarly expressed as in Equations (3.35), (3.36), and (3.37)

$$\left(\frac{\Delta x \Delta y \Delta z}{\Delta t} + a_{i,j,k}^u \right) u_{i,j,k} = \sum a_{nb}^u u_{nb} + b^{u'} - \frac{1}{\rho} \frac{\partial p}{\partial x} \Delta V \quad (3.40)$$

$$\left(\frac{\Delta x \Delta y \Delta z}{\Delta t} + a_{i,j,k}^v \right) v_{i,j,k} = \sum a_{nb}^v v_{nb} + b^{v'} - \frac{1}{\rho} \frac{\partial p}{\partial y} \Delta V \quad (3.41)$$

$$\left(\frac{\Delta x \Delta y \Delta z}{\Delta t} + a_{i,j,k}^w \right) w_{i,j,k} = \sum a_{nb}^w w_{nb} + b^{w'} - \frac{1}{\rho} \frac{\partial p}{\partial z} \Delta V \quad (3.42)$$

Subtracting Equations (3.40) and (3.35), (3.41) and (3.36), and (3.42) and (3.37)

$$\left(\frac{\Delta x \Delta y \Delta z}{\Delta t} + a_{i,j,k}^u \right) (u_{i,j,k} - u_{i,j,k}^*) = \sum a_{nb}^u (u_{nb} - u_{nb}^*) - \frac{1}{\rho} \frac{\partial (p - p^*)}{\partial x} \Delta V \quad (3.43)$$

$$\left(\frac{\Delta x \Delta y \Delta z}{\Delta t} + a_{i,j,k}^v \right) (v_{i,j,k} - v_{i,j,k}^*) = \sum a_{nb}^v (v_{nb} - v_{nb}^*) - \frac{1}{\rho} \frac{\partial (p - p^*)}{\partial y} \Delta V \quad (3.44)$$

$$\left(\frac{\Delta x \Delta y \Delta z}{\Delta t} + a_{i,j,k}^w \right) (w_{i,j,k} - w_{i,j,k}^*) = \sum a_{nb}^w (w_{nb} - w_{nb}^*) - \frac{1}{\rho} \frac{\partial (p - p^*)}{\partial z} \Delta V \quad (3.45)$$

Using the correction formula Equations (3.43), (3.44), and (3.45) can be rewritten as

$$\left(\frac{\Delta x \Delta y \Delta z}{\Delta t} + a_{i,j,k}^u \right) u'_{i,j,k} = \sum a_{nb}^u u'_{nb} - \frac{1}{\rho} \frac{\partial p'}{\partial x} \Delta V \quad (3.46)$$

$$\left(\frac{\Delta x \Delta y \Delta z}{\Delta t} + a_{i,j,k}^v \right) v'_{i,j,k} = \sum a_{nb}^v v'_{nb} - \frac{1}{\rho} \frac{\partial p'}{\partial y} \Delta V \quad (3.47)$$

$$\left(\frac{\Delta x \Delta y \Delta z}{\Delta t} + a_{i,j,k}^w \right) w'_{i,j,k} = \sum a_{nb}^w w'_{nb} - \frac{1}{\rho} \frac{\partial p'}{\partial z} \Delta V \quad (3.48)$$

The SIMPLE scheme approximate the above three equations by omissions of terms $\sum a_{nb}^u u'_{nb}$, $\sum a_{nb}^v v'_{nb}$ and $\sum a_{nb}^w w'_{nb}$. This scheme is an iterative approach and we are allowed to construct a formula for p' that is simply a numerical artifice with the aim to expedite the convergence of the velocity field to a solution that satisfies the continuity equation. Once the pressure correction field is known, the correct velocities $u, v,$ and w can be obtained through the guessed velocities $u^*, v^*,$ and w^* from the simplified equations (3.46), (3.47), and (3.48)

$$u_{i,j,k} = u_{i,j,k}^* - F^u \frac{\partial p'}{\partial x} \quad (3.49)$$

$$v_{i,j,k} = v_{i,j,k}^* - F^v \frac{\partial p'}{\partial y} \quad (3.50)$$

$$w_{i,j,k} = w_{i,j,k}^* - F^w \frac{\partial p'}{\partial z} \quad (3.51)$$

Where,

$$F^u = \frac{\Delta V}{\rho \left(\frac{\Delta x \Delta y \Delta z}{\Delta t} + a_{i,j,k}^u \right)} \quad F^v = \frac{\Delta V}{\rho \left(\frac{\Delta x \Delta y \Delta z}{\Delta t} + a_{i,j,k}^v \right)} \quad F^w = \frac{\Delta V}{\rho \left(\frac{\Delta x \Delta y \Delta z}{\Delta t} + a_{i,j,k}^w \right)}$$

These correction formulae can be applied to any location, where the velocity components reside within the computational grid. The general form of the velocity correction formulae, by removing the subscript i, j, k can be written as

$$u = u^* - F^u \frac{\partial p'}{\partial x} \quad (3.52)$$

$$v = v^* - F^v \frac{\partial p'}{\partial y} \quad (3.53)$$

$$w = w^* - F^w \frac{\partial p'}{\partial z} \quad (3.54)$$

By differentiating Equations (3.52), (3.53), and (3.54) by the Cartesian direction x , y , and z respectively and summing them together [25]

$$\frac{\partial u}{\partial x} + \frac{\partial v}{\partial y} + \frac{\partial w}{\partial z} = \frac{\partial u^*}{\partial x} + \frac{\partial v^*}{\partial y} + \frac{\partial w^*}{\partial z} - \frac{\partial}{\partial x} \left(F^u \frac{\partial p'}{\partial x} \right) - \frac{\partial}{\partial y} \left(F^v \frac{\partial p'}{\partial y} \right) - \frac{\partial}{\partial z} \left(F^w \frac{\partial p'}{\partial z} \right) \quad (3.55)$$

But,

$$\frac{\partial u}{\partial x} + \frac{\partial v}{\partial y} + \frac{\partial w}{\partial z} = 0 \quad (3.56)$$

$$\frac{\partial}{\partial x} \left(F^u \frac{\partial p'}{\partial x} \right) + \frac{\partial}{\partial y} \left(F^v \frac{\partial p'}{\partial y} \right) + \frac{\partial}{\partial z} \left(F^w \frac{\partial p'}{\partial z} \right) = \frac{\partial u^*}{\partial x} + \frac{\partial v^*}{\partial y} + \frac{\partial w^*}{\partial z} \quad (3.57)$$

Once the pressure correction is obtained from Equation (3.57), the pressure and velocity components are subsequently updated through the correction formulae of Equations (3.52), (3.53), and (3.54). The right hand side of Equation (3.57) commonly known as the **mass residual**. The sequence of operations in CFD process that embodies the transient SIMPLE scheme is given in Fig. 3.5.

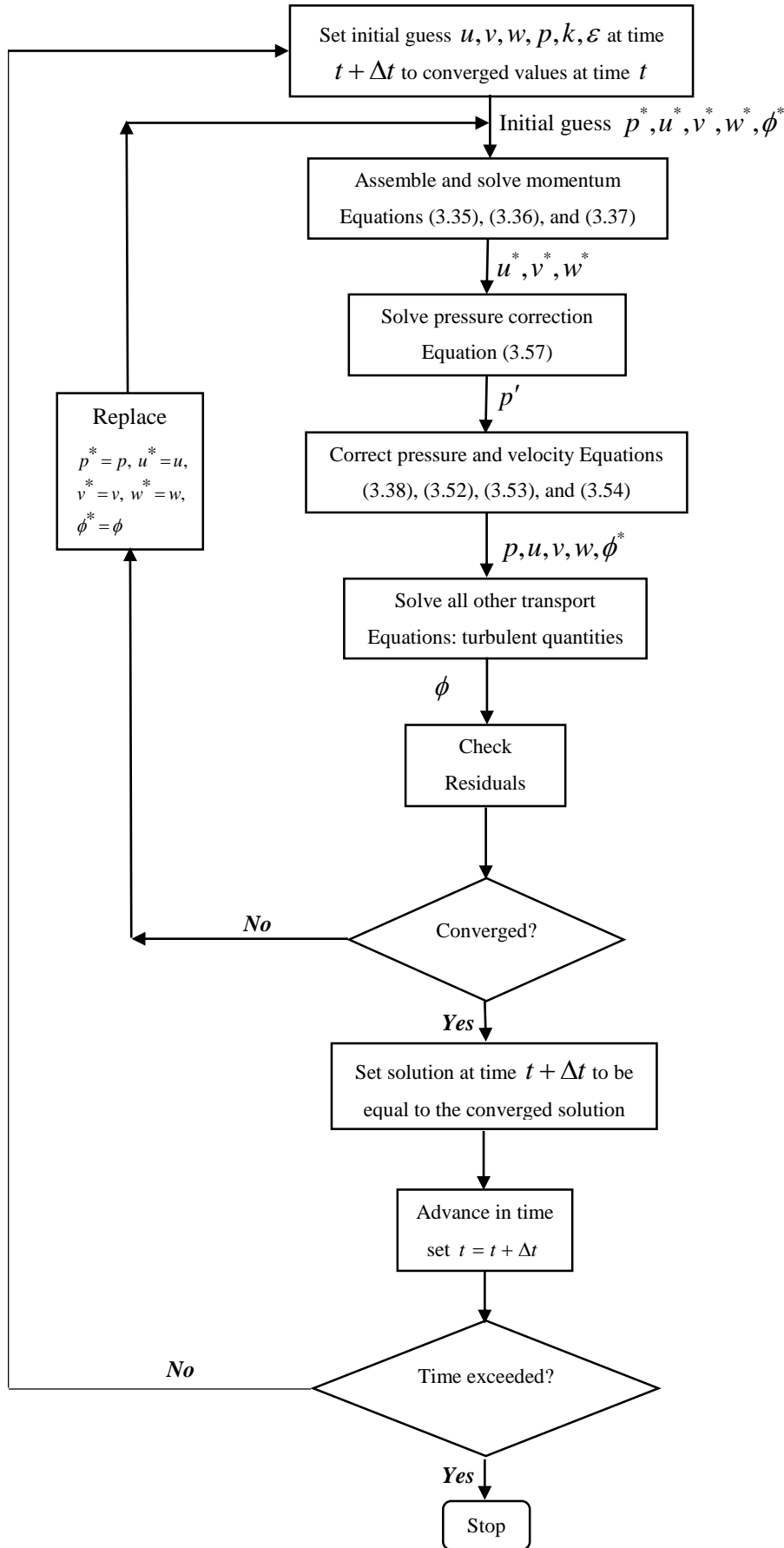


Fig. 3.5: Solution algorithm of Transient SIMPLE Scheme [25, 36]

3.6 Convergence

Convergence of a numerical process can be stated as the solution of the system of algebraic equations approaching the true solution of the partial differential equations having the same initial and boundary conditions as the refined grid system. In the majority of commercial CFD code, the system of algebraic equations is usually solved iteratively. When dealing with these codes, there are three important aspects to abide by for the iterative convergence. First, all the discretized equations are needed to be converged when they reach a specified tolerance at every nodal section. Second, the numerical solution no longer changes with additional iterations. Third, overall mass, momentum and scalar balances are obtained. During the numerical procedure, the imbalances of the discretized equations are monitored and these defects are commonly referred to as the residuals of the system of algebraic equations that is they measure the extent of imbalances arising from these equations and terminate the numerical process when a specified tolerance is reached. For satisfactory convergence, the residuals should diminish as the numerical process progresses [25].

For any transport variable ϕ , the discretized form of the partial differential equation can be specially written as:

$$a_{i,j,k}\phi_{i,j,k} = \sum a_{nb}\phi_{nb} + b_{i,j,k} \quad (3.58)$$

In the equation (3.58) the central coefficient $a_{i,j,k}$ and neighboring coefficients a_{nb} normally depend on the solution of other flow-field variables including the time and spatial varying fluid-flow properties. These coefficients are updated consecutively during the iterative procedure. At the start of each iteration step, the equality in equation (3.58) will not hold. Therefore, rewrite the above equation by introducing an imbalance variable called residual $R_{i,j,k}$ and the above is re-expressed as

$$R_{i,j,k} = \sum a_{nb}\phi_{nb} + b_{i,j,k} - a_{i,j,k}\phi_{i,j,k} \quad (3.59)$$

For a well-posed formulation, the residuals become negligible with increasing iterations. In CFD, residuals are employed to monitor the behavior of the numerical process. Importantly, they implicate whether the solution shows a trend of convergence or divergence.

The residual actually depicts the imbalance at the nodal point for one cell volume. For practical purposes, a global residual R , taken as the sum of the each local residual $R_{i,j,k}$ over all the grid nodal points, is monitored:

$$R = \sum_{\text{grid points}} |R_{i,j,k}| \quad (3.60)$$

Convergence is deemed to be achieved for the discretized equation so long as the global residual R satisfies a specified tolerance, that is

$$R \leq \varepsilon \text{ or } \sum_{\text{grid points}} |R_{i,j,k}| \leq \varepsilon \quad (3.61)$$

The variable ε is usually referred to as the convergence tolerance for the system of algebraic equations. Specifying appreciably small tolerance values will incur a large number of iteration steps in reaching convergence. On the other hand, large tolerance values constitute an early termination of the iteration process for which the numerical solution of the algebraic equations is considered to be rather coarse or not sufficiently converged. The residual convergence study for each hull is drawn from the simulation and given in *Appendix C*.

3.7 Grid Dependence and Validation

In CFD problem, uncertainties can arise while performing a numerical simulation. These can be due to the improper modeling of physics such as a misunderstanding of the phenomenon leading to falsifying assumptions or incorrect computational design such as making wrong approximations and simplifications about the parameters that governs the fluid dynamics. Therefore, it requires a detailed analysis to be performed to quantify the modeling and numerical uncertainties in the simulation. Grid dependence and validation procedures are the means by which a CFD solution can be properly assessed through quantitatively estimating the inherent errors and uncertainties.

Grid dependence can be defined as a process for assessing the numerical simulation uncertainty and the dependence of the numerical results on the grid refinement.

Validation can be defined as a process for assessing simulation model uncertainty by using benchmark experimental data and when conditions permit, estimating the sign and magnitude of the simulation modeling error itself [25].

The grid dependence and validation methodology are discussed following the published literatures by Stern et al. [43] and Wilson et al. [44].

3.7.1 Grid Dependence Test

The test methodology starts with the grid convergence study. For convergence studies ITTC [45] recommends a grid refinement ratio $r_G = \sqrt{2}$, as it provides fairly large parameter refinement ratio. Convergence studies require a minimum of $m=3$ solutions to evaluate convergence with respect to input parameter. Changes between medium-fine and coarse-medium can be written as

$$\begin{aligned}\varepsilon_{21} &= S_2 - S_1 \\ \varepsilon_{32} &= S_3 - S_2\end{aligned}\tag{3.62}$$

S_1, S_2 , and S_3 are stand for fine, medium and coarse solution. Convergence ratio is defined as

$$R_G = \frac{\varepsilon_{21}}{\varepsilon_{32}} = \frac{S_2 - S_1}{S_3 - S_2}\tag{3.63}$$

Three convergence conditions are possible:

- i. Monotonic convergence: $0 < R_G < 1$
- ii. Oscillatory convergence: $R_G < 0$
- iii. Divergence: $R_G > 1$

For monotonic convergence, generalized Richardson Extrapolation (RE) [44] is used to estimate the grid uncertainty U_G . For oscillatory convergence, uncertainties can be estimated, but not the signs and magnitudes of the errors. Uncertainties are estimated based on determination of the upper (S_U) and lower (S_L) bounds of the solution oscillation, which requires more than three solutions. The estimate of uncertainty is based on half the solution range

$$U_G = \frac{1}{2}(S_U - S_L)\tag{3.64}$$

For divergence, errors and uncertainties cannot be estimated. The preparation and verification steps must be reconsidered.

In case of monotonic convergence, an error δ_{RE} due to the selection of r^{th} input parameters and the order of accuracy can be estimated as,

$$\delta_{RE} = \frac{\varepsilon_{21}}{r_G^{p_G} - 1} \quad (3.65)$$

$$p_G = \frac{\ln(\varepsilon_{32}/\varepsilon_{21})}{\ln(r_G)} \quad (3.66)$$

Correction of Equation (3.65) through a multiplication factor C_G provides a quantitative metric to determine proximity of the solutions to the asymptotic range. Where the correction factor is given by,

$$C_G = \frac{r_G^{p_G} - 1}{r_G^{p_{G_{east}}} - 1} \quad (3.67)$$

When solutions are beyond the asymptotic range, C_G is sufficiently less than or greater than 1, the magnitude of error is determined through the estimation of grid uncertainty, U_G given by

$$U_G = |C_G \delta_{RE}| + |(1 - C_G) \delta_{RE}| \quad (3.68)$$

3.7.2 Validation Procedure

Validation is targeted through the comparison of simulations with benchmark experimental fluid dynamics (EFD) data. The comparison error E is defined by,

$$E = S - D \quad (3.69)$$

S is the simulation result and D is the experimental data. The validation of the numerical results are achieved when the comparison relative error $|E|$ becomes less than the validation uncertainty U_V level.

The validation uncertainty $|U_V|$ is given by,

$$U_V = \sqrt{U_{SN}^2 + U_D^2} \quad (3.70)$$

U_{SN} is the numerical uncertainty and found by

$$U_{SN} = \sqrt{U_G^2 + U_I^2} \quad (3.71)$$

U_G is the grid uncertainty given in the Equation (3.68) and U_I is the iterative uncertainty.

Chapter 4

Computational Setup

The whole simulation is carried out in commercial CFD code STAR-CCM+ version 14.02.010. The processes required to run the simulation will be presented and the guidelines for the best approaches are selected with the aid of STAR-CCM+ user guide [30].

4.1 Co-ordinate System

A Cartesian coordinate system $Oxyz$ is fixed in the model ship and the origin at the intersection of the planes of the mid-ship section and the undisturbed free surface level as shown in Fig. 4.1. The x direction is positive towards the forward part of the ship, y direction is positive to the port side and z direction is positive in the vertically upward direction. The model ship is fixed in the position and the free stream velocity, U is parallel to the negative x direction.

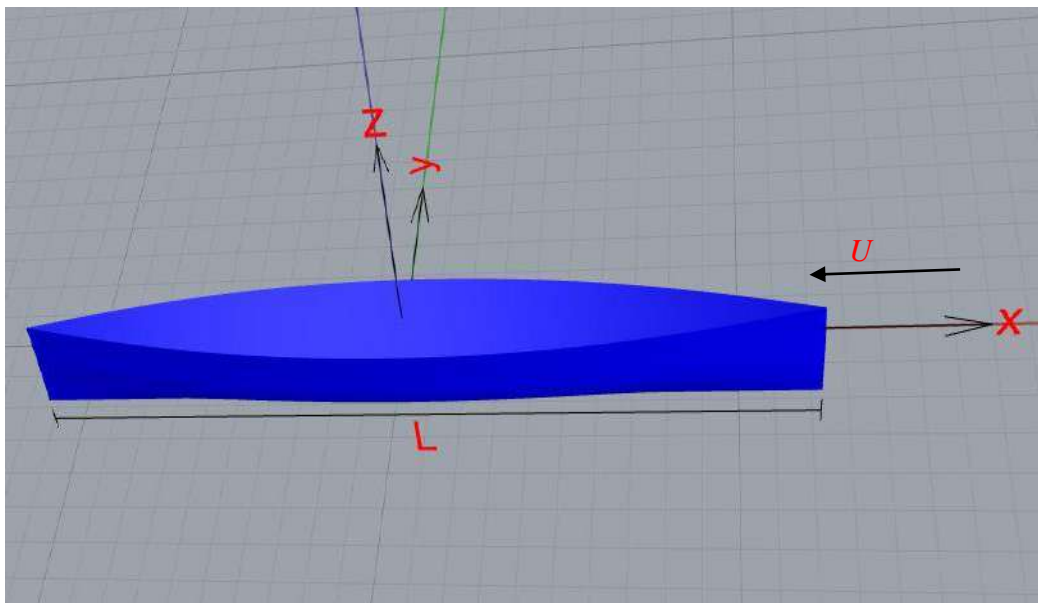


Fig. 4.1: Coordinate system used in this present study

4.2 Boundary Conditions

The general view of the computational domain including the ship hull and the notations of its boundary conditions is depicted in Fig. 4.2. The computational domain is split into two sub-domains (air and water) and has an interface between the flow fluids. This entire computational domain is bounded by six boundary surfaces such as inlet, outlet, side, symmetry, top and bottom.

The boundary conditions imposed on each surface are described below (Masuko and Ogiwara [46]).

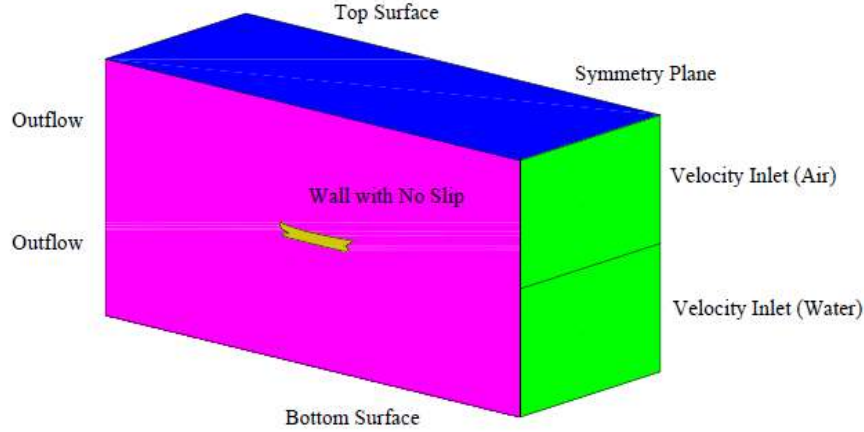


Fig. 4.2: Computational domain and its boundary conditions

- (a) **Inlet boundary:** Similar to inviscid flow problem, the initial velocity components in x, y and z direction are selected as,

$$u(x) = \bar{u} \quad \text{and} \quad \bar{v} = w = 0 \quad (4.1)$$

- (b) **Outlet boundary:** The pressure at outlet is assumed to be the hydrostatic on the free surface and the shear forces are prescribed zero in order to meet the criteria of stress continuity equation.

$$\frac{\partial \bar{u}}{\partial n} = \frac{\partial \bar{v}}{\partial n} = \frac{\partial \bar{w}}{\partial n} = 0 \quad (4.2)$$

- (c) **Side and Symmetry boundary:** The axis of symmetry of the computational domain and the surface of symmetry (side) plane can be considered as the boundaries. The net flow across the symmetry is zero and hence the velocity including the turbulent quantities normal to the boundary is set to zero.

$$\bar{v} = 0, \quad \frac{\partial \bar{u}}{\partial n} = \frac{\partial \bar{w}}{\partial n} = \frac{\partial k}{\partial n} = \frac{\partial \varepsilon}{\partial n} = 0 \quad (4.3)$$

- (d) **Top and Bottom boundary:** The top and bottom boundaries are considered to be the wall type and can be written as,

$$\bar{u} = \bar{v} = \bar{w} = k = \varepsilon = 0 \quad (4.4)$$

(e) **Ship hull:** The velocity components (no-slip) and the turbulent quantities on the hull are set to zero.

$$\bar{u} = \bar{v} = \bar{w} = k = \varepsilon = 0 \quad (4.5)$$

(f) **Wall function:** The wall function emulates the behaviour of the flow inside the boundary layer. On the first grid point of the body k and ε become:

$$k = \frac{u_{\tau}^2}{\sqrt{\beta}}, \quad \varepsilon = \beta^{3/4} \frac{k^{3/2}}{ky} \quad (4.6)$$

Towards the outer part of the viscous sub layer and the buffer layer, the turbulence is rapidly increased by the production of turbulent kinetic energy. With the use of standard k - ε turbulence model, additional wall functions are necessary to bridge the solution variables in the viscosity affected region. The velocity in the log-law region varies logarithmically with y^+ as given by Equation (4.7). Although there is a slight variation in the values of universal constants in the literature, according to Stanford conventions suggest the von Karman constant κ as 0.41 and the equation constant B as 5.0.

$$u^+ = \frac{1}{\kappa} \ln(y^+) + B \quad (4.7)$$

Where u^+ is the stream wise velocity non-dimensionalized by the friction velocity u_{τ} , y^+ is the normalized wall distance such that $y^+ = y u_{\tau} / \nu$. At the upstream boundary, the uniform flow condition is used. At the downstream boundary, zero derivative condition in x -direction is used and the pressure p is taken as hydrostatic. At the symmetry plane boundaries zero derivative condition in the normal directions are utilized.

4.3 Mesh Generation

The mesh generation constitutes one of the most important steps during pre-process stage after the definition of the domain geometry. CFD requires the subdivision of the domain into a number of smaller, non-overlapping subdomains in order to solve the flow physics within the domain geometry that is created: this yields the generation of mesh of cells. The essential fluid

flows that are described in each of these cells are usually solved numerically so that discrete values of the flow properties such as the velocity, pressure, and the other transport properties of interests are determined. This yields the CFD solution to the flow problem that is being solved. The accuracy of a CFD solution is governed by the number of cells in the mesh within the computational domain.

4.3.1 Surface Mesh

In STAR-CCM+ meshing models are split into two groups: surface mesh models and volume mesh models. Meshing strategy begins with the surface meshing modeling and when a high-quality surface mesh is achieved, go on to the volume meshing models [30]. There are two types of surface meshing model: *Surface remesher* and *Surface wrapper*.

To obtain a best surface mesh a global setting with the selection of base size is required in the problem simulation. The *Base Size* is a characteristic dimension of the model that has been set before using any relative values. This base size determines the number of cells within the domain are generated. It is noted that lower the base size will generate the higher cells and vice versa. However, it is recommended that the value of base size should be equal to the $1/40^{\text{th}}$ to $1/60^{\text{th}}$ of the length of the hull. Base size is the only a global setting which controls the size of the whole mesh but it is also allowed to control the surface of the interests based on the base size. As the faces of the computational domain are smooth and rectangular in shape, surface mesh is generated with an acceptable view as shown in Fig. 4.3.

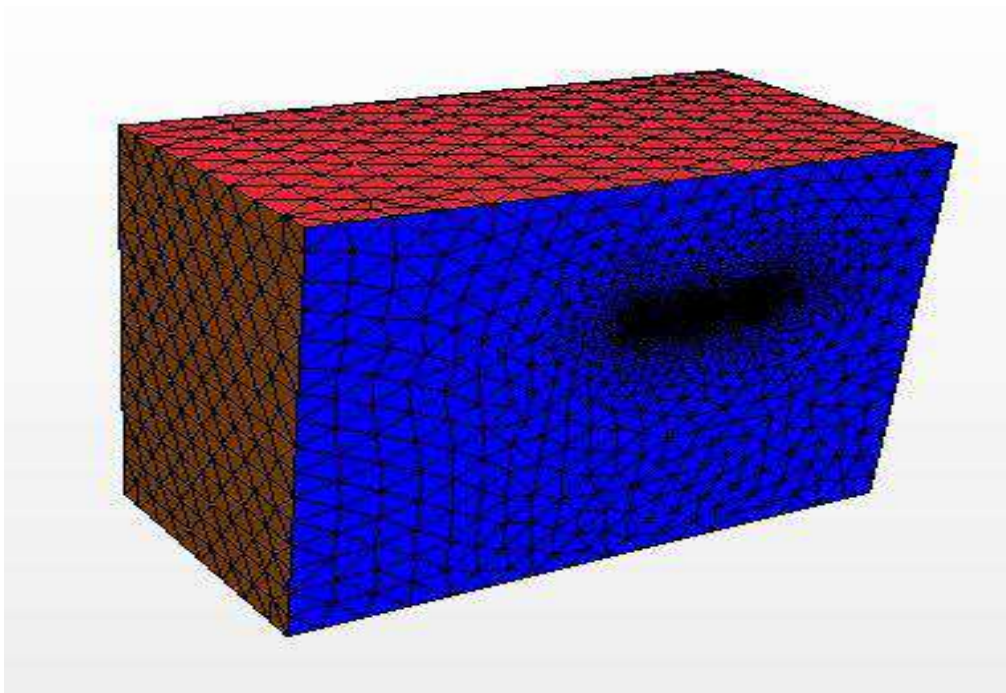


Fig. 4.3: Surface mesh of the computational domain

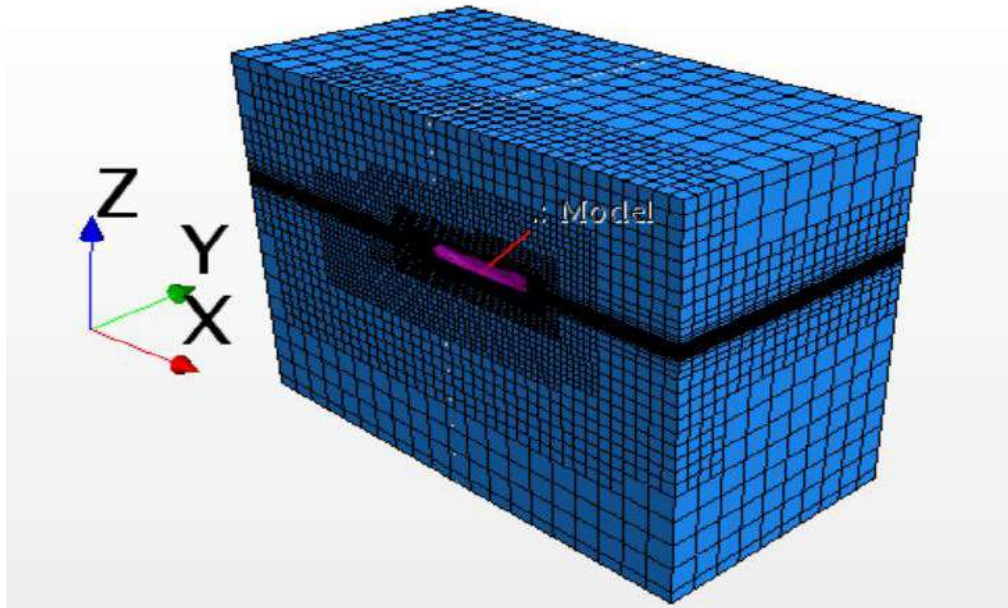
However, the hull geometry which is a really complex one, surface control is mandatory to generate the acceptable surface mesh. And so, beyond the global base size, relative values are set as a percentage of the base size at the complex geometry of the hull surface as shown in Fig. 4.4.



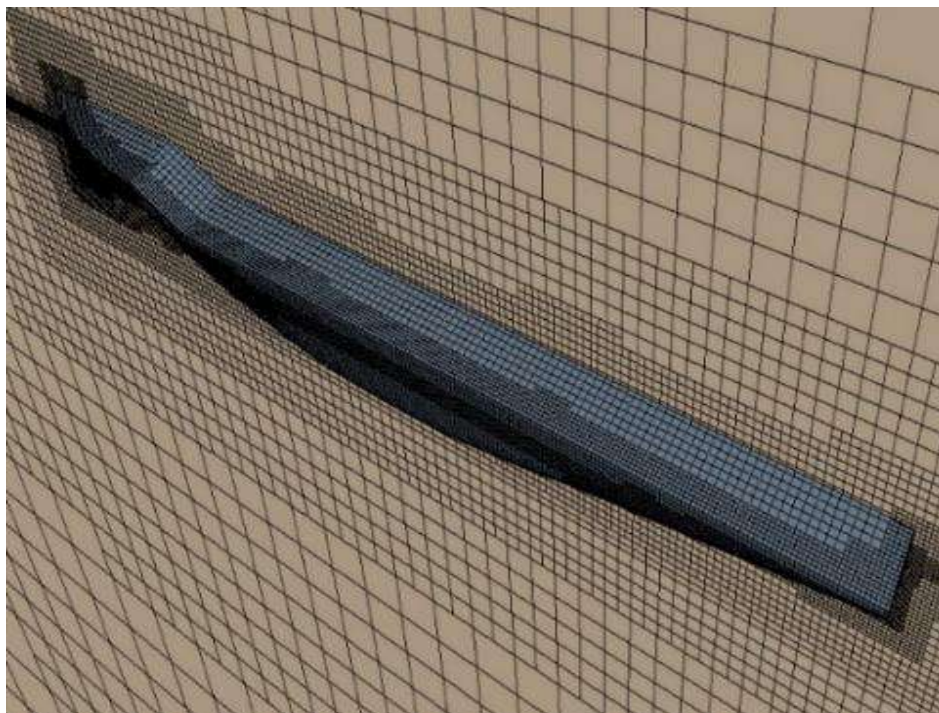
Fig. 4.4: Surface mesh of the KCS hull

4.3.2 Volume Mesh

The volume mesh in a simulation is the mathematical description of the space or geometry of the problem being solved. A Trimmed cell mesher and prism layer mesher models are used in this mesh generation strategy. Trimmed cell mesher provides a robust and efficient method of producing a high-quality grid for both simple and complex geometry problems. The trimmer meshing model utilizes a template mesh that is constructed from hexahedral cells from which it cuts or trims the core mesh using starting input surface. The template mesh contains refinement that is based on the local surface mesh size and local refinement controls. Finite volume mesh with hexahedral cell was generated within the whole domain as shown in Fig. 4.5.



(a) Computational Domain



(b) Closed view of hull surface

Fig. 4.5: Finite volume mesh applied to the domain and hull model

To capture the free surface efficiently a thin rectangular block is created with high mesh resolution at the free surface location which is shown in Fig. 4.6 and at the stern and bow sides block small volumetric blocks are created to get better mesh quality as presented in Fig. 4.7. Special care is also taken away from the stern of the hull to capture the free surface wave more accurately.

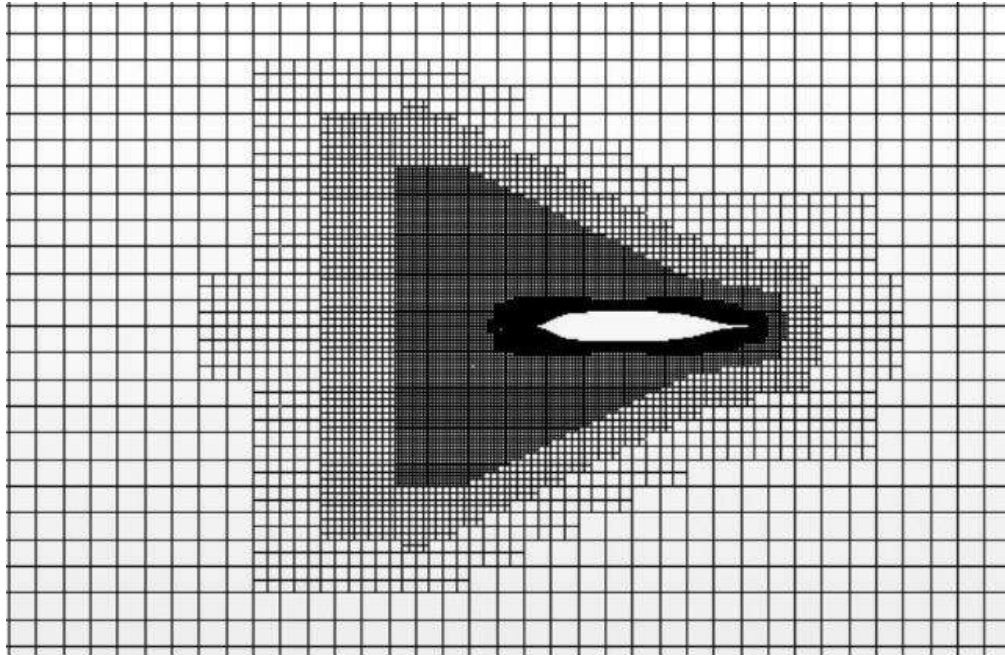
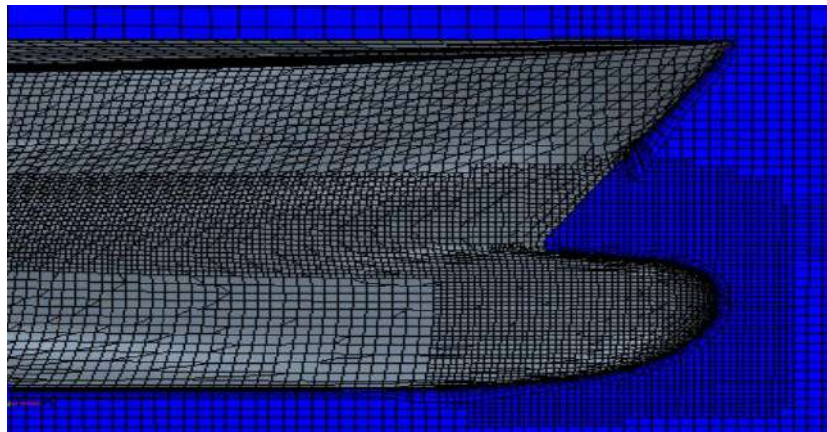
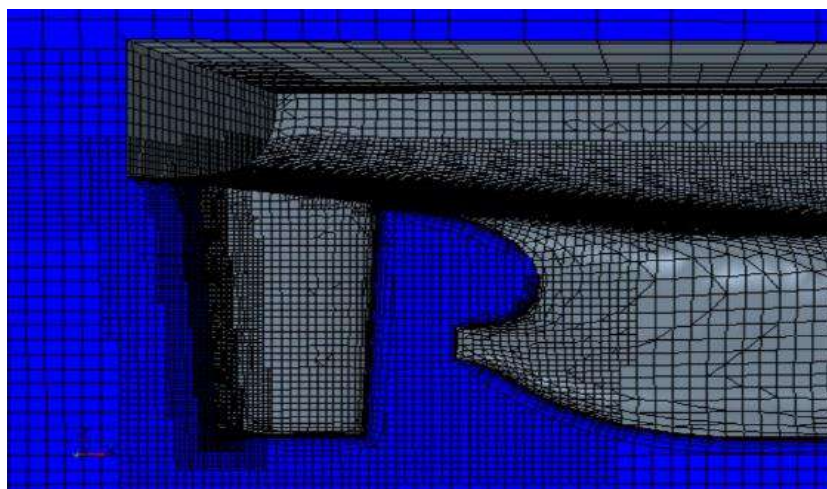


Fig. 4.6: Refined mesh scene at the free



(a) Bow region



(b) Stern region

Fig. 4.7: Mesh applied at the bow and stern regions

A trimmed cell mesher technique is used to produce hexahedral cell and prism layer mesher model is applied to resolve accurately the turbulent flow near the solid wall of the hulls. Determination of the velocity gradients normal to the wall boundary has a remarkable effect on the accurate prediction of the flow features. Hence, prism layer allows to resolve these gradients, moreover, prism layer thickness is a region which govern a lot of key characteristics to predict the different hydrodynamic behaviors. The first prism layer height normal to the solid wall is determined using $y^+=60$ and using the geometric progression relationship which uses a stretch factor (constant value, 1.3), the size of the progressive layers are calculated. It is recommended that the size of the last layer of the prism should be the closet size to the core mesh.

Table 4.1: Overall thickness of a prism layer for KCS

Layer No.	Layer Thickness	Overall Thickness
1	0.00240	0.00240
2	0.00312	0.00552
3	0.00405	0.00957
4	0.00527	0.01484
5	0.00685	0.02169
6	0.00891	0.03060

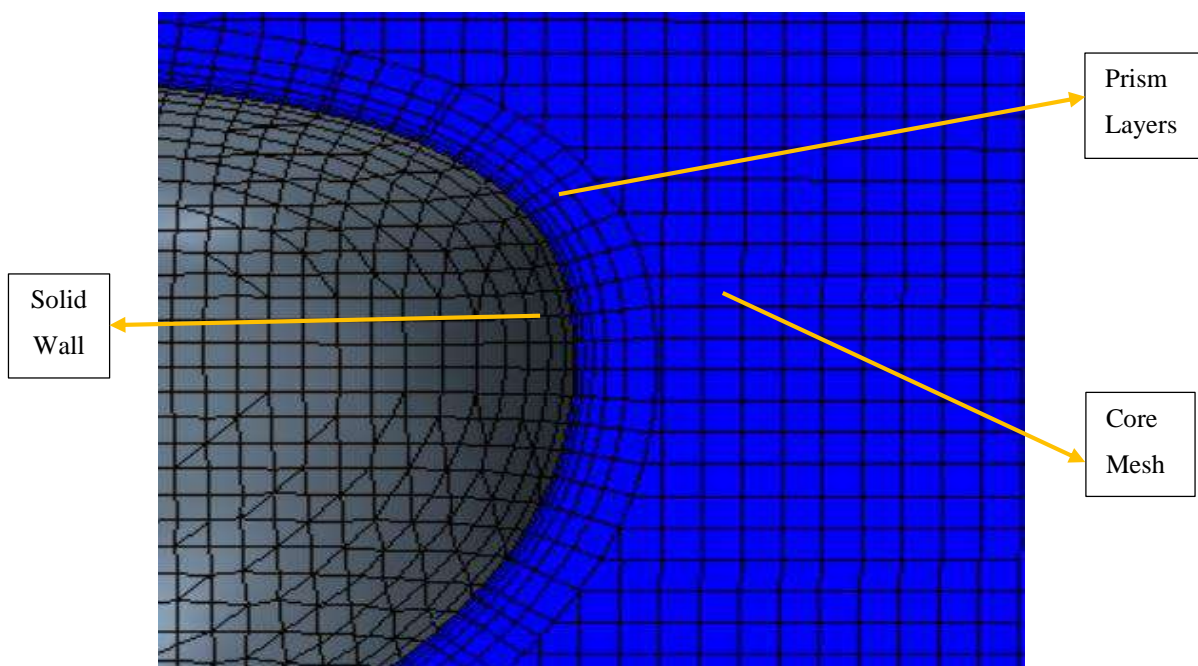


Fig. 4.8: Generated prism layers with the core mesh

4.4 Physics Modeling

After creating the computational domain and generating the mesh, next step is to set the proper physics model and fluid properties. Many industrial CFD flow problems may require solutions to very complex physical flow processes. STAR-CCM+ contains a wide range of physics models and methods for the simulation of single and multi-phase fluid flow, heat transfer, turbulence, solid stress, dynamic fluid body interaction, and related phenomenon.

Physics models define the primary variables of the simulation (such as pressure, temperature, and velocity) and what formulation is used to generate the solution. An appropriate combination of models is necessary for the complete definition of a physics continuum.

4.4.1 Space Modeling

The primary function of the space model in STAR-CCM+ is to provide methods for computing and assessing mesh matrices. The mesh matrices include cell volume and centroid, face area and centroid, cell and face indexes, and skewness angle. For space modeling, three-dimensional model is selected. The three-dimensional model is designed to work on three-dimensional meshes.

4.4.2 Time Modeling

Time model in STAR-CCM+ provides solvers that control the iteration and/or unsteady time-stepping. In RANS equation, there are time varying properties the problem becomes an unsteady state. The implicit unsteady is used due to unsteady model available with the segregated flow and segregated fluid energy model. In the implicit unsteady approach each physical time-step involves some number of inner iterations to converge the solution for that given instant of time. These inner iterations may be accomplished using the same implicit integration or explicit integration schemes used for steady analysis.

4.4.3 Materials Modeling

The material model is responsible for managing the material that is substance or substances, being simulated in the continuum. The simulated material is responsible for managing the various thermodynamic and transport properties relevant to that material and to the physical processes being modeled in the continuum. In the present study, the simulated body is exposed to two phases namely air and water. Hence, a multiphase mixture model is selected and this model is for simulating two or more immiscible phases, where each phase is composed of pure

gas or liquid substance, such as air and water. Materials properties for used two phases (fluid-fluid) are tabulated below:

Table 4.2: Material properties for multiphase modeling

Phase	Material	Density (kg / m^3)	Dynamic Viscosity ($Pa - s$)
Liquid	Water	1000	1.1375×10^{-3}
Gas	Air	1.225	1.802×10^{-5}

4.4.4 Multiphase Flow Modeling

Multiphase flow is term which refers to the flow and interaction of several phases within the same system where distinct interface exist between phases. Volume of Fluid (VOF) multiphase flow model which is provided for systems containing two or more immiscible fluid phases, where each phase constitutes a large structure within the system. This approach captures the movement of the interface between the fluid phases. In VOF homogenous multiphase model, a common velocity and pressure field are assumed for all phases.

An iso surface is created in this multiphase model which basically represents the free surface between the air and water phases. An iso value (volume fraction) 0.5 is selected such that the iso surface is created at the $z=0$ plane (draft line) as shown in Fig. 4.9.

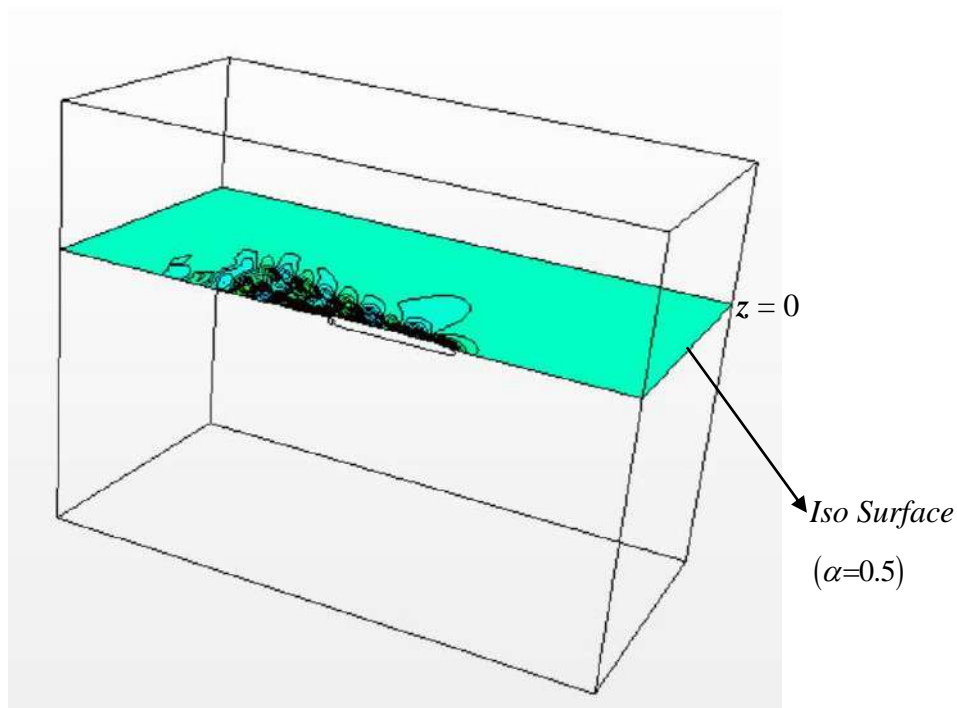


Fig. 4.9: Iso surface generated by multiphase modeling

Volume fraction is defined by,

$$\alpha = \frac{V_i}{V} \quad (4.8)$$

Sum of the volume fraction is unity:

$$\sum_i \alpha = 1 \quad (4.9)$$

Depend on the value of volume fraction, three conditions are possible:

1. $\alpha = 0$, The cell is empty of liquid
2. $\alpha=1$, The cell is completely full of liquid
3. $0<\alpha<1$, The cell contains a free surface

Fig. 4.10 indicates the initial stage of the simulation, where the value of volume fraction equal to 0.5 i.e. the control volume at the free surface contains 50% of water and 50% of air. The further away from the free surface, red zone is completely full of liquid ($\alpha \rightarrow 1$) and the blue zone is empty of liquid ($\alpha \rightarrow 0$).

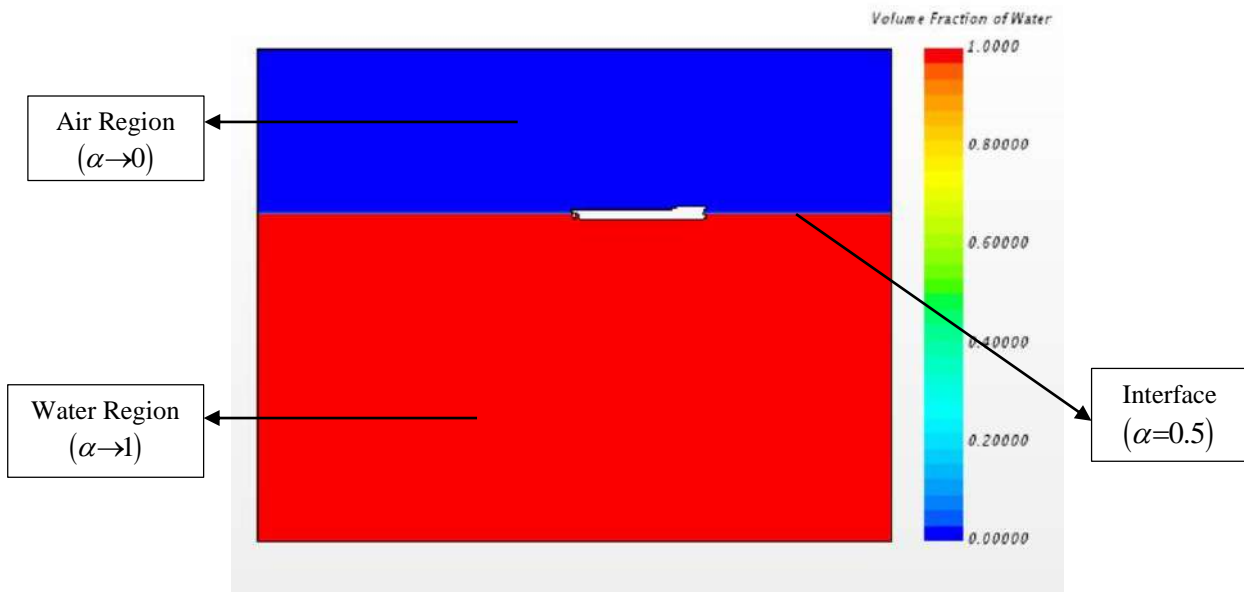


Fig. 4.10: Free surface at initialization stage of simulation.

4.4.5 VOF Waves

VOF wave is used to simulate surface gravity waves on a light fluid (air)-heavy fluid (water) interface. This is for three-dimensional cases only, and are used with the Volume of Fluid (VOF) multiphase model in STAR-CCM+. It is typically used with the 6-DOF Motion model for marine applications. When created, VOF Wave provides field functions that can be used to

initialize the VOF calculation and to provide suitable profiles at boundaries. The VOF Wave model, when selected, also activates a region condition and a boundary condition to control damping of the waves near boundaries in order to reduce wave reflections.

The simulation is carried out in calm water condition and hence selected Flat wave option available in STAR-CCM+. A flat wave represents a calm plane of water, that is, the least amount of current. In the flat wave properties, the point on the water level defines the position of the water surface that is the load water line. The vertical direction is given normal to the water surface. The current and wind velocity for the model is water (heavy fluid) and air (lighter fluid) respectively.

The VOF wave model also includes a VOF wave damping capability. This means that a VOF wave can be damped in the vicinity of selected boundaries to reduce wave oscillation near those boundaries. The VOF Wave damping option is activated at the outlet boundary of the computational domain.

4.4.6 Turbulence Modeling

The turbulence models in STAR-CCM+ [28] are responsible for providing closure of the governing equations in turbulent Flows. Three basic approaches to modeling turbulence are available in STAR-CCM+.

- Models that provide closure of the Reynolds-Averaged Navier-Stokes (RANS) equations.
- Large eddy simulation (LES).
- Detached eddy simulation (DES).

Present problem relies on the first approach. The second two approaches (LES and DES) are best used after carefully reviewing the applicable literature to gain confidence that the grid resolution requirements can be met and that the computational costs incurred by resolving the small time and length scales are indeed justified.

Eddy viscosity models

Eddy viscosity models use the concept of a turbulent viscosity μ_t to model the Reynolds stress tensor as a function of mean flow quantities. The most common model is known as the Boussinesq [27] approximation:

$$\mathbf{T}_t = 2\mu_t \mathbf{S} - \frac{2}{3}(\mu_t \nabla \cdot \mathbf{v} + \rho k) \mathbf{I} \quad (4.10)$$

Where \mathbf{S} is the strain tensor:

$$\mathbf{S} = \frac{1}{2}(\nabla \mathbf{v} + \nabla \mathbf{v}^T) \quad (4.11)$$

and k is the turbulent kinetic energy.

The eddy viscosity models in STAR-CCM+ solve additional transport equations for scalar quantities that enable the turbulent viscosity μ_t to be derived. These include the following turbulence models:

- Spalart-Allmaras models
- K-Epsilon models
- K-Omega models

Among these three models, the K-Epsilon models is selected because this model provides a good compromise between robustness, computational cost and accuracy. They are generally well suited to industrial-type application that contain complex recirculation, with or without heat transfer.

4.4.7 Wall Treatment Modeling

A wall treatment in STAR-CCM+ is the set of near-wall modeling assumptions for each turbulence modeling. STAR-CCM+ provides three types of wall treatment:

The high- y^+ wall treatment assumes that the near-wall cell lies within the logarithmic region of the boundary layer and uses a wall function. A wall function is the set of mathematical relations that are used to obtain the boundary conditions for the continuum equations. These calculations are based on the following assumptions:

- The turbulence model is valid only outside the viscous-dominated region of the boundary layer, and the viscous-affected region of the boundary layer is not resolved; and
- The centroid of the near-wall cell lies within the logarithmic region of the boundary layer.
- Velocity, turbulence, and other scalar quantities are distributed consistently

The main advantage of using wall functions is the significant savings in terms of near-wall mesh resolution.

The low- y^+ wall treatment is suitable only for low-Reynolds number turbulence models: this treatment assumes that the viscous sub-layer is properly resolved.

Low-Reynolds number turbulence models are valid throughout the boundary layer, including the viscous sub-layer. To resolve the viscous sub-layer, these models require a sufficiently fine mesh. There is little or no need for modeling to obtain the wall boundary conditions. The computational expense that is associated with this approach can be significant, particularly for large Reynolds numbers.

The all- y^+ wall treatment is a hybrid treatment that attempts to emulate the high- y^+ wall treatment for coarse meshes, and the low- y^+ wall treatment for fine meshes. It is also formulated with the desirable characteristic of producing reasonable answers for meshes of intermediate resolution.

Among the three treatments above, the high- y^+ wall treatment is applied because this treatment can have some computer storage by avoiding the computation of the wall distance when used certain high-Reynolds number models. Also this treatment is suitable for use with models that do not explicitly damp the turbulence model in the near –wall region.

Wall treatment formulation for K-Epsilon Model

To calculate the wall distance and reference velocity, following non-dimensional quantities are used:

$$y^+ = \frac{yu^*}{\nu} \quad (4.12)$$

$$u^+ = \frac{u}{u^*} \quad (4.13)$$

y is the normal distance from the wall to the wall-cell centroid.

u is the component of wall-cell velocity parallel to the wall.

u^* is a reference velocity.

For high- y^+ wall treatment, following terms are calculated as:

$$\text{Reference velocity, } u^* = \sqrt{C_\mu^{1/2} k} \quad (4.14)$$

$$\text{Wall-cell production, } G_k = \frac{1}{\mu} \left(\rho u^* \frac{u}{u^+} \right)^2 \frac{\partial u^+}{\partial y^+} \quad (4.15)$$

$$\text{Wall-cell dissipation, } \varepsilon = \frac{u^{*3}}{\kappa y} \quad (4.16)$$

κ is Von-Karman constant equal to 0.42

4.5 DFBI Modeling

Dynamic Fluid Body Interaction (DFBI) module simulate the motion of a rigid body in response to pressure and shear force the fluid exerts. STAR-CCM+ calculates the resultant force and moment acting on the body due to all influences, and solves the governing equations of rigid body motion to find the new position of the rigid body [28] . A rigid body (defined using a 6-DOF Body in STAR-CCM+) can be defined as an object in which the relative distance between internal points does not change. Using the standard Cartesian coordinate system as a reference frame, it is possible for a rigid body to move (translate) along each of the three axes, and to rotate about the axes.

This commercial code has the advantage to work with free motion enables to control which direction of motion will be calculated and which ones to be leave constraints. Present interests are to evaluate the sinkage (translation along the z axis) and trim (rotation about the y axis). Therefore Z motion and Y rotation are free to calculate and other four terms are kept as frozen.

The solution processes [47] for sinkage and trim can be summarized as follows:

- a) The flow around the ship hull with the fluid viscosity, flow turbulence and deformation of free surface taking into consideration is computed by the RANSE solver in the usual way (ship-fixed).
- b) The normal and shear stresses are integrated over the body surface to obtain the forces and moments acting on the body and then the amounts of sinkage and trim needed to balance the fluid dynamic forces and moment are evaluated.
- c) The grids of ship are rearranged to take the sinkage and trim into account, and the fluid flow is computed again.

4.6 Solver Setting

In the implicit unsteady solver the physical time step is selected following the ITTC guideline which gives the mathematical formulation given below:

$$\Delta t = 0.005 \sim 0.01L/U \quad (4.17)$$

Where Δt is the time step, L is the length between perpendicular and U is flow velocity.

For 6 (Six) DOF solver, the maximum number of iteration is chosen as 5 iteration to compute fluid forces, moments, and gravitational forces on a 6-DOF body and moves the vertices of the grid according to motion of the body.

In the stopping criteria, the maximum inner iteration is selected for every 10 iterations to get the required solution after every time step. The maximum number of iteration is continued until the residuals convergence.

Chapter 5

Results and Discussions

Simulations are carried out for four types of mono hull: Wigley hull, Kriso Container Ship (KCS) hull, Series 60 hull, and HSVA tanker and for one multihulls: Wigley catamaran hull. Simulation results constitute of total resistance coefficient, wave pattern and profile, sinkge, and trim are discussed in this chapter.

5.1 Wigley Hull

The Wigley hull is most commonly used for ship like form. It is a mathematically defined parabolic hull and the underwater hull is described by the equation,

$$y = \frac{B}{2} \left(1 - \frac{z^2}{H^2} \right) \left(1 - \frac{4x^2}{L^2} \right) \quad (5.1)$$

The x-axis shows forward, y to starboard and z downward. The main particulars of the mathematically defined Wigley hull are provided in the Table 5.1.

Table 5.1: Main Particulars of Wigley Hull

Particulars	Value
Length (m)	L (m) 3.0
Breadth (m)	B (m) 0.3
Draft (m)	H (m) 0.1875
Block coefficient	C_b 0.444
Mid-ship coefficient	C_x 0.667
Wetted surface area coefficient	C_s 0.661
Vertical center of gravity	KG (m) 0.17
	K_{xx} / B 0.30
Moment of inertia	K_{yy} / L 0.25
	K_{zz} / L 0.25

The dimensions of the half of the computational domain (Fig. 5.1) is taken as of 12m long, 6m wide, and 3.5 m deep with the total no of cells of **2579745** for the finest grid. The grid is refined

by creating additional rectangular block at the free surface indicated by the dark region in order to get better resolution of the free surface and this is so done following the ITTC recommendation that a minimum of 80 cell numbers per wave length and a maximum of 20 cell numbers per wave height should be kept at the free surface. The mesh resolution also refined around the hull with high density of mesh. Two more mesh resolutions such as medium (**1249498** cells) and coarse (**599208** cells) are employed in the simulation to carry out the convergence study. The mesh structures of the computational domain and the hull are shown in Fig. 5.2 and Fig. 5.3 respectively. The resulting mesh is composed principally hexahedral cells with trimmed cells next to the surface. The prism boundary layer is applied around the ship hull to capture the flow properties with accuracy.

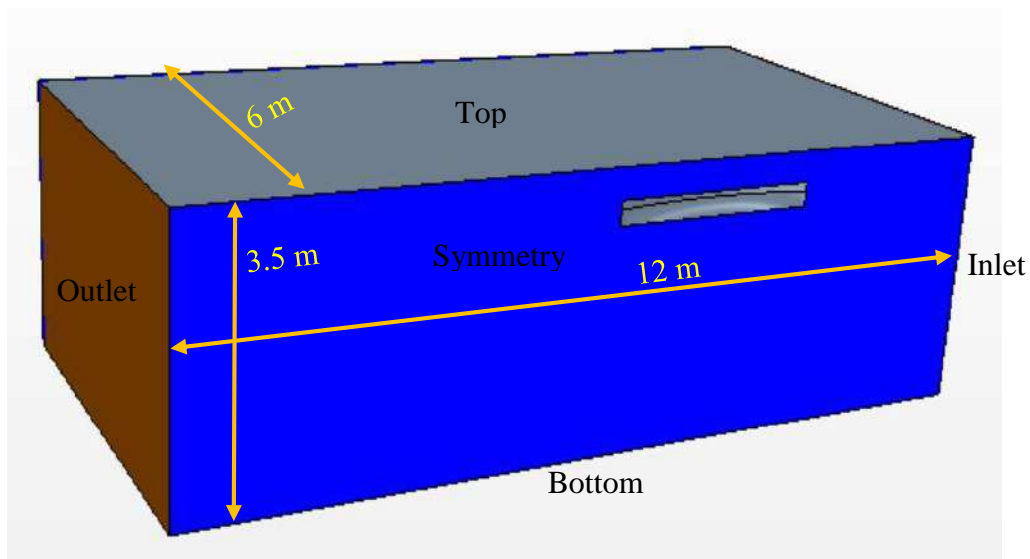


Fig. 5.1: Computational Domain of Wigley Hull

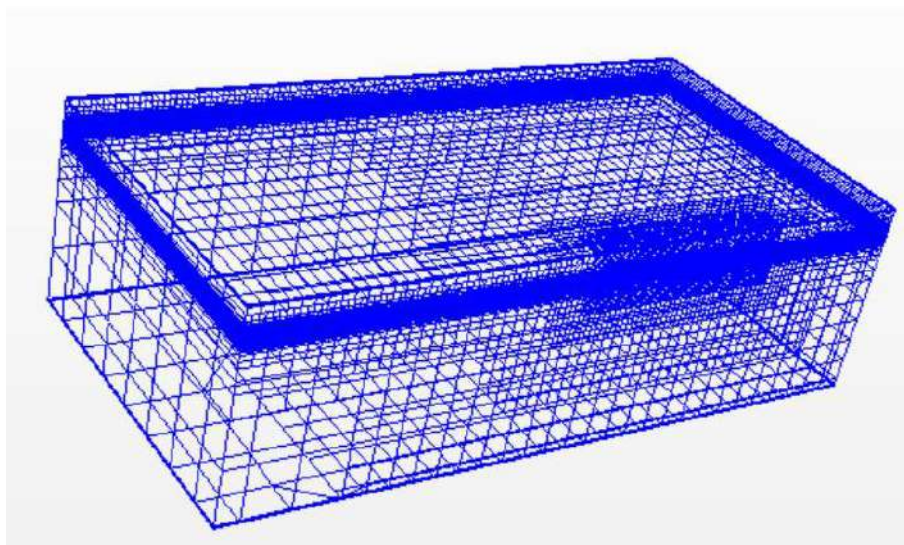


Fig. 5.2: Mesh structure for flow computation domain

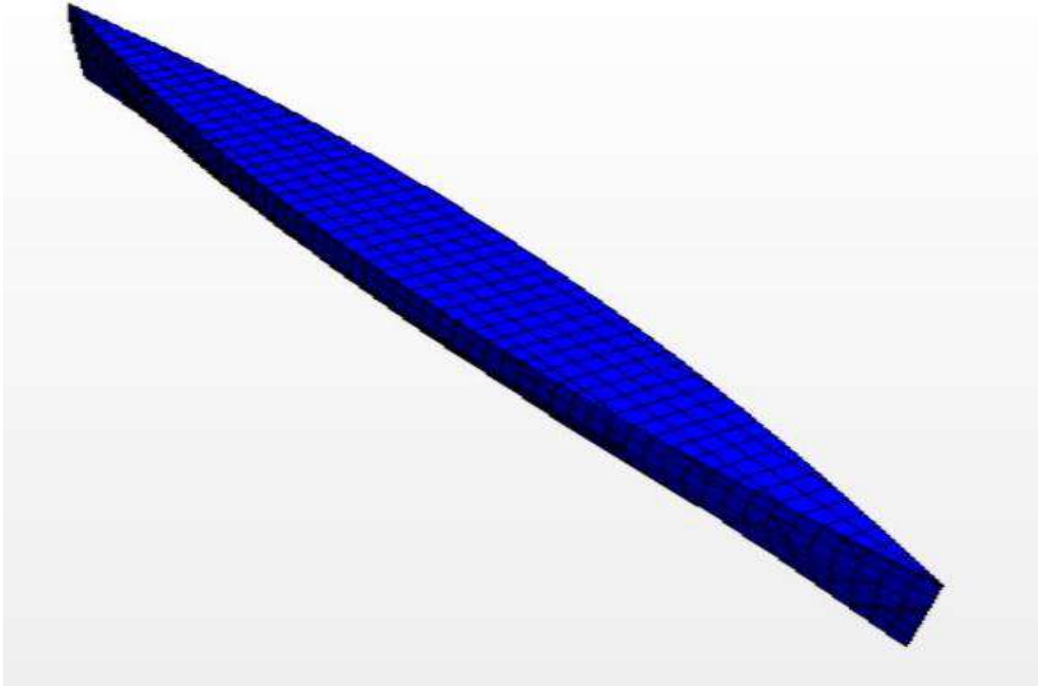


Fig. 5.3: Grid distribution on the surface of Wigley hull

Total Resistance Coefficient

The Wigley model is simulated for a wide range of Froude numbers, obtained results of total resistance coefficient is shown in Fig. 5.4 with the experimental data [48] and also with the results performed by Barros [49]. The total hull resistance increases as the speed (Froude No) increases as shown in Fig. 5.3. At the lower Froude no, the frictional resistance dominants and at the higher Froude no, $F_n \geq 0.40$ the resistance curve increases rapidly as the wave resistance dominates. The curve of the total resistance followed a number of “hump” and “hollow” in the curve. The interference effect between the bow and stern transverse wave systems (discussed in section 2.6) is the reason for the hump and hollow condition in the resistance curve. First hollow occurred at Fn range 0.25-0.28 and 2nd occurred at Fn range 0.34-0.36 and then followed by significant hump at the peak at Fn about 0.47. Above the Froude number 0.47, the interference transverse bow and stern become less significant while the divergent waves become more and more important. As the ship moves, the energy given to the water by bow is carried out laterally and away from the ship and hence the height of each succeeding wave of each system decreases with no considerable change in wavelength results in a decrease in wave resistance [33].

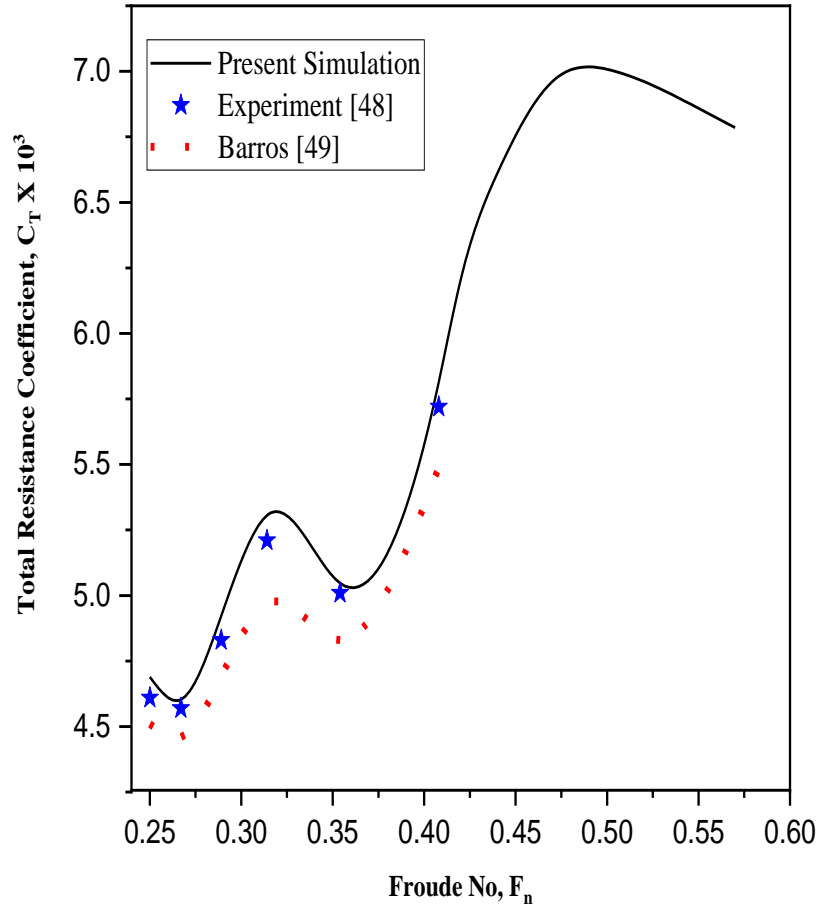


Fig. 5.4: Comparison of total resistance coefficient for Wigley hull.

Moreover, with the increasing Froude number, the wetted surface area decreases gives a less value in frictional resistance. So, the effect of decreasing value in frictional and wave resistance follows a downward trends in resistance curve after the significant resistance value as shown in Fig. 5.4. Overall, the resistance coefficient consistency shown in Fig. 5.4 is found in good agreement with of those available experimental results and Barros [49] as well.

The summary of resistance coefficient results with error calculation is given in Table 5.2. The relative error is found using this formula:

$$|Error| = \left| \frac{S - D}{D} \right| \times 100 \quad (5.2)$$

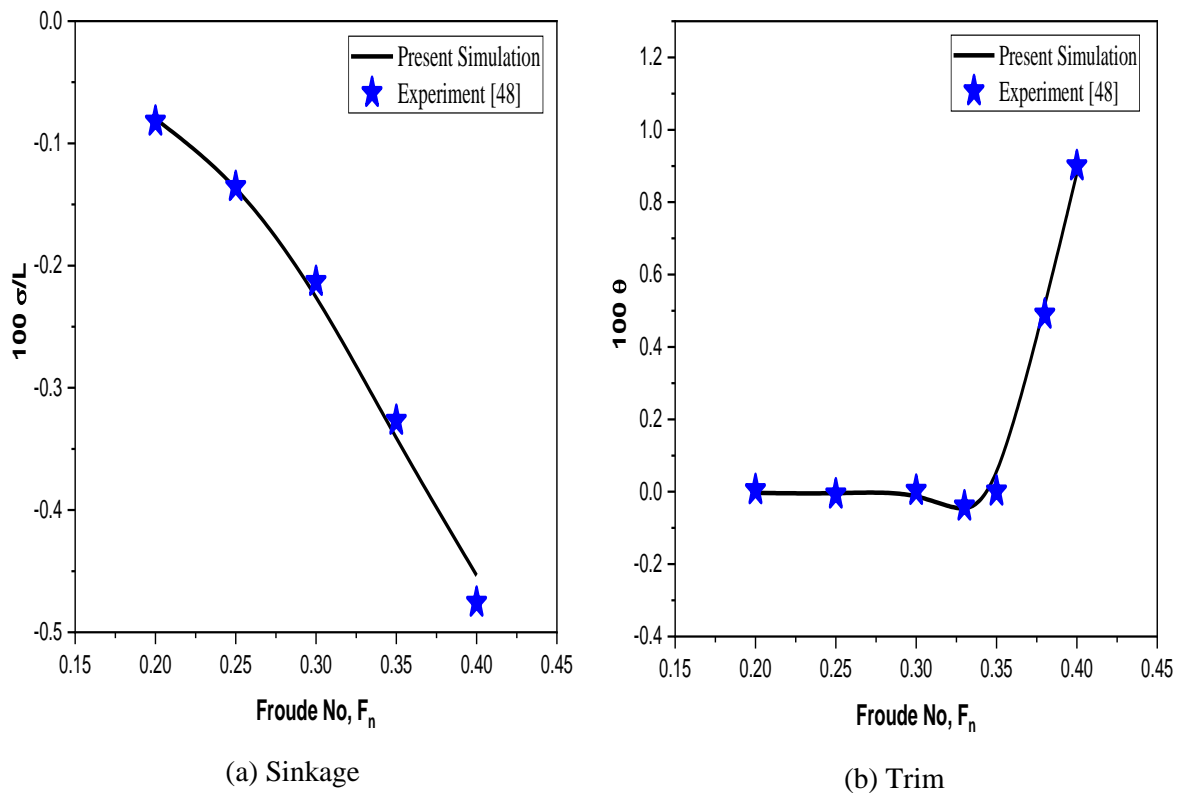
S is stand for the simulated computational fluid dynamics (CFD) results and D stands for the experimental fluid dynamics (EFD) results. The relative errors found by Barros [49] carried out the simulation in OpenFOAM solver are slightly larger than the relative error found by the present simulation carried out in STAR-CCM+ solver.

Table 5.2: Relative error analysis of resistance coefficient for Wigley hull

Froude No	Speed, U (m/s)	Reynolds No, Rn	$C_T \times 10^3$ EFD (D)	$C_T \times 10^3$ CFD (S)	Error	$C_T \times 10^3$ [49] (S)	Error
0.25	1.356	3.6×10^6	4.61	4.689	1.714 %	4.51	2.169 %
0.267	1.448	3.8×10^6	4.57	4.602	0.700 %	4.46	2.407 %
0.289	1.567	4.1×10^6	4.83	4.921	1.884 %	4.69	2.898 %
0.316	1.714	4.5×10^6	5.21	5.315	2.015 %	4.97	4.606 %
0.354	1.920	5.1×10^6	5.01	5.047	0.738 %	4.83	3.593 %
0.408	2.213	5.8×10^6	5.72	5.814	1.643 %	5.49	4.021 %

Sinkage and Trim

Figure 5.5 shows the comparison of sinkage and trim with the experimental values and indicates a good agreement between those two values. The sinkage values are normalized by $L/100$ and due to very small value of trim angle, values are multiplied by 100. A negative value of sinkage indicates the downward direction and positive value of trim indicates the bow up.

**Fig. 5.5:** Comparison of sinkage and trim for Wigley hull

Pressure Field

The pressure distribution over the hull surface is shown in Fig. 5.6 for different Froude numbers. Pressure is normalized by the $\frac{1}{2}\rho U^2$ term, where ρ is the fluid density and U is the free stream velocity. High pressure gradient is expected at the region where the flow interacts with the rapid changing geometry: the bow and stern regions are such geometries. From the figure it has been shown that the forward and aft portion of the ship experience larger pressure than any other location. The forward of the hull is positioned at the right side in the Fig. 5.6.

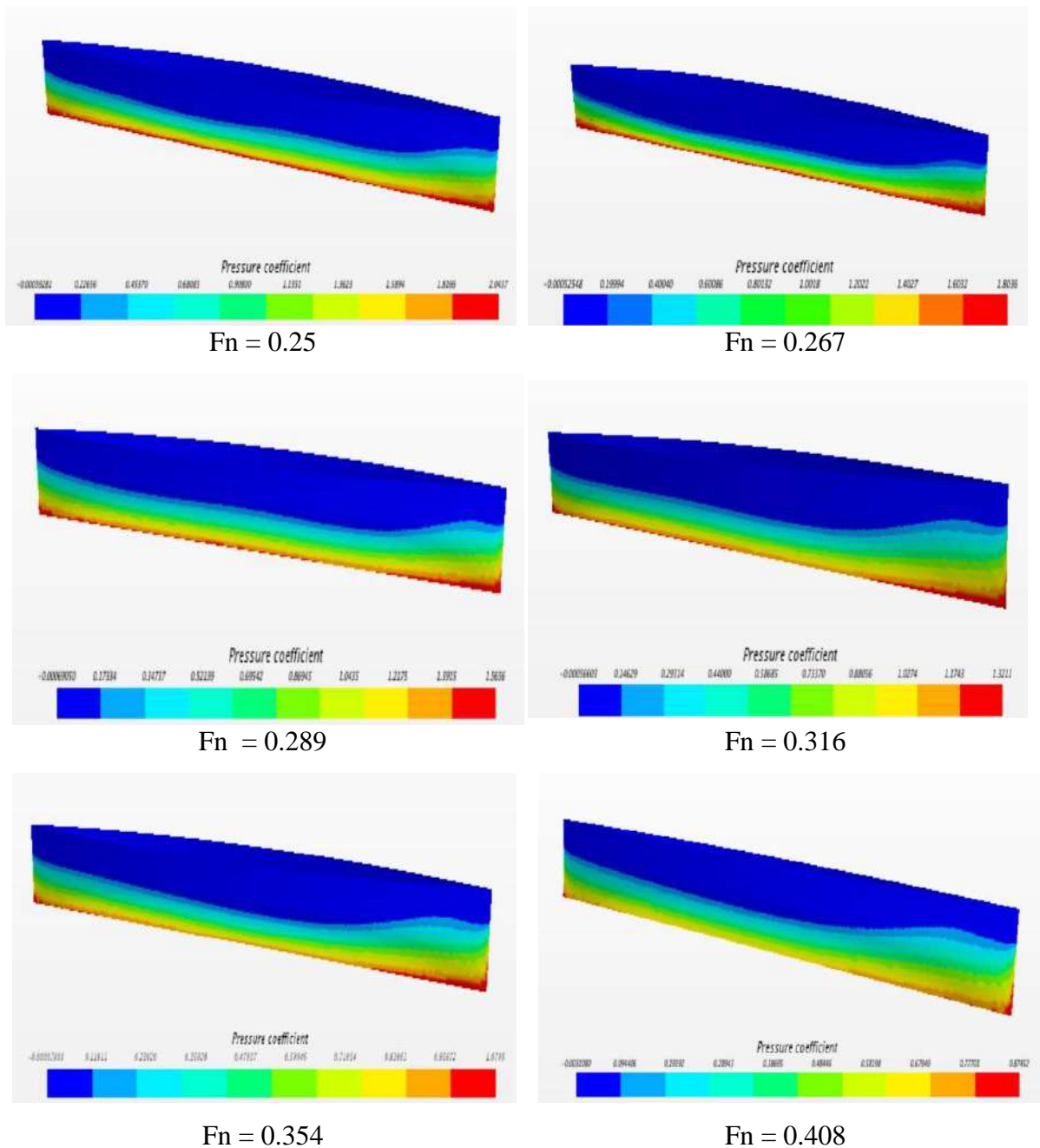


Fig. 5.6: Pressure distribution over the surface of Wigley hull

Wave Profile and wave pattern

The computed wave profiles along the Wigley hull are presented in the Fig. 5.7 and compared with the experimental data [48]. Both axes: position and wave height is normalized by the length of the hull. The computed wave profiles with the present methodology are well compatible with the experimental results at the almost every location along the hull.

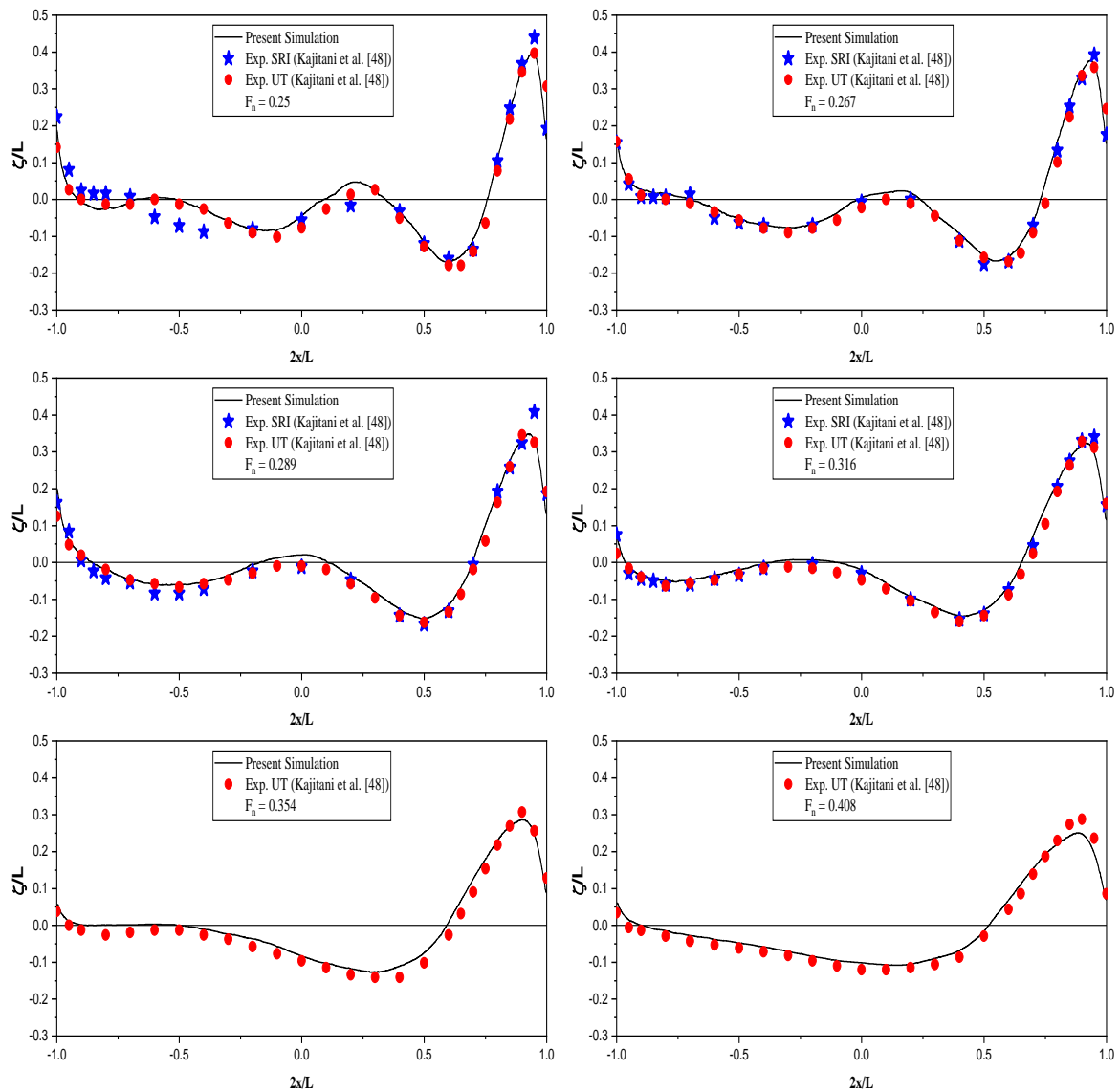


Fig. 5.7: Wave profile along the Wigley mono hull with experimental results.

At near of the bow of the hull, the wave elevation has its highest value near the bow of the hull and immediately behind the hull as expected. At the lower Froude number, there are number of crest in the wave profile while it decreases at the higher Froude number as shown in Fig. 5.7. The pressure increases where wave crests are found and pressure decreases in the trough

of the wave profile. For the Wigley hull, the breadth to length (B/L) ratio is 0.1 which is much less than the practical hull form and therefore the predicted wave profile is in well agreement both in height and profile with the experimental one. It has also been concluded that the wavelength is increased with the increased value of Froude number i.e. increment of reference speed which is the indication of increase of wave resistance.

The computed wave contour for the same Froude numbers mentioned above are presented in the Fig. 5.8. The ship hull is fixed relative to incoming water flow (water flows in the negative x direction i.e. bow to stern direction) and the water creates both diverging waves spread outward from the hull and transverse wave following behind the stern of the ship hull. The consisting wave pattern is known as the Kelvin wave pattern.

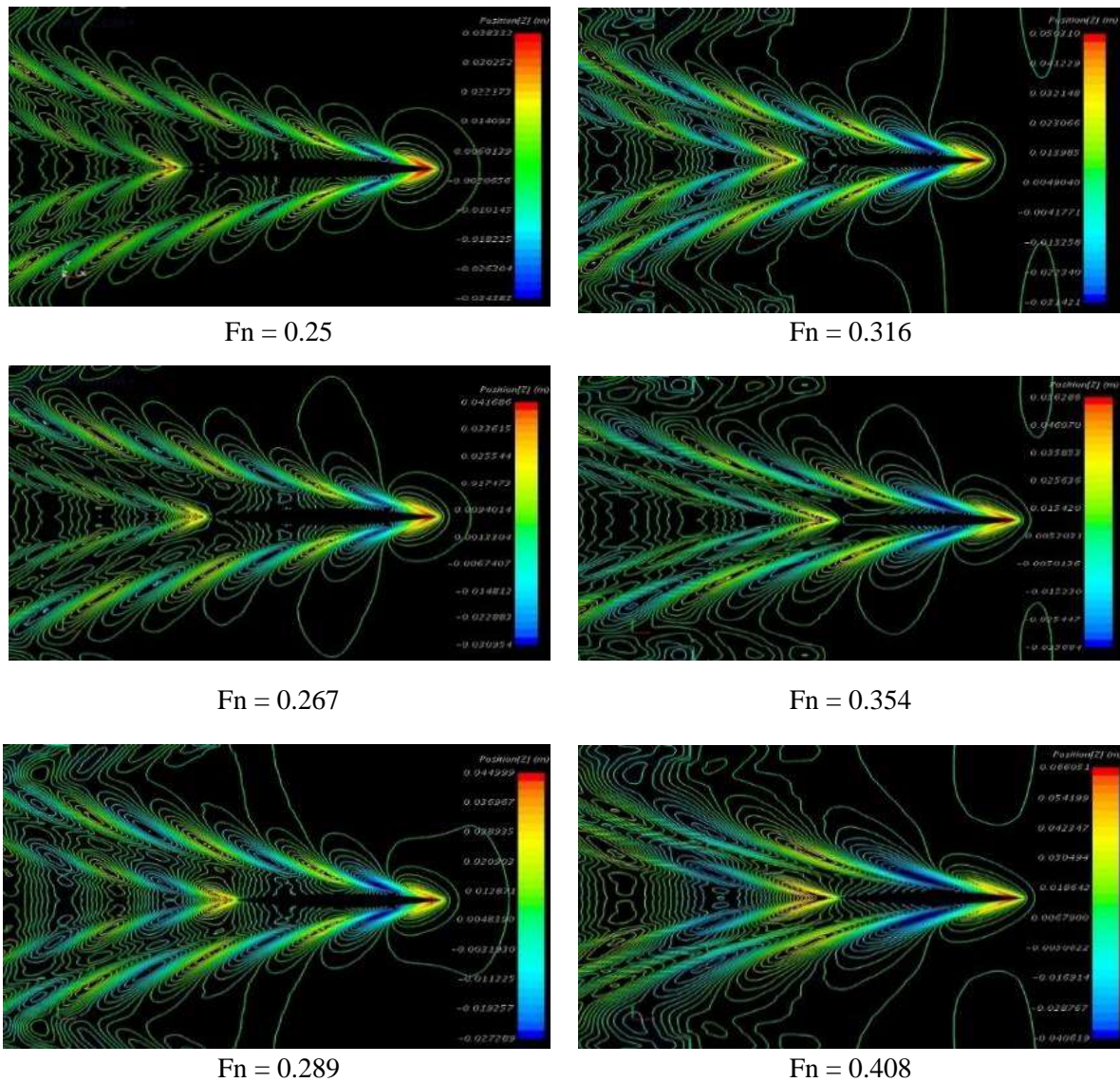


Fig. 5.8: Kelvin Wave pattern at different Froude numbers for Wigley hull

From the wave pattern it can also be seen that with the increasing Froude number, the wave height (Position [Z]) marked by the red color (at the bow location) is increasing. A comparison have also been made in Fig. 5.9 with the published numerical results (Tarafter and Khalil [50]) carried out by a boundary element method (BEM) for solving a non-linear free surface problem. The qualitative comparison is found for the wave pattern at the Froude numbers 0.289 and 0.316 and hence it can be stated that the present finite volume method (FVM) gives a reasonable simulation of wave field.

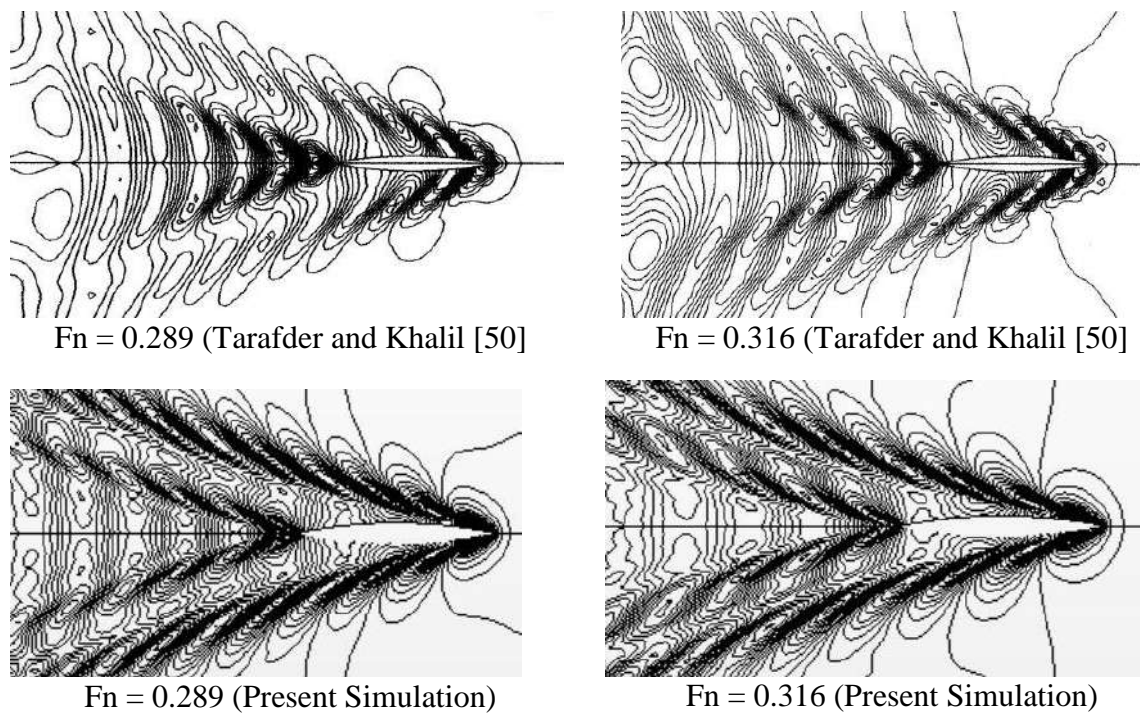


Fig. 5.9: Kelvin Wave pattern comparison for Wigley

Grid Dependence Test

In finite volume method, the partial differential equations are solved numerically for RANS equations and hence the discretization errors are introduced. Theoretically it is said that to minimize that errors, the number of cells by discretization are increased. However, in numerical analysis to study the errors and uncertainties, grid independence study must be done. In this case, three simulations were performed by keeping all the parameters same except the grid refinement. A systematic grid refinement ratio, $r = \sqrt{2}$ was applied to the three directions in the computational domain. The grid properties with the cell no and the grid solutions are shown in Table 5.3.

Table 5.3: Grid properties for C_T , C_F , and C_W

Grid No	Cell No	$r = h_i/h_1$	$C_T \times 10^3$	$C_F \times 10^3$	$C_W \times 10^3$
Grid 1 (Fine)	2579745	1.000	4.583	3.569	1.013
Grid 2 (Medium)	1249498	1.414	4.602	3.592	1.010
Grid 3 (Coarse)	599208	2.000	4.753	3.756	0.998

The simulated results for Wigley hull at the three grids are given in Table 5.4 with the relative solution changes (ε), relative error ($E\%D$) and EFD (D) value is also given for the comparison.

Table 5.4: Grid convergence study of C_T , C_F , and C_W for Wigley hull

Grid	S_1 (Grid 1)	S_2 (Grid 2)	S_3 (Grid 3)	EFD Data
$C_T \times 10^3$	4.583	4.602	4.753	4.57
$E\%D$	-0.28	-0.70	-4.00	
$\varepsilon\%$	-0.40	-3.28	---	
$C_F \times 10^3$	3.569	3.592	3.756	3.55
$E\%D$	-0.53	-1.18	-5.80	
$\varepsilon\%$	-0.64	-4.56	---	
$C_W \times 10^3$	1.013	1.010	0.998	1.02
$E\%D$	0.68	0.98	2.15	
$\varepsilon\%$	0.29	1.18	---	

From Table 5.4 it has been shown that the relative errors are in acceptable range. Especially for the finest grid solution: 0.28%, 0.53%, and 0.68% for the total, frictional and wave resistance coefficients which are very low. Also, the relative solution change between Grid 1 and Grid 2 is less than change between Grid 2 and Grid 3 that indicates the state of convergence.

Solution changes between medium-fine and coarse-medium can be written as

$$\varepsilon_{21} = S_2 - S_1 \quad (5.3)$$

$$\varepsilon_{32} = S_3 - S_2 \quad (5.4)$$

S_1 , S_2 , and S_3 are the solutions of fine, medium, and coarse mesh refinement. Convergence ratio defined as

$$\text{Convergence ratio, } R_G = \frac{\varepsilon_{21}}{\varepsilon_{32}} = \frac{S_2 - S_1}{S_3 - S_2} \quad (5.5)$$

Three convergence conditions are possible:

- i. Monotonic convergence: $0 < R_G < 1$
- ii. Oscillatory convergence: $R_G < 0$
- iii. Divergence: $R_G > 1$

As the calculation procedure for all the solution parameters is same, only the calculation of total resistance coefficient (C_T) is presented here. The convergence ratio:

$$R_G = \frac{\varepsilon_{21}}{\varepsilon_{32}} = \frac{S_2 - S_1}{S_3 - S_2} = \frac{(4.602 - 4.583) \times 10^{-3}}{(4.753 - 4.602) \times 10^{-3}} = 0.12$$

The value of convergence ratio, R_G indicates that this the monotonic convergence condition i.e. the simulated result has been converged. And, also the simulated result is independent of the grid refinement. For monotonic convergence, generalized Richardson Extrapolation (RE) [40] is used to evaluate the numerical uncertainties which has been discussed in Chapter 3.

The 1st order RE estimate δ_{RE} , the order of accuracy p_G , and correction factor C_G are given as follows:

$$p_G = \frac{\ln(\varepsilon_{32}/\varepsilon_{21})}{\ln(r)} = \frac{\ln(0.151/0.019)}{\ln(\sqrt{2})} = 5.98$$

$$\delta_{RE} = \frac{\varepsilon_{21}}{r^{p_G} - 1} = 2.74 \times 10^{-6}$$

$$C_G = \frac{r^{p_G} - 1}{r^{p_{east}} - 1} = 6.95$$

For C_G sufficiently less than or greater than 1 (one) and lacking confidence, the grid uncertainty U_G is determined as follows:

$$\begin{aligned} U_G &= |C_G \delta_{RE}| + |(1 - C_G) \delta_{RE}| \\ &= (19.04 \times 10^{-6}) + (16.3 \times 10^{-6}) \\ &= 35.34 \times 10^{-6} = 0.77\% S_1 \end{aligned}$$

The numerical uncertainty is found by, $U_{SN} = \sqrt{U_G^2 + U_I^2}$

Where U_I is the iterative uncertainty and assumed to be negligible in comparison to the grid uncertainty ($U_I \ll U_G$) such that $U_{SN} = U_G$

The convergence ratio R_G , order of accuracy p_G , correction factor C_G , and the numerical uncertainty U_{SN} for all the resistance coefficients following the above procedure are given in Table 5.5.

Table 5.5: Verification of C_T , C_F , and C_W for Wigley hull

Study	R_G	p_G	C_G	U_{SN}
C_T	0.12	5.98	6.95	0.77 % S_1
C_F	0.14	5.66	6.13	1.18 % S_1
C_W	0.25	4.00	3.00	0.50 % S_1

From Table 5.5 it has been shown that grid convergence ratio R_G for every resistance coefficient falls between 0 to 1, which is the indication of monotonic convergence [43], i.e., results are grid independent. For total resistance and frictional resistance coefficients, the order of accuracy p_G was found of larger value which in result lead to get higher numerical uncertainties. However, in case of wave resistance coefficient, C_W the numerical uncertainty was found lower than the other two values. All the uncertainties values are indicated as the percentage of the finest grid solution S_1 .

Validation

For the validation purpose, the finest grid solution S_1 is used to compare with the experimental data. The comparison error can be calculated as:

$$\begin{aligned}
 E &= S_1 - D \\
 &= 4.583 \times 10^{-3} - 4.57 \times 10^{-3} \\
 &= 0.013 \times 10^{-3} = 0.28\% D
 \end{aligned}$$

The symbol D is denoted for the experimental fluid dynamics (EFD) data. The validation uncertainty is calculated from

$$U_V = \sqrt{U_{SN}^2 + U_D^2}$$

U_D is the data uncertainty equal to 2.5% D [33].

$$\begin{aligned}
 U_V &= \sqrt{(0.773\% D)^2 + (2.5\% D)^2} \\
 &= 2.62\% D
 \end{aligned}$$

The absolute value of comparison error is calculated as

$$|E|\%D = \left| \frac{S_1 - D}{D} \right| \times 100$$

The comparison error E , validation uncertainty U_V , experimental data uncertainty U_D for all solution parameters are tabulated in Table 5.5. All the calculated values are shown as percentage of the EFD (D) value. S_1 is the simulation result for finest grid.

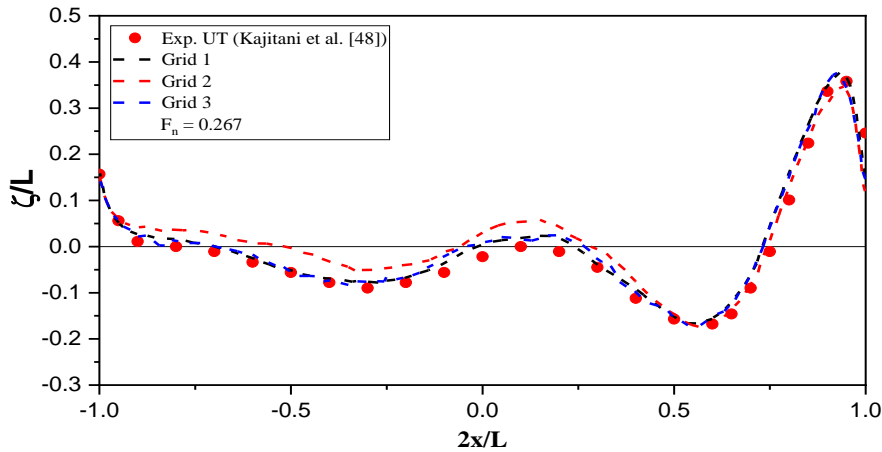
Table 5.6: Validation of C_T , C_F , and C_W for Wigley hull

Study	$ E \%$	$U_V\%$	$U_D\%$
C_T	0.28 %D	2.62 %D	2.5 %D
C_F	0.53 %D	2.77 %D	2.5 %D
C_W	0.68 %D	2.55 %D	2.5% D

From Table 5.6 it has been observed that the relative errors for three cases are less than the validation uncertainties. According to Wilson [44], this condition ($|E| < U_V$) implies that the results are well validated. For three cases the validation uncertainties are generated with reasonable lower value. However, among them for the frictional resistance coefficient, the validation uncertainty shows a little bit higher value than the total and pressure resistance coefficient. Overall it is concluded that numerical results are nicely validated with the experimental results.

Grid Dependence and Validation of a point variable: Wave elevation, ζ

Wave profile along the hull for three grids: coarse, medium, and fine are shown in the Fig. 5.10. Experimental data [48] of wave profile is also shown for the comparison. Normalized value of maximum wave height is used for the verification and validation study

**Fig. 5.10: Grid dependency on wave profile of Wigley hull**

In the above figure, the wave heights are at different location along the hull surface at the free surface are normalized by the length of the hull. The overall pattern of wave profile for three grid sizes with the experimental data have satisfactory pattern. The numerical results of maximum normalized wave height, ζ_{\max} for Wigley hull at the three grids are given in Table 5.7 with the relative change, ε and EFD value is also given for the comparison. The convergence ratio R_G , order of accuracy p_G , correction factor C_G , and the numerical uncertainty U_{SN} are given in Table 5.8.

Table 5.7: Grid convergence study of wave profile for Wigley hull

Grid/Study	S_1 (Grid 1)	S_2 (Grid 2)	S_3 (Grid 2)	EFD (D) Data
ζ_{\max}	0.3767	0.3764	0.3505	0.3580
ε		-0.08 %	-6.8 %	

Table 5.8: Verification and validation of wave profile for Wigley hull

Study	R_G	p_G	U_{SN}	$ E \%$	$U_V\%$	$U_D\%$
ζ_{\max}	0.012	12.86	0.16 % S_3	2.09 %D	2.51 %D	2.5 %D

From Table 5.8, the order of accuracy was found with very high value from the typical theoretical order of accuracy. This is because of the changes of solutions of the point variable tends to value of zero. The validation was done with the solution of Grid 3 and it was found that the relative error is less than the validation uncertainty, i.e., the wave profile is validated against the experimental data.

5.2 KCS Hull

KRISO container ship (KCS) is usually chosen as a benchmark for flow computations. Principal particulars of the model ship and full scale are tabulated below in Table 5.9.

Table 5.9: Main particulars of KCS hull form

Principal particulars		Full Scale	Model
Length between perpendiculars	$L_{PP}(m)$	230.0	7.2786
Length of waterline	$L_{WL}(m)$	232.5	7.3577
Maximum beam of waterline	$B_{WL}(m)$	32.2	1.0190
Depth	$D(m)$	19.0	0.6013
Draft	$T(m)$	10.8	0.3418
Displacement volume	$\nabla(m^3)$	52030	1.6490
Wetted surface area	$S_w(m^2)$	9424	9.4379
Block coefficient	$C_B = \nabla / (L_{PP} \cdot B_{WL} \cdot T)$	0.6505	0.6505
	K_{XX}/B	0.40	0.4
Moment of inertia	K_{YY}/L_{PP}	0.25	0.25
	K_{ZZ}/L_{PP}	0.25	0.25

The origin of the coordinate system is located in an undisturbed free surface at midship so that the undisturbed incident flow appears to be a streaming flow in the positive direction. The z axis is vertically upward and the y axis extends to portside. The size of one-half of the computational domain (Fig. 5.11) is $-2.97 L < x < 1.97 L$, $0 < y < 2.47 L$, $-1.0 L < z < 0.17 L$ and is taken into account due to vertical plane symmetry that leads to reduce the number of element and to require less time to converge the problem. The KCS hull is firstly analyzed at the fixed condition to get the calm water resistance and then allowed to rotate about y-axis to calculate sinkage and trim. The mesh discretized view of computational domain and the hull are shown in Fig. 5.12 and Fig. 5.13. Three different mesh distributions are applied which are categorized as fine (**1057126** cells), medium (**531014** cells), and coarse (**303224** cells) mesh.

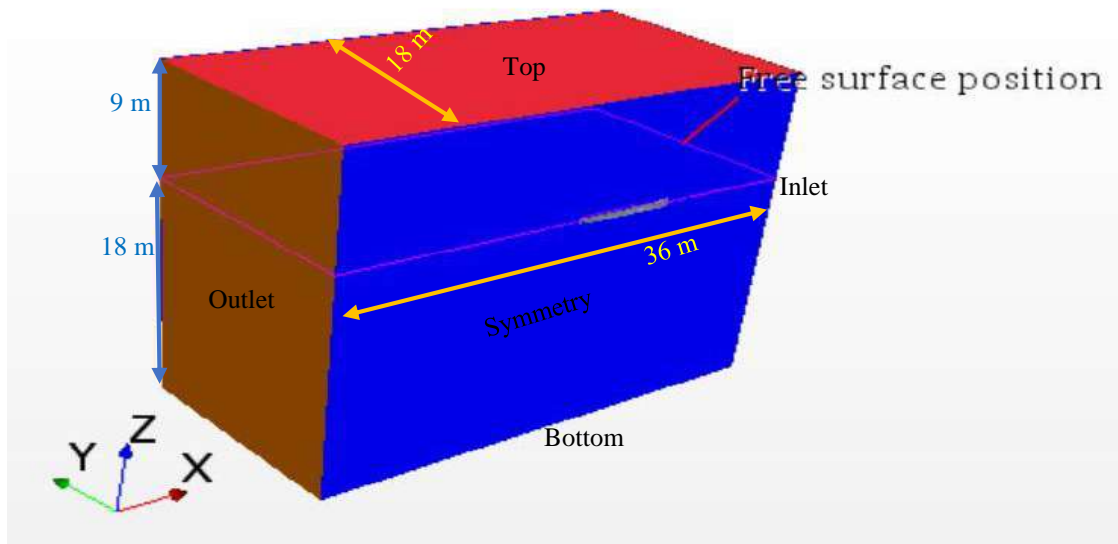


Fig. 5.11: Computational Domain of KCS hull

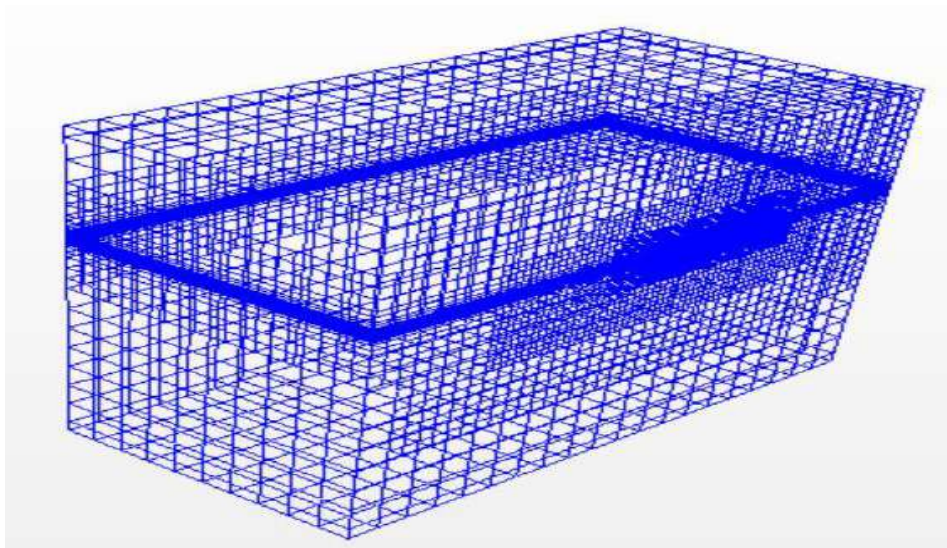


Fig. 5.12: Mesh structure of flow computation domain

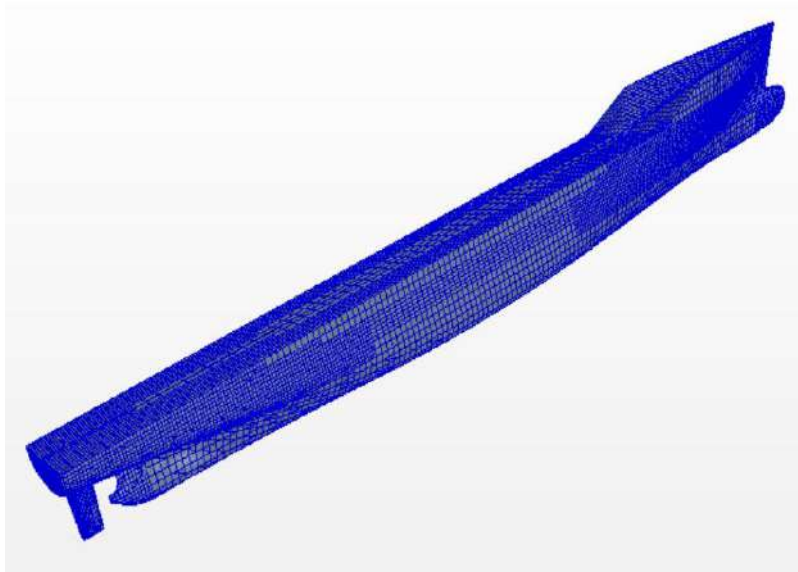


Fig. 5.13: Grid Distribution on the KCS hull

Resistance Coefficient

Total resistance coefficient (C_T) is calculated using the equation 2.79, where the total resistance (R_T) is obtained by averaging the resistance values over a certain period of physical time starting from the convergence state of the performed simulation. Such convergence history of resistances are shown in *Appendix D*. At the $Fn = 0.26$, the simulation runs almost for 64 sec and the convergence state (the solution reached at the steady state) of the result is found approximately at 30 sec and therefore the resistance value is extracted by averaging the values from 30 sec to 64 sec as shown in Fig. 5.14. It is observed that at the very beginning of time, the fluctuation rate is very high. But after elapsing certain period of time, fluctuating becomes very low and then solution is being converged. Among them frictional resistance is converged very fast.

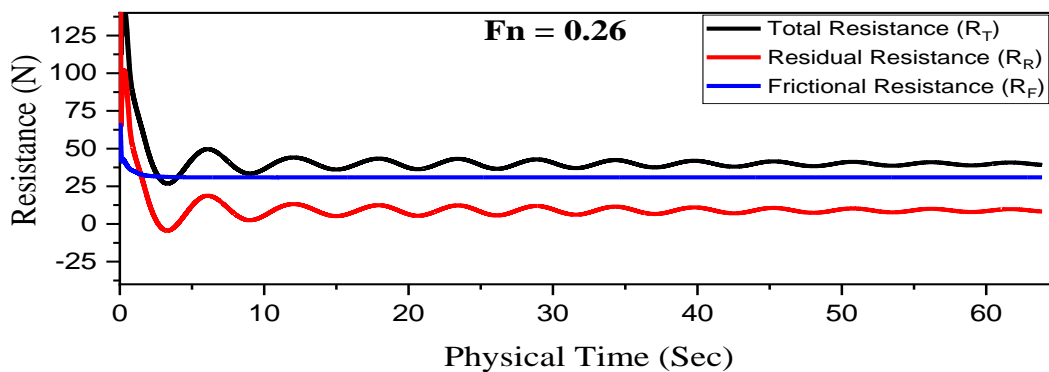


Fig. 5.14: Convergence history of Resistance of KCS hull at $Fn = 0.26$

The Predicted total resistance coefficients are shown in Fig. 5.15 with the experimental results. The total hull resistance increases as the speed (Froude No) increases. The curve of the total resistance followed a number of “hump” and “hollow” in the curve. First hollow occurred at Fn range 0.20-0.28 and then followed by significant hump at the peak at Fn about 0.52. As known the characteristic of the hollow and hump phenomena occurred in the resistance trend is due to the interference between the bow and stern transverse waves. Above the Froude number 0.52, the interference transverse bow and stern become less significant while the divergent waves become more and more important. As the ship moves, the energy given to the water by bow is carried out laterally and away from the ship and hence the height of each succeeding wave of each system decreases with no considerable change in wavelength results in a decrease in wave resistance and so decreases in total resistance. From the figure it has been shown at the very low Froude number the deviation between CFD and EFD [51] results is high but the discrepancy between these two is low at relative higher Froude number. The overall pattern of the resistance coefficient is quite satisfactory with the experimental results. The relative error between CFD and EFD values are given in Table 5.10.

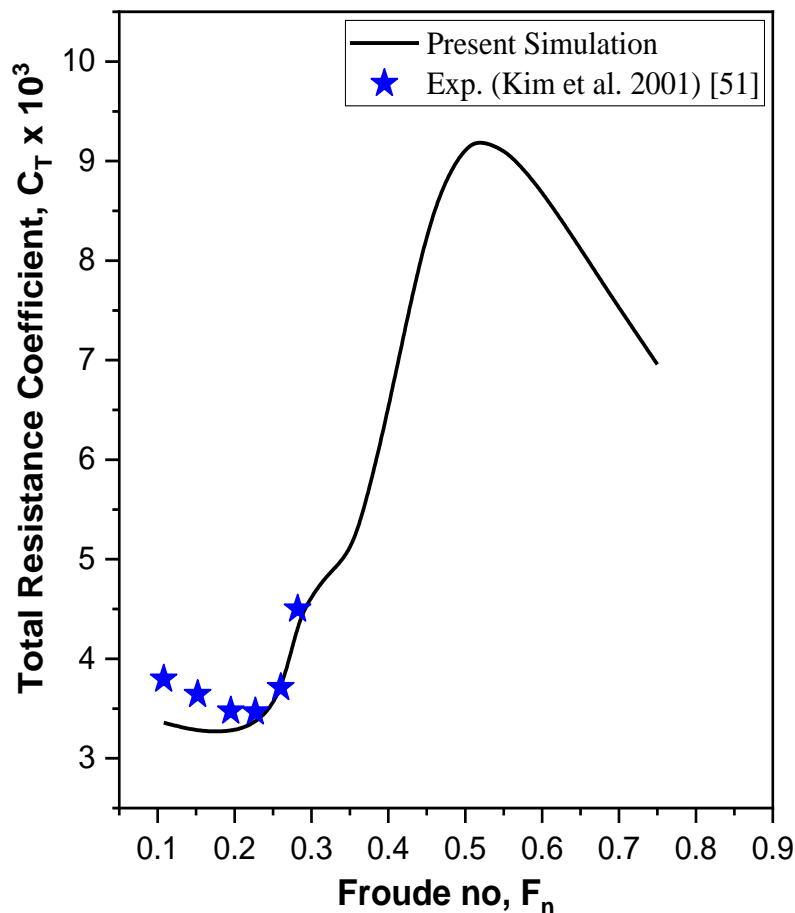


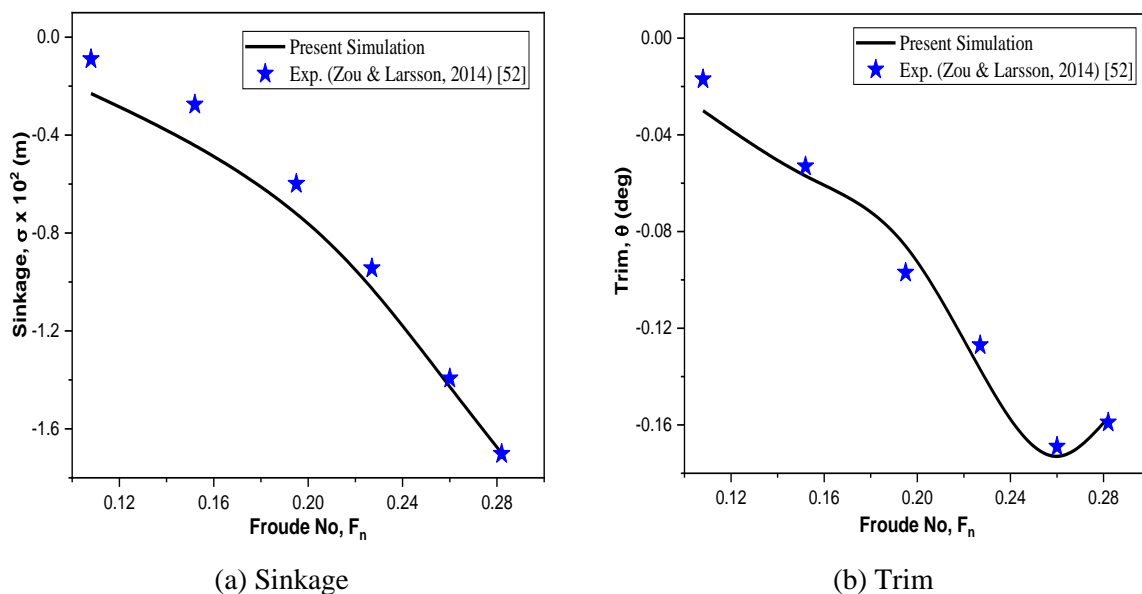
Fig. 5.15: Comparison of total resistance coefficients of KCS hull.

Table 5.10: Relative error analysis of total resistance coefficient for KCS hull

Froude No	Speed, V (m/s)	Reynolds No, Rn	$C_T \times 10^3$ (EFD)(S)	$C_T \times 10^3$ (CFD)(D)	Error
0.108	0.915	5.23×10^6	3.796	3.357	11.56 %
0.152	1.281	7.33×10^6	3.641	3.269	10.22 %
0.195	1.647	9.42×10^6	3.475	3.265	6.04 %
0.227	1.922	1.10×10^6	3.467	3.344	3.55 %
0.260	2.196	1.26×10^6	3.711	3.635	2.00 %
0.282	2.379	1.36×10^6	4.501	4.376	2.77 %

Sinkage and Trim

To investigate the dynamic behavior (in this case sinkage and trim), the KCS hull is simulated at free condition. Hull model is allowed to translate in the vertical direction and to rotate about the transverse axis. In the DFBI modeling, the release and the ramp time are chosen 1.0 sec and 5.0 sec. Release time gives some times to the fluid flow to be initialized before the motion calculation begins. Force and moments are applied on the hull body at the Ramp time and at this time solutions are carried out by reducing the oscillation. In Fig. 5.16 (a), the sinkage of KCS increases at the downward direction with the increasing Froude numbers. Fig. 5.16 (b) shows the changing trend of trim angle at different Froude numbers. The negative value of trim angle means trim by bow. Both the sinkage and trim values are compared with the experimental results [52] and a good consistency is found between those.

**Fig. 5.16: Comparison of (a) Sinkage and (b) Trim for KCS hull**

The relative error analysis for sinkage and trim are given in Table 5.11. The present Computational Fluid Dynamics (CFD) results indicated by simulation (S) are compared with the Experimental Fluid Dynamics (EFD) indicated by data (D) for 6 (Six) Froude numbers.

$$|Error| = \left| \frac{S - D}{D} \right| \times 100$$

At the low Froude number the relative error is quite high for both sinkage and trim predictions. At the low speed, the Reynolds number is lower than the higher speed. It increases the laminar boundary layer and turbulent boundary layer thickness. Moreover, the mesh resolution can be a reason for this high deviation and prediction can be improved by applying a higher mesh resolution. The deviation margin decreases with increase in Froude number, Fn. With the increasing Froude numbers especially at the Froude numbers 0.260 and 0.282, the differences are only 4.02% and 0.12% to the experimental data for Sinkage and differences are 1.77% and 1.26% to the experiments for the Trim values.

Table 5.11: Relative error analysis of Sinkage and Trim for KCS hull

Froude No	Speed, U(m/s)	Sinkage, CFD (S)	Sinkage, EFD (D)	Error	Trim, CFD (S)	Trim, EFD (D)	Error
0.108	0.915	-0.23	-0.09	---	-0.03	-0.017	76.5%
0.152	1.281	-0.43	-0.275	56.4%	-0.057	-0.053	7.55%
0.195	1.647	-0.70	-0.599	16.86%	-0.086	-0.097	11.3%
0.227	1.922	-1.01	-0.944	6.99%	-0.137	-0.127	7.87%
0.260	2.196	-1.45	-1.394	4.02%	-0.172	-0.169	1.77%
0.282	2.379	-1.70	-1.702	0.12%	-0.157	-0.159	1.26%

Pressure Field

The pressure distribution over the hull surface is shown in Fig. 5.17 for different Froude numbers. Pressure is normalized by the $\frac{1}{2}\rho U^2$ term, where ρ is the fluid density and U is the free stream velocity. In the calm water condition, maximum pressure met at the bow of the ship hull. Moreover the appendage section: rudder experiences a high pressure as shown in the figure.

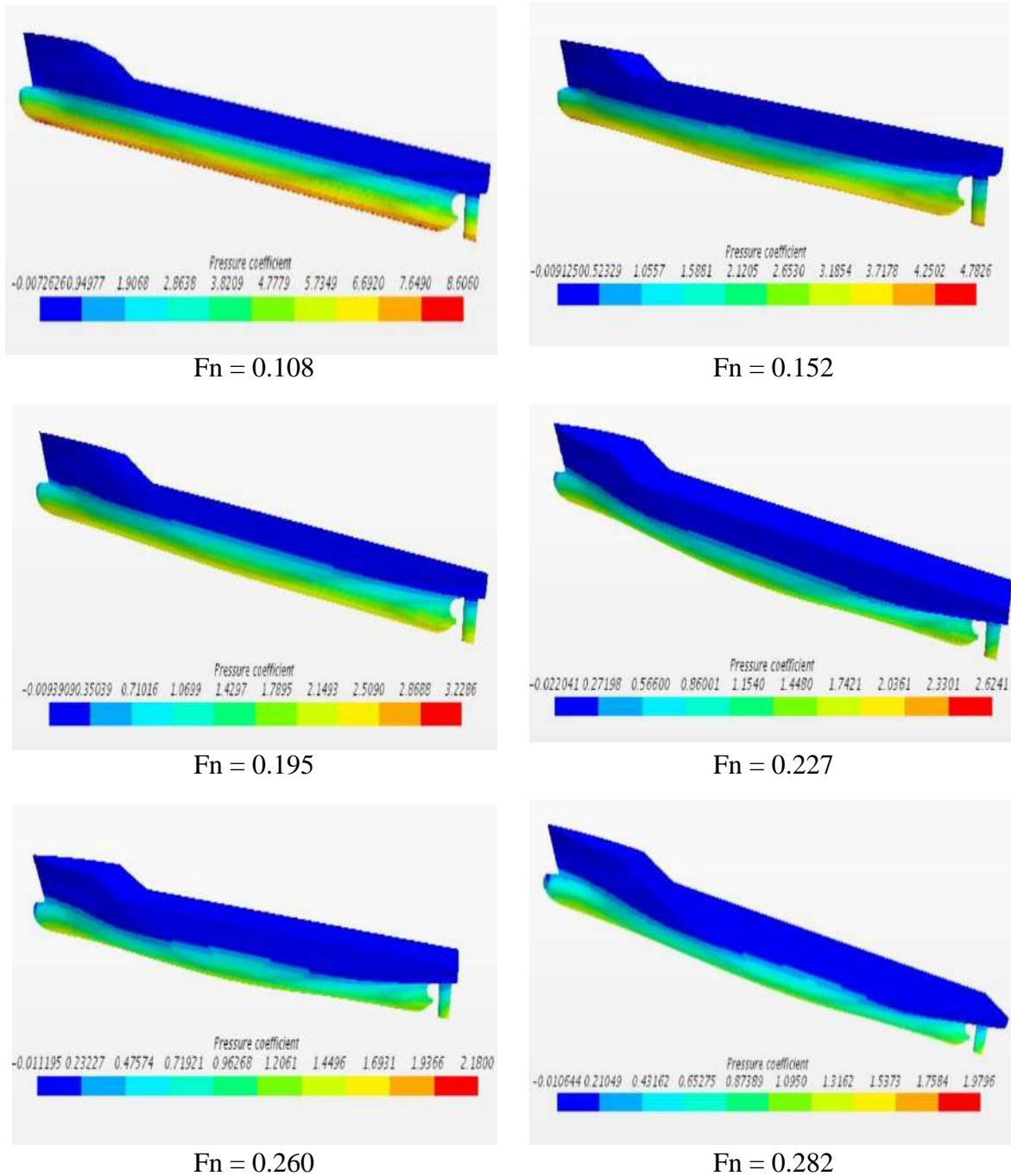


Fig. 5.17: Pressure distribution over the surface of Wigley hull

Wave Field

Figure 5.18 shows the generated Kelvin wave pattern (wave contour) for different Froude number. The wave pattern consists of the transverse and diverging waves as shown in figure. There are very less disturbance of wave surface at the low Froude number, however, the

disturbance of wave surface augments with the increasing Froude numbers and therefore the wave making region spread outward from the bow and the ship itself as well.

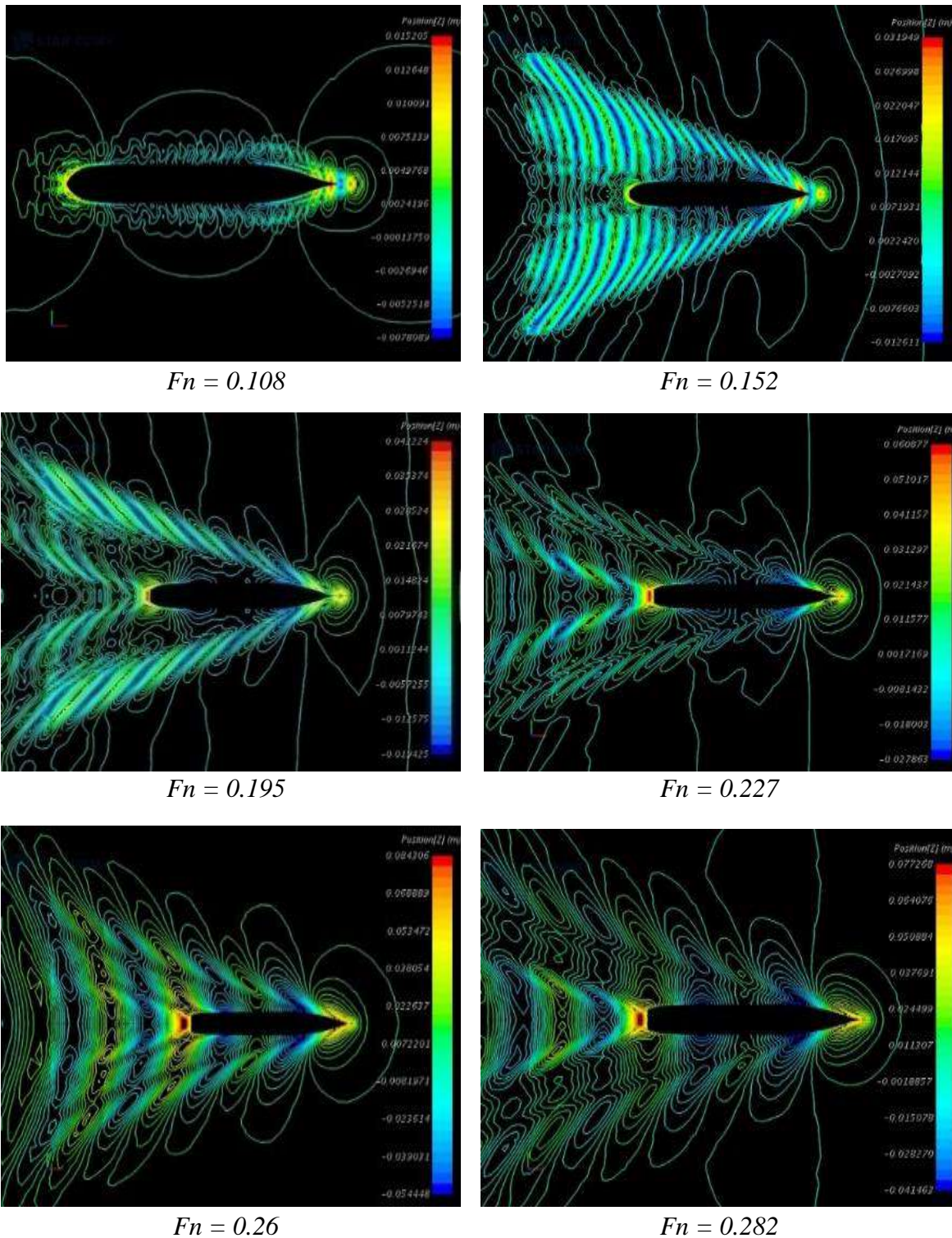


Fig. 5.18: Kelvin Wave pattern for KCS hull at different Froude numbers

Simulated Kelvin wave pattern at Froude no of 0.26 is compared with the experimental wave pattern as shown in the Fig. 5.19. A good agreement in wave height and position of the wake are found and this achievally assure the accuracy of CFD analysis around the hull form.

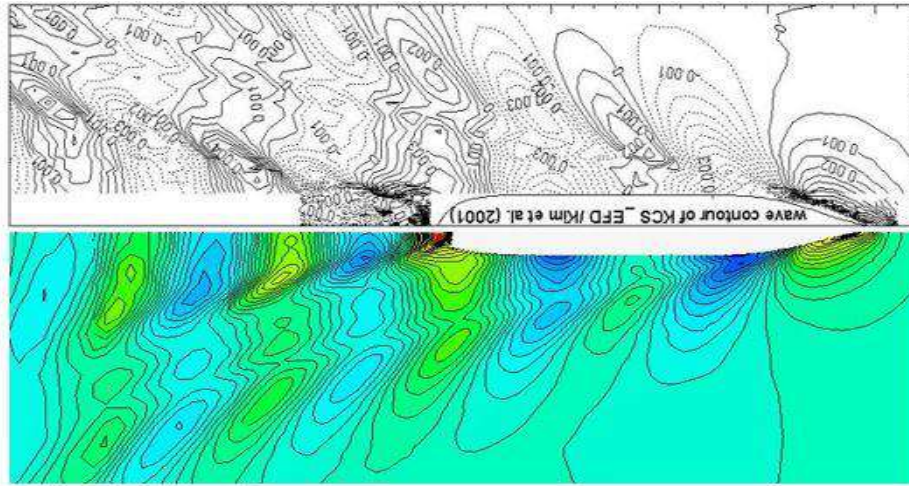


Fig. 5.19: Comparison of Kelvin wave pattern of KCS hull between CFD (bottom) and EFD (top)

The wave profile around the KCS at $F_n = 0.26$ is plotted against the experimental data and shown in Fig. 5.20. Wave height and location along the hull both are normalized by the length of the hull. In the RANS method, the highest wave crest occurs at the stern and bow region of the ship hull. The bow region is placed at the $x/L=0.5$ and the stern is placed at the $x/L=-0.5$. Therefore, the highest wave crests are found at those locations as shown in the figure.

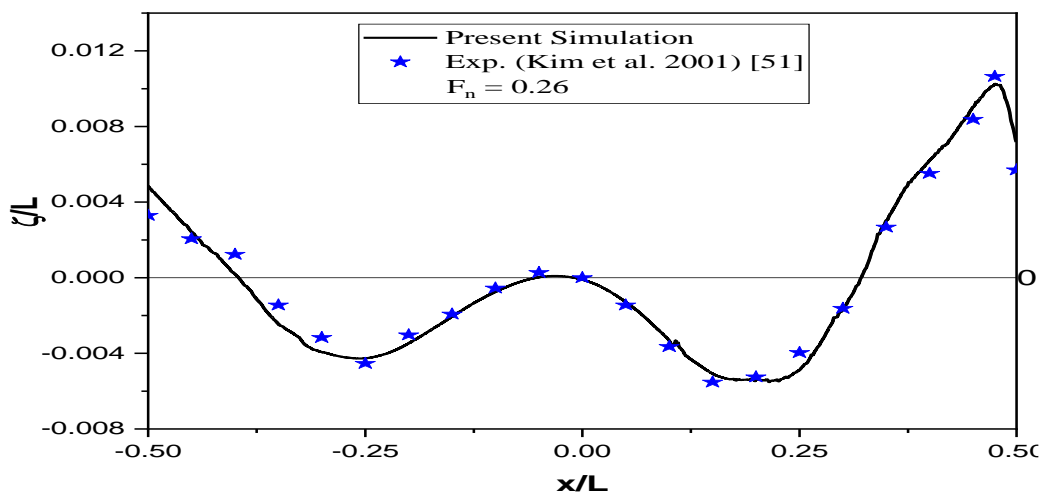


Fig. 5.20: Wave profile along the KCS hull

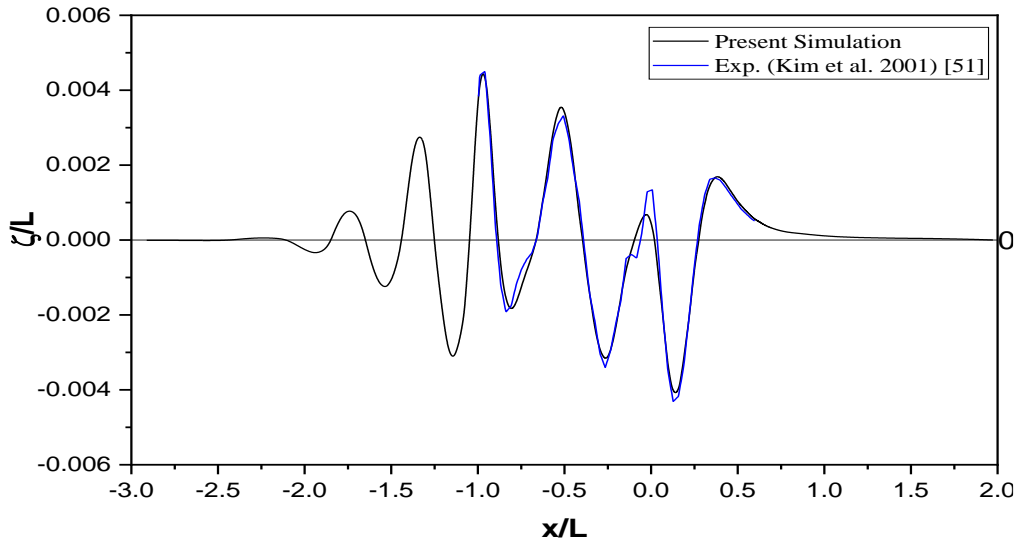


Fig. 5.21: Transverse wave cut of KCS hull

Transverse wave cut is found at the intersection of the wave pattern at the distance of $1.098m$ from the center line of the ship. This distance is also normalized by the length between perpendiculars of the ship. Transverse wave cut analysis is presented in Fig. 5.21 with the available experimental data. A good agreement is found in this wave cut result.

Grid Dependence Test

Total three solutions with the uniform mesh refinement to the three directions of the whole domain equal to $r = \sqrt{2}$ recommended by ITTC [53] are used in this present study. Total calculation procedures has already been carried out in the Wigley hull section 5.1. The grid properties with the corresponding numerical results are given in Table 5.12.

Table 5.12: Grid properties for C_T , Sinkage, and Trim

Grid No	Cell No	$r = h_i/h_1$	$C_T \times 10^3$	Sinkage, (m)	Trim, (deg)
Grid 1	1057126	1.000	3.650	-0.0143	-0.170
Grid 2	531014	1.414	3.635	-0.0145	-0.172
Grid 3	303224	2.000	3.590	-0.0149	-0.182

The simulated results for KCS hull at the three grids are given in Table 5.13 with the relative solution changes (ϵ), relative error ($E\%D$) and EFD (D) is also given for the comparison. The convergence ratio R_G , order of accuracy p_G , correction factor C_G , and the numerical uncertainty U_{SN} are given in Table 5.14.

Table 5.13: Grid convergence study for C_T , Sinkage, and trim for KCS hull

Grid	S_1 (Grid 1)	S_2 (Grid 2)	S_3 (Grid 3)	EFD (D) Data
$C_T \times 10^3$	3.650	3.635	3.590	3.711
$E\%D$	1.64	-2.14	-3.26	
$\varepsilon\%$	0.41	1.24	---	
$\sigma (m) \times 10^2$	-1.43	-1.45	-1.49	-1.394
$E\%D$	2.58	4.02	6.88	
$\varepsilon\%$	-1.40	-2.76	---	
θ (deg)	-0.170	-0.172	-0.182	-0.169
$E\%D$	0.59	1.77	7.69	
$\varepsilon\%$	-1.17	-5.81	---	

Table 5.13 shows that the relative solution change between Grid 1 and Grid 2 is less than change between Grid 2 and Grid 3 that indicates the state of convergence.

Table 5.14: Verification of C_T , Sinkage, and trim for KCS hull

Study	R_G	p_G	C_G	U_{SN}
C_T	0.33	3.17	2.00	0.6 % S_1
$\sigma (m)$	0.50	2.00	1.00	1.4 % S_1
τ (deg)	0.20	4.64	4.00	2.0 % S_1

From the Table 5.14 it has been shown that the convergence ratio R_G for all the solutions falls in this limit: $0 < R_G < 1$. That indicates the monotonic convergence and the further carried out results are grid independent. For monotonic convergence, the errors and numerical uncertainties are calculated using generalized Richardson Extrapolation (RE). The order of accuracy for resistance and trim are higher than the theoretical order of accuracy of 2 that is perfectly attainable for the sinkage.

Validation

From the verification study, numerical uncertainties are obtained. The comparison error E , validation uncertainty U_V , experimental data uncertainty U_D are calculated for validation process which is explained in details in Stern [43]. These values are shown in Table 5.15.

Where the symbol D is denoted for the EFD data. All the calculated values are shown as percentage of the EFD value. The absolute value of comparison error is calculated as

$$|E|\%D = \left| \frac{S - D}{D} \right| \times 100$$

S is the simulation result for finest grid.

Table 5.15: Validation of C_T , Sinkage, and trim for KCS hull

Study	$ E \%$	$U_V\%$	$U_D\%$
C_T	1.62 %D	2.67 %D	2.5 %D
σ (m)	2.58 %D	6.47 %D	2.5 %D
τ (deg)	0.59 %D	5.52 %D	2.5% D

From Table 5.15 it has been observed that the comparison error for three cases are less than the validation uncertainties. According to Wilson [44], this condition ($|E| < U_V$) implies that the results are well validated. However, for the sinkage and trim, the results are validated with the higher validation uncertainty level 6.47%D and 5.52%D respectively.

Figure 5.22 shows a grid dependency study of wave profile along the hull for three number of mesh arrangement namely Grid 1 (Finest), Grid 2 (Medium), and Grid 3 (Coarse) respectively and a satisfactory agreement is found with the experiment results of Kim *et al.* (2001) [51].

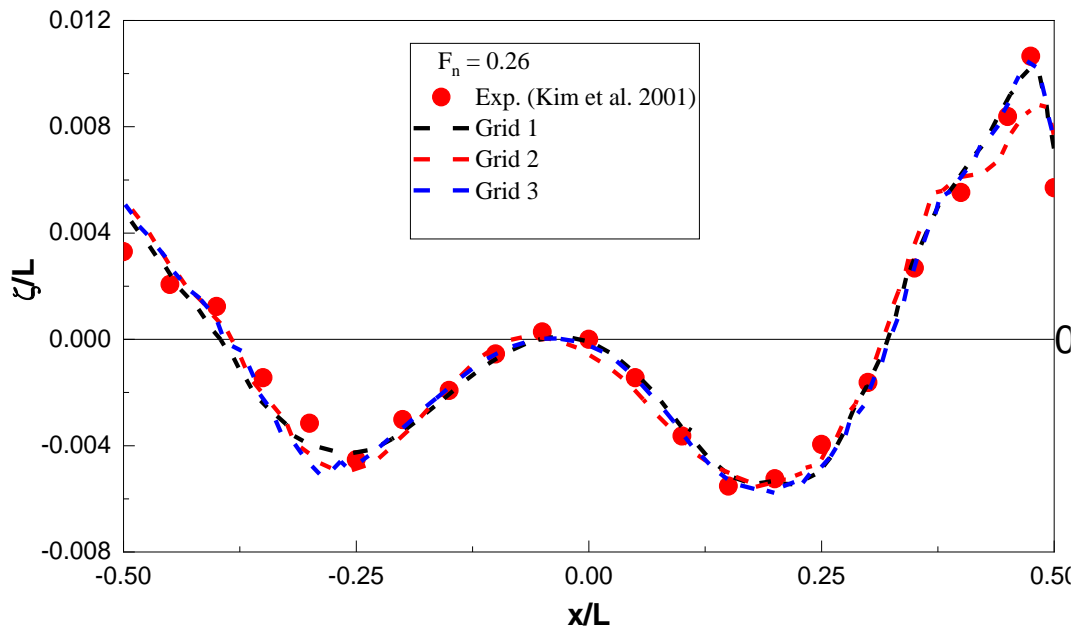


Fig. 5.22: Grid dependency study of wave profile for KCS hull

5.3 Series 60 Hull

Series 60 hull is extensively used in numerical and experimental studies. Several towing tank tests were carried to investigate the hydrodynamic behaviors which are very crucial to know at the initial stage of design. The principal particulars of Series hull are given in Table 5.16 and its surface mesh is shown in Fig. 5.23.

Table 5.16: Main Particulars of Series 60 Hull

Particulars		Value
Length (m)	L (m)	1.0
Breadth (m)	B (m)	0.1333
Draft (m)	H (m)	0.0533
Block coefficient	C_B	0.6
Mid-ship coefficient	C_x	0.977
Wetted surface area coefficient	C_s	0.710
Vertical center of gravity	KG (m)	0.051
Moment of inertia	K_{xx} / B	0.40
	K_{yy} / L	0.25
	K_{zz} / L	0.25

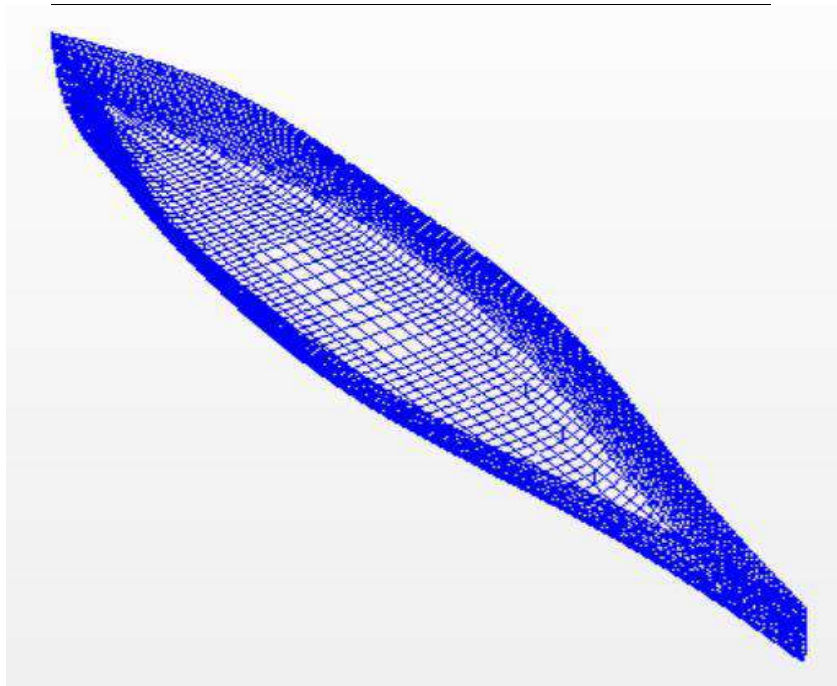


Fig. 5.23: Grid distribution on the surface of Series 60 hull

The size of one-half of the computational domain is $-2.6 L < x < 1.5 L$, $0 < y < 2.0 L$, $-1.5 L < z < 0.2 L$ and is taken into account due to vertical plane symmetry as shown in Fig. 5.24. Numerical simulation is carried with the model of $L = 1$ m in a computational domain has the dimension of $4.1m \times 2m \times 1.7m$. A prism layer hexahedral mesh is applied and generates **300065** control volume cells within the domain.

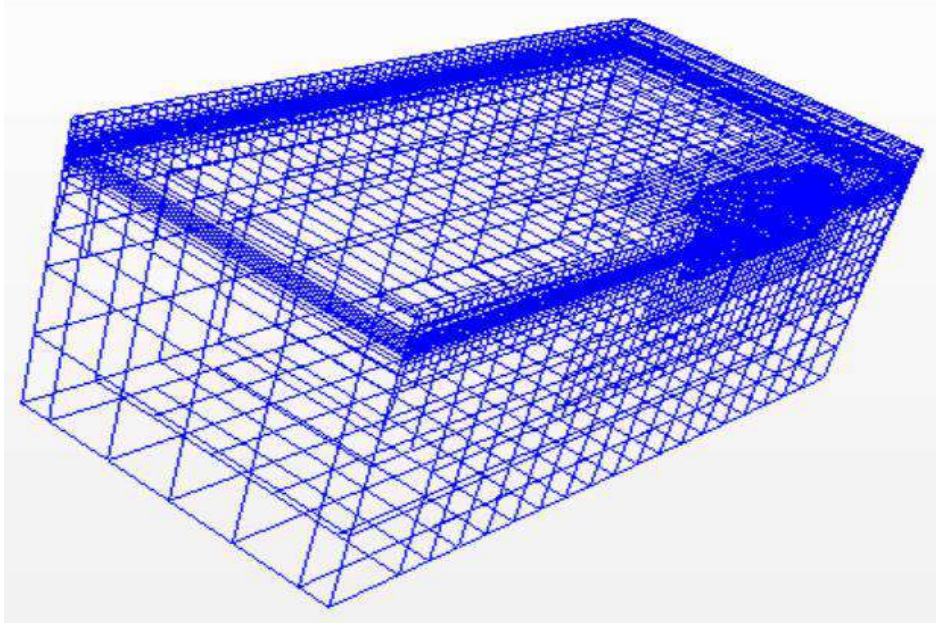


Fig. 5.24: Mesh structure for flow computation of Series 60 hull

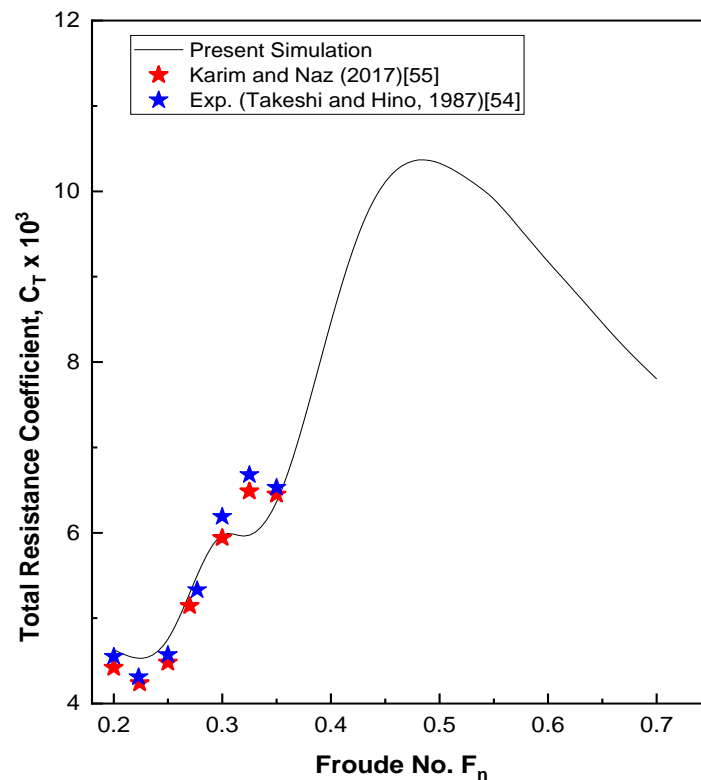


Fig. 5.25: Comparison of total resistance coefficient of Series 60 hull

The total resistance coefficients for various Froude numbers ranging from $F_n = 0.20$ to 0.72 are computed and compared with the experimental results [54] and the results obtained by Karim and Naz [55] as shown in Fig. 5.25. A fairly good agreement is found among these results. The curve of the total resistance followed a number of “hump” and “hollow” in the curve. First hollow occurred at F_n range $0.2-0.25$ and 2nd occurred at F_n range $0.31-0.35$ and then followed by significant hump at the peak at F_n about 0.46 . Further from this Froude number, the resistance curve goes downward due to the less transverse wave interference between bow and stern waves and increase in wetted surface area as well.

The comparison between the obtained simulation results and experimental results [56] for wave profile along the hull are shown in Fig. 5.26. The highest wave crest is found at the bow location where maximum pressure is subjected for every Froude number. The series 60 hull has a large B/L ratio equal to 0.133 and hence wave profile has some discrepancy with the experimental data as shown in figure.

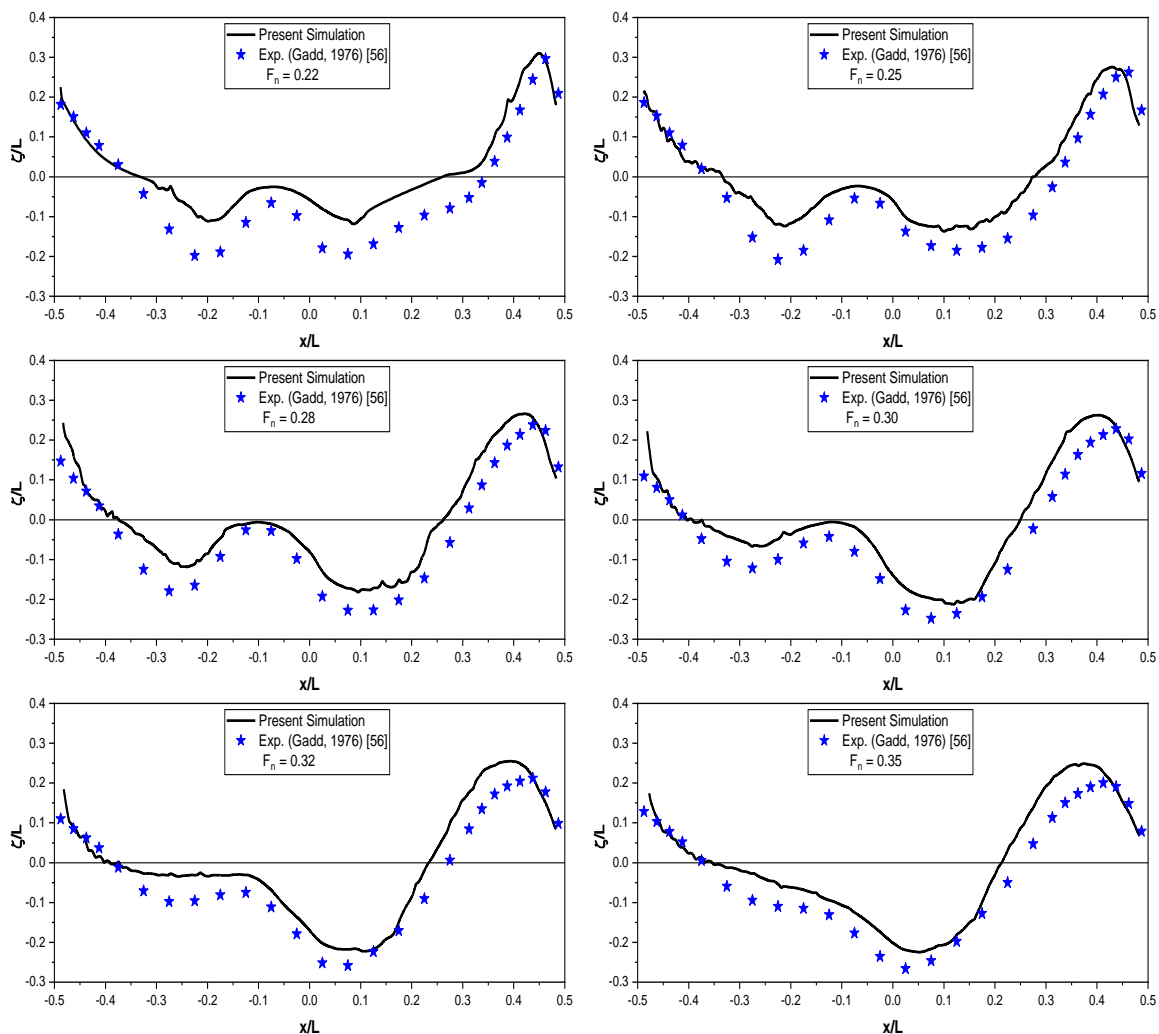


Fig. 5.26: Wave profile along the Series 60 hull at different Froude numbers

Figure 5.27 shows the wave contour at different Froude numbers. At the low Froude numbers 0.22 and 0.25, the disturbance of the wave surface is low and hence wave making region spreads less from the hull body. On the contrary, with the increasing Froude number, the surface wave disturbance increases and wave waking region spreads more from the bow region.

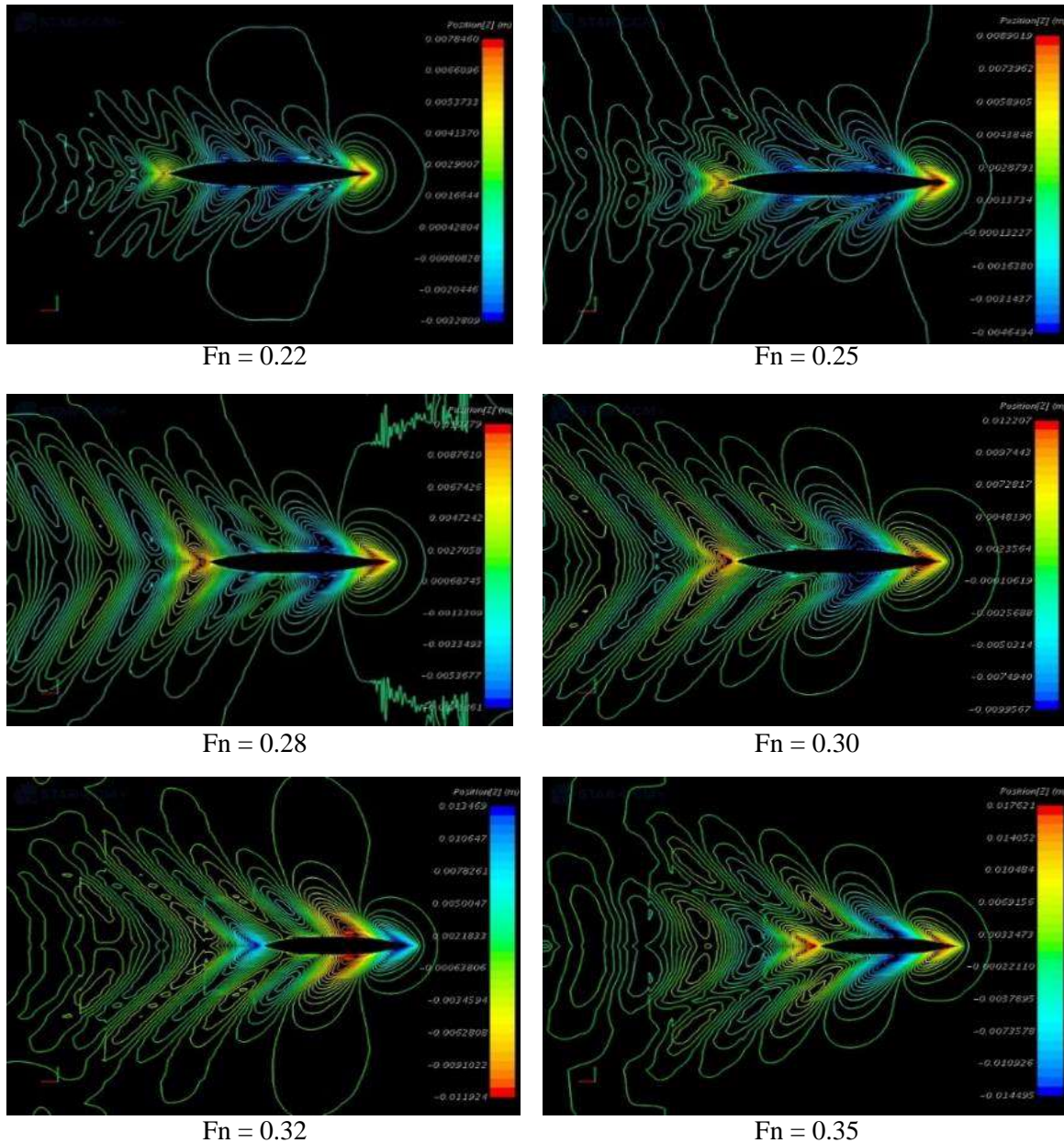


Fig. 5.27: Kelvin Wave pattern for Series 60 hull at different Froude numbers

Furthermore, for Froude numbers 0.25 and 0.32 the simulated wave patterns are compared with the numerical analysis by Huang [57]. A very good agreement has been found between these two results as shown in Fig. 5.28, where the left side figures are for Huang [57] and the right side figures are for present study.

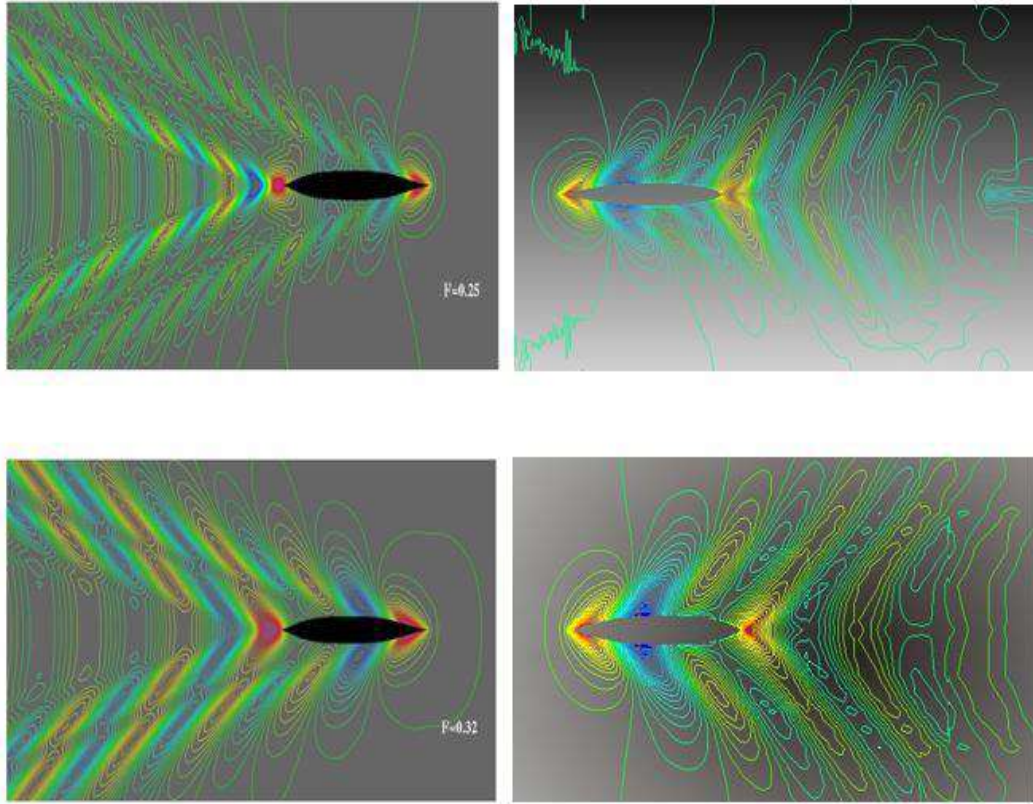


Fig. 5.28: Comparison of wave pattern between Huang[57] (Left) and present study (Right)

Grid Dependence and Validation

The mathematical procedures and detailed calculation of V&V study have already been discussed in the case of Wigley and KCS hulls. The tabulated results of total resistance coefficient are presented here for the Series 60 hull.

Table 5.17: Grid properties for C_T at $Fn = 0.30$

Grid No	Cell No	$r = h_i/h_1$	$C_T \times 10^3$
Grid 1 (Finest)	587743	1.000	5.97
Grid 2 (Medium)	300065	1.414	6.05
Grid 3 (Coarse)	178391	2.000	6.45

Table 5.18: Grid convergence study for C_T Series 60 hull

Grid	S_1 (Grid 1)	S_2 (Grid 2)	S_3 (Grid 2)	EFD Data
$C_T \times 10^3$	5.97	6.05	6.45	5.94
ε		1.34 %	6.62 %	

Table 5.19: Verification of C_T for Series 60 hull

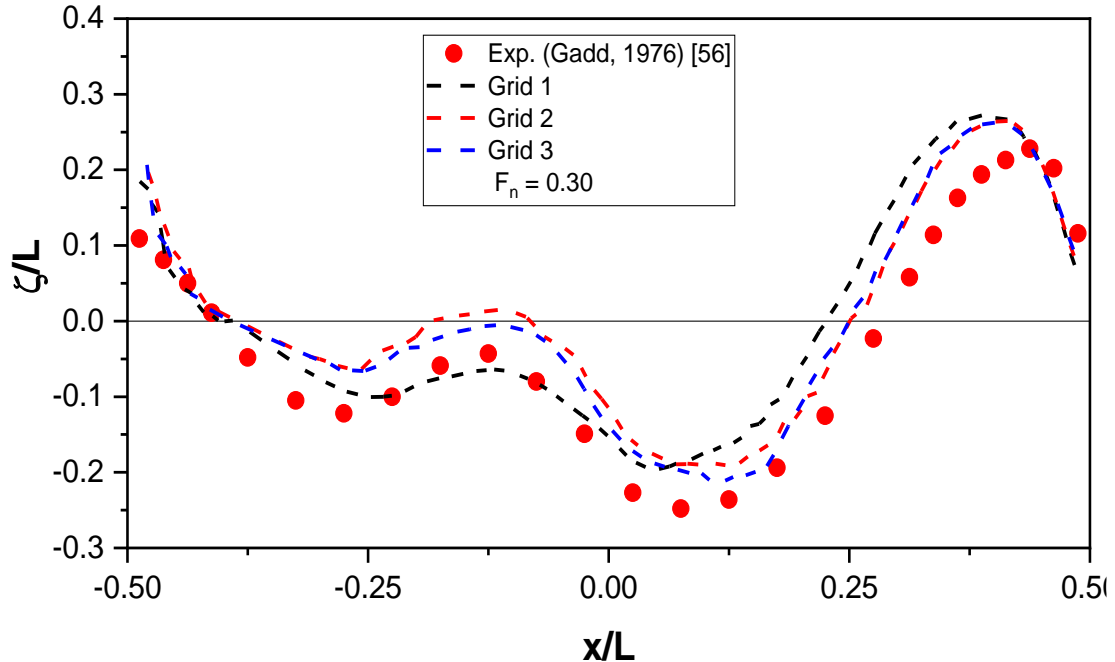
Study	R_G	p_G	C_G	U_{SN}
C_T	0.2	4.64	4.00	2.34 % S_1

Table 5.20: Validation of C_T for Series 60 hull

Study	$ E \%$	$U_V\%$	$U_D\%$
C_T	0.51 %D	3.43 %D	2.5 %D

Table 5.18 shows that the relative solution change between Grid 1 and Grid 2 is less than change between Grid 2 and Grid 3 that indicates the state of convergence. Table 5.20 presents that the relative is less than the validation uncertainties and this condition ($|E| < U_V$) implies that the results are well validated.

Figure 5.29 presents the grid dependency study on the wave profile at Froude number 0.30. It has been shown that there is a good consistency level among the grid results and has a compatibility with the experimental result as well.

**Fig. 5.29: Grid dependency on wave profile for Series 60 hull**

5.4 HSVA Tanker

The HSVA tanker is a limiting case with its high value of block coefficient and low range of Froude numbers. The principal particulars of HSVA Tanker are given in Table 5.21 and its surface mesh is shown in Fig. 5.30.

Table 5.21: Main Particulars of HSVA

Particulars	Value
L (m)	5.00
B (m)	0.7575
H (m)	0.2805
C_B	0.8503
$C_S = S/L(2H + B)$	0.8815
∇ (m^3)	0.9034
S (m^2)	5.8113

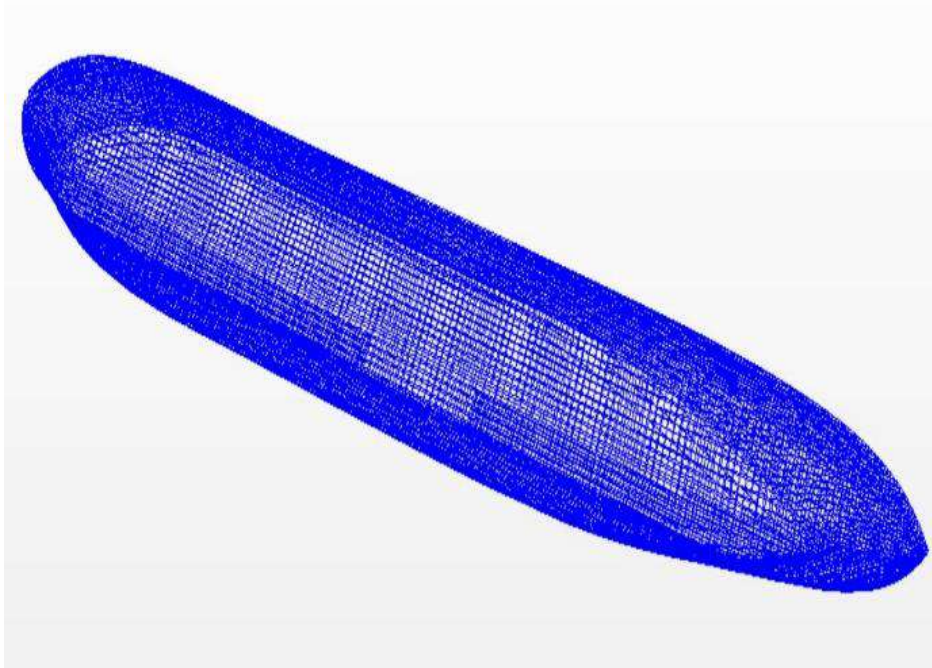


Fig. 5.30: Surface mesh on the HSVA Tanker

The origin of the coordinate system is located in an undisturbed free surface at midship so that the undisturbed incident flow appears to be a streaming flow in the positive direction. The z axis is vertically upward and the y axis extends to portside. The size of one-half of the computational domain shown in Fig. 5.31 is $-2.5L < x < 1.5L$, $0 < y < 2L$, $-1.5L < z <$

0.3L and is taken into account due to vertical plane symmetry that leads to reduce the number of element and to require less time to converge the problem. The mesh discretization view of the computational domain is shown in Fig. 5.32.

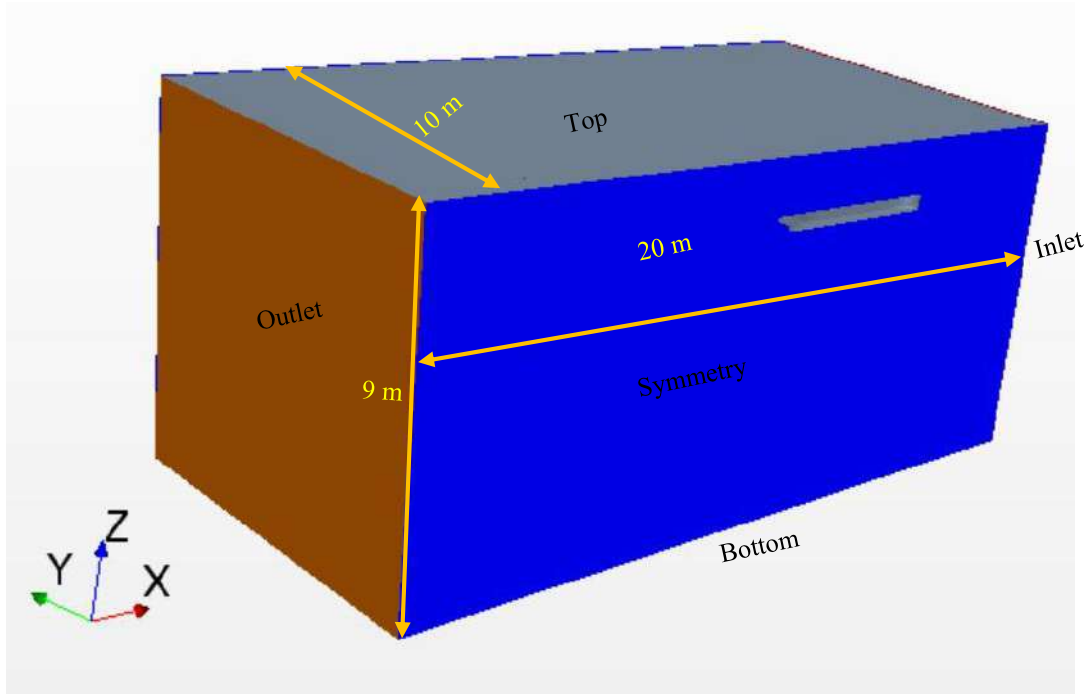


Fig. 5.31: Computational domain of HSVA Tanker

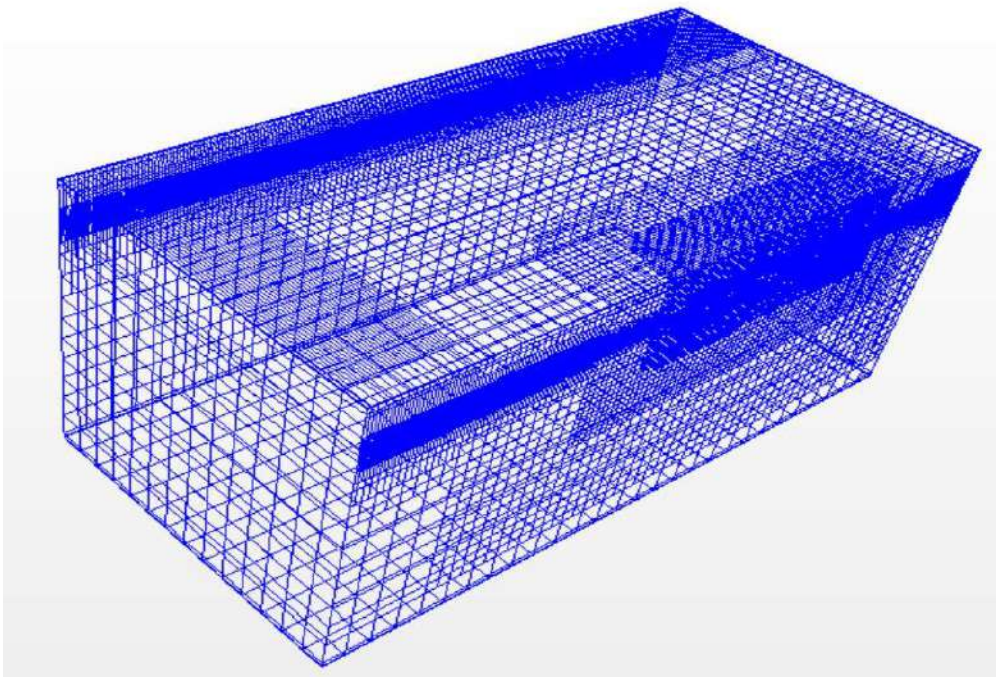


Fig. 5.32: Mesh structure for flow computation of HSVA Tanker

The numerical analysis is carried out for Froude numbers ranging 0.13-0.19 and computed total resistance coefficients are compared with the experimental results (Collatz [58]) as shown in Fig. 33. Simulated resistance coefficients are over predicted than the experimental but the overall trend has a good compatibility with the experiment.

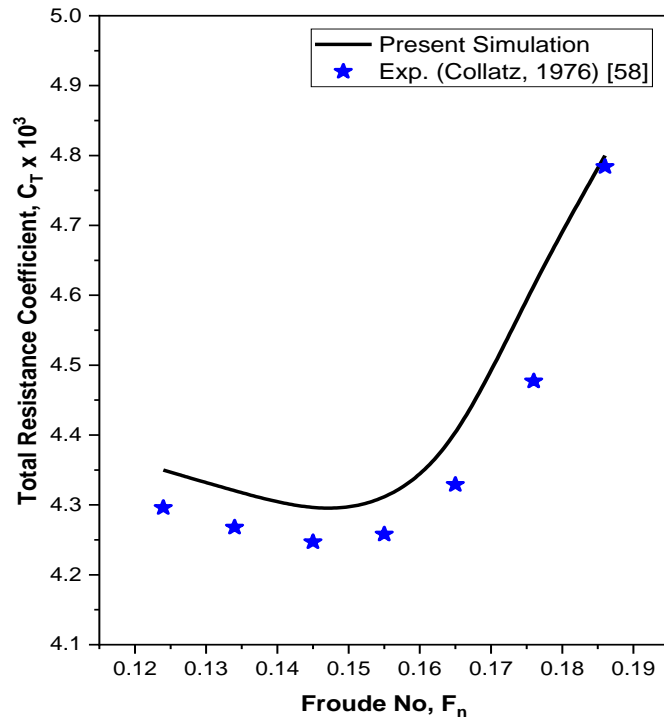


Fig. 5.33: Comparison of total resistance coefficient for HSVA tanker

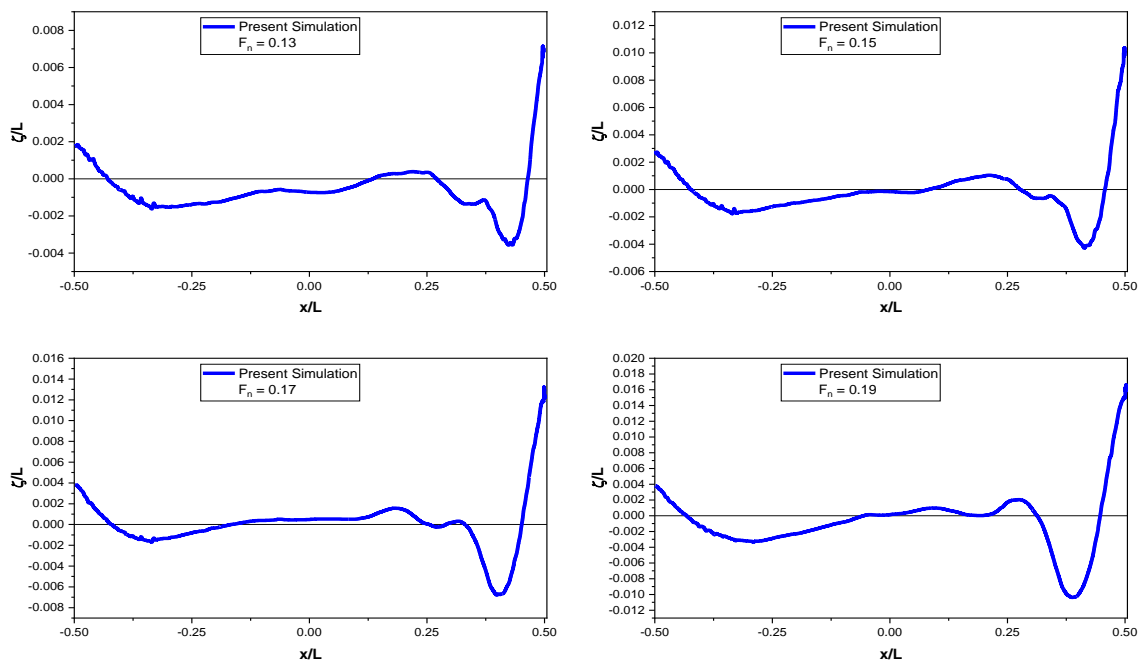


Fig. 5.34: Wave profile along the HSVA hull at different Froude numbers

Figure 5.34 shows the wave profile around the HSVA tanker at the Froude numbers 0.13, 0.15, 0.17 and 0.19. Only the results of the present analysis are presented here. From the figure it has been shown that the wave profiles are quite similar to each other as the Froude numbers are low and much closed to each other. However, the maximum wave height increases at the forward bow position ($x/L=0.5$) with the increasing Froude numbers.

5.5 Catamaran Hull

The catamaran hull is composed of two identical Wigley mono hulls and has the hull separation to length ratio (s/L) is 0.4. Each mono hull is 3m in length, 0.3m in breadth and 0.1875m in draft. The size of one-half of the computational domain is $-3.5 L < x < 1.5 L, 0 < y < 1.67 L, -1.0 L < z < 0.33 L$ and is discretized by **2957198** number of hexahedral cells as given in Fig. 5.35.

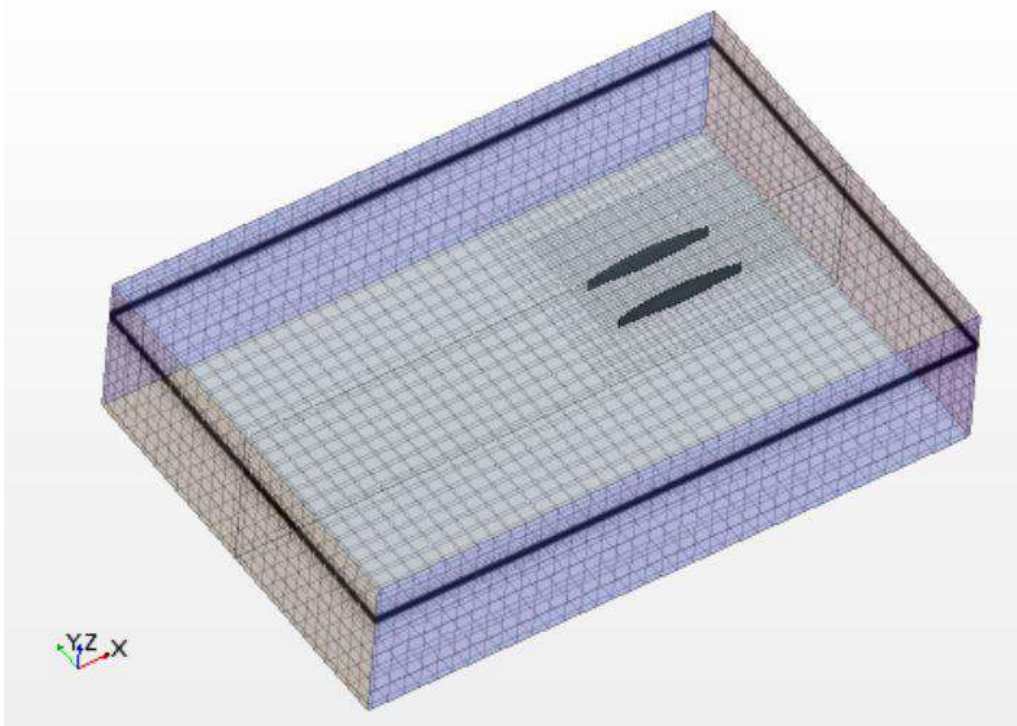


Fig. 5.35: Computational domain of the wigley catamaran hull

For the catamaran hull shown in Fig. 5.36 special care is taken at separation of the hulls where the highly complex flow likely to be generated. This is done by creating another rectangular volumetric block with stronger mesh refinement and at the free surface mesh refinement is also taken as refined mesh. The simulation results are obtained on a laptop consisting **Intel Core i5 1.8 GHz** and **8.0 GB RAM** and a total solver **CPU time 36 Hours** is needed to complete the entire simulation.

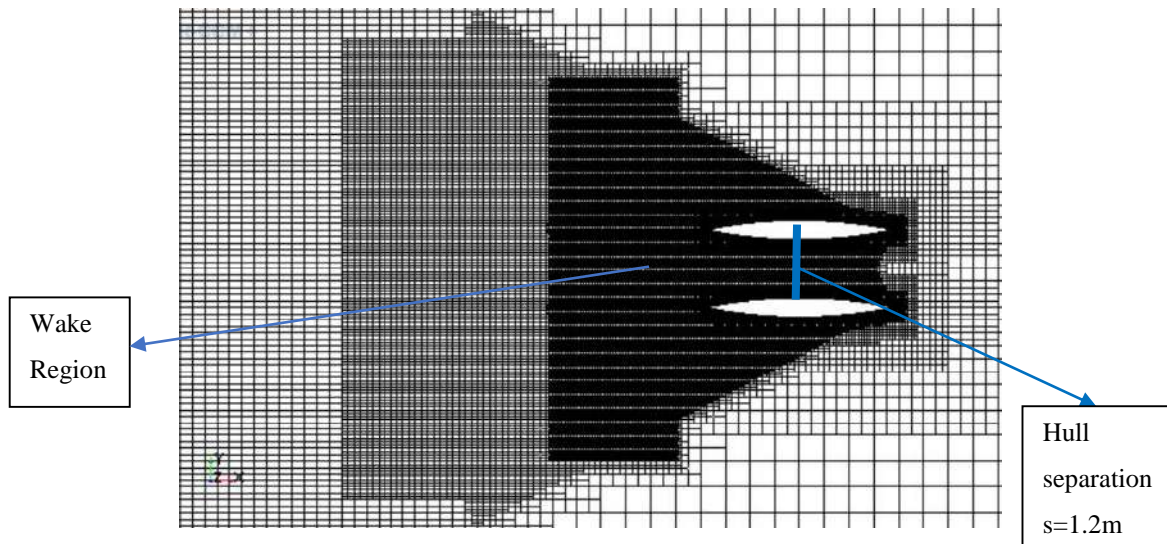


Fig. 5.36: Volume mesh with refinement at the hull separation and wake region

Wigley catamaran hull is simulated at various Froude numbers ranging from 0.2 to 0.75. The wave-making resistance of the catamaran hull is shown in Fig. 5.37 and exhibits broadly similar trends to those of the published monohull results as well as the experiment of Insel and Molland [22] and numerical results of Tarafder and Suzuki [24]. At the low Froude number, catamaran hull has a larger wetted surface area as the ship model in low speed and consequently viscous resistance greatly affects in the total resistance. With the increasing Froude numbers the wave resistance become dominants in the total resistance.

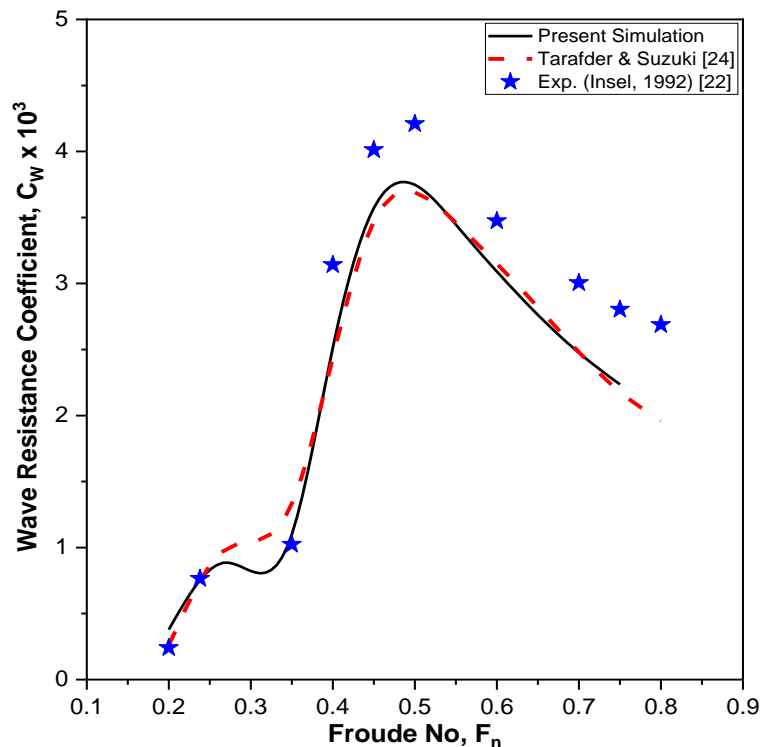


Fig. 5.37: Wave resistance coefficient comparison of Wigley catamaran hull

The ‘Hump’ and ‘Hollow’ in the wave resistance curve as shown in Fig. 5.38 are occurred due to the wave interference effect. Hump occurs when wave resistance arises drastically due to the coincidence of crest/trough of bow and stern transverse waves and the Hollow occurs when wave resistance falls significantly due to the coincidence of crest of bow and trough of stern waves. A significant peak value of wave resistance is found at Froude no around 0.5, above this Froude no, the divergent waves become more and more dominant and the height of each wave systems decrease with no considerable change in wavelength (i.e. less interference effect of transverse bow and stern waves). Therefore, the wave resistance decreases after reaching its highest value and would eventually die out.

The Kelvin-wave contours at Froude numbers 0.35, 0.40, 0.50 and 0.60 are shown in Fig. 5.38. From the figure it has been shown that the effect of wave interference between the hulls is trivial due to large separation ration $s/L=0.4$ and the pattern is likely to be similar as the mono hull. However, at the smaller value of separation (s) to length (L) ratio, the transverse wave becomes dominant over the divergent wave [23]. When this s/L ratio value becomes extremely smallest, the wave interference between hulls becomes so larger and the dominant transverse waves are circulated from the outer side of the hulls.

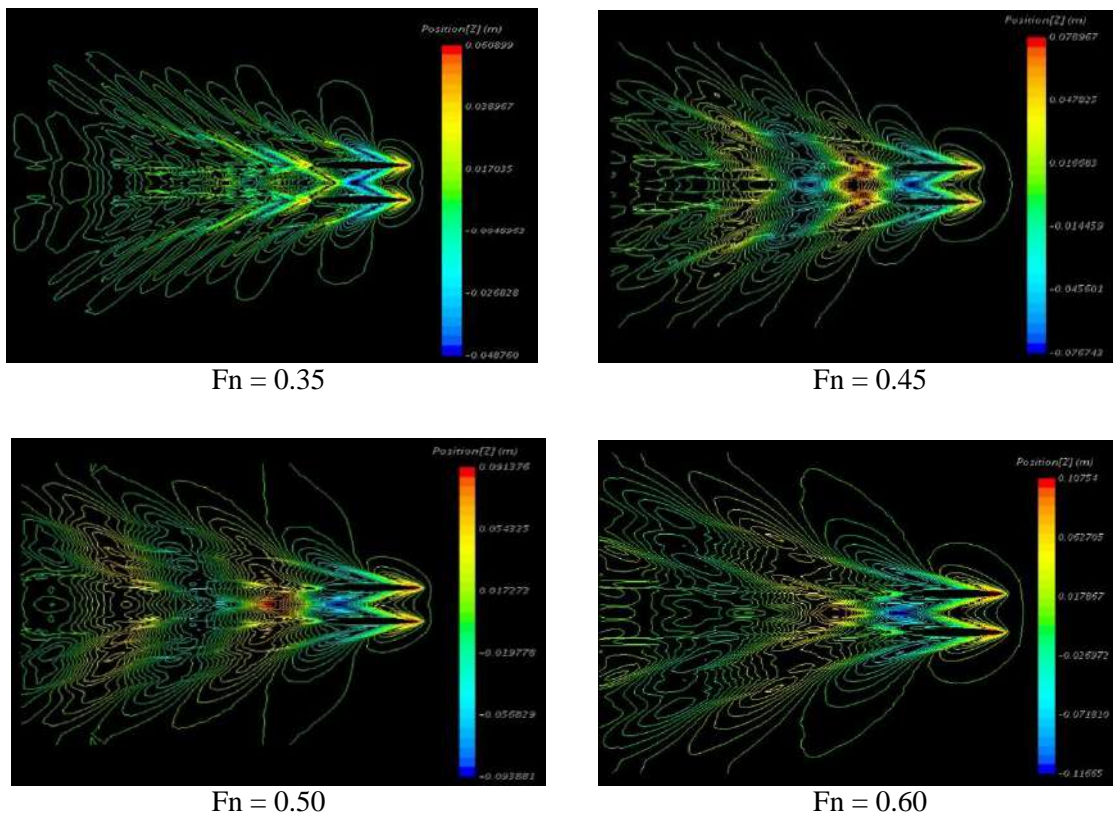


Fig. 5.38: Kelvin Wave pattern at different Froude numbers of Wigley catamaran ($s/L= 0.4$)

Figure 5.39 presents the wave profile for outer and inner side of a catamaran hull of $s/L=0.4$ for four Froude numbers 0.35, 0.45, 0.50, and 0.60 respectively. The difference in magnitude between the inner and outer wave elevation of the catamaran hull is low due to higher $s/L=0.4$ that leads to trivial wave interference. At the bow side the wave height of inner profile is slightly greater than that of the outer wave profile for every Froude number. This is so because the effect of the wave interference even though in small scale.

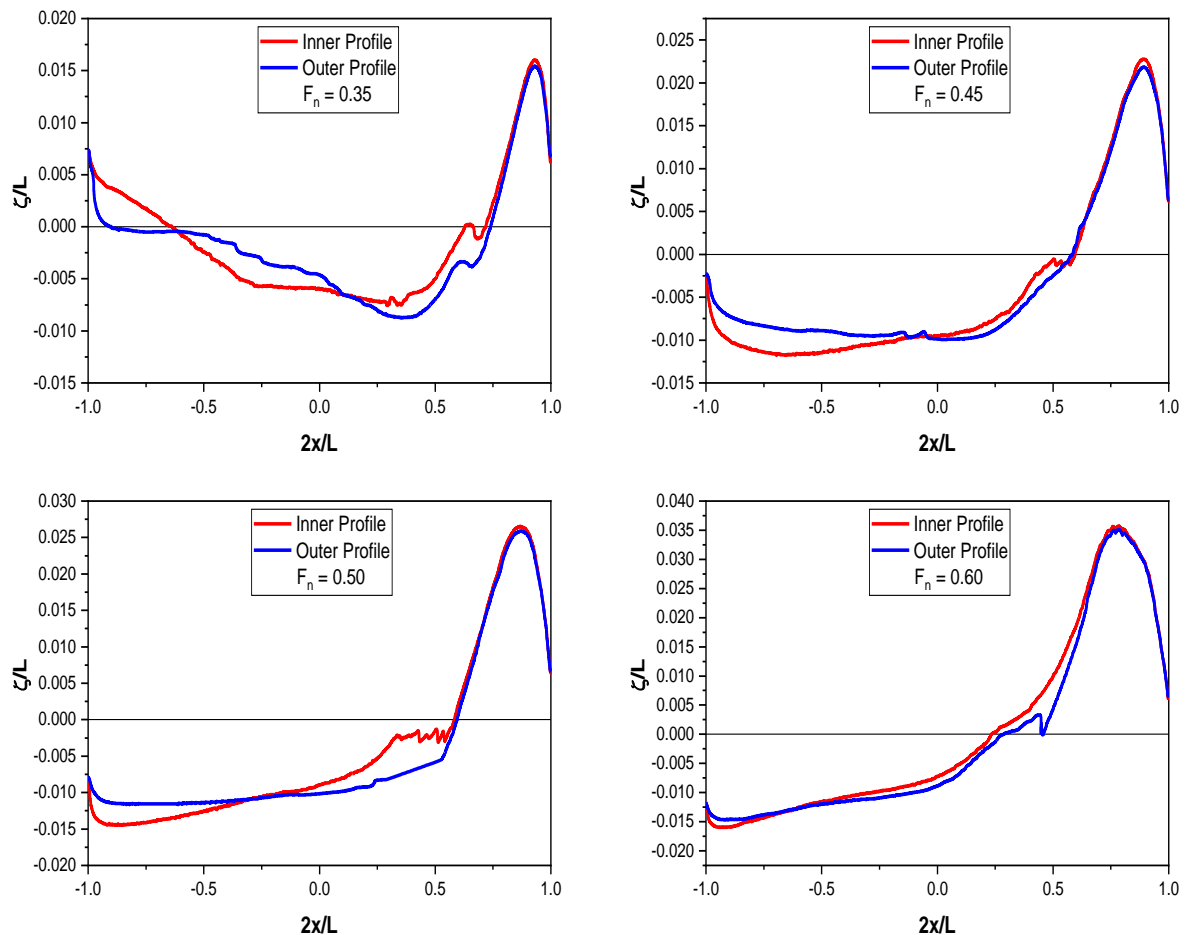


Fig. 5.39: Wave profile along the Wigley catamaran hull ($s/L=0.4$)

Figure 5.40 shows the pressure distribution on the surface of catamaran hull. Pressure is normalized by the $\frac{1}{2}\rho U^2$ term, where ρ is the fluid density and U is the free stream velocity. High pressure gradient is expected at the region where the flow interacts with the rapid changing geometry: the bow and stern regions are such geometries. From the figure it has been shown that the forward and aft portion of the ship experience larger pressure.

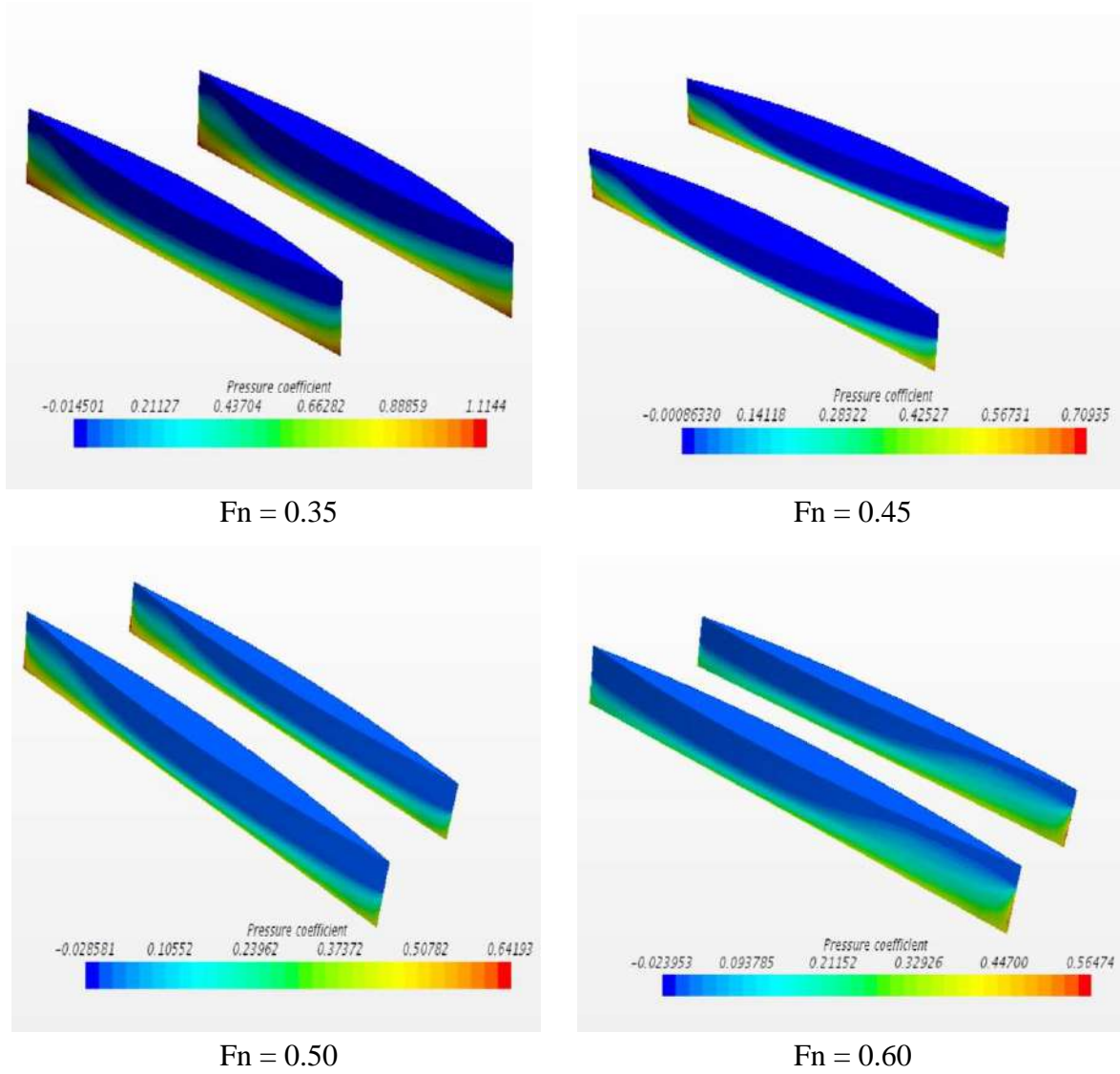


Fig. 5.40: Pressure distribution on the surface of Catamaran hull

Chapter 6

Conclusions

In present study, the turbulent flows around Wigley, KCS, Series 60, HSVA Tanker and a catamaran hull are investigated numerically using a commercial CFD code STAR-CCM+. The k- ϵ turbulence model in connection with SIMPLE algorithm is chosen to extract the velocity and pressure fields. The following conclusions can be drawn from the analysis:

- a) The standard k- ϵ turbulence model can be adopted as powerful tool to analyze the ship flow (resistance, sinkage and trim) except for the case where flow separations occur.
- b) The diverging waves radiating from the bow and stern are well predicted and look very similar to the wave pattern in deep water (Kelvin wave pattern).
- c) As expected the finer are the grids, the better is the accuracy at a cost of longer computation time. Reducing the grid size provides better representation of the bow and aft of the ship model. However, it increases the computation time drastically, and sometimes the CPU may not be able to compute the huge amount of data because of memory deficiency. Several grid refinement studies are performed, and the optimum grid size are chosen for resistance calculations.
- d) The magnitude of the wave elevation of the inner side of the catamaran hull is slightly higher than that of the outer side at the first crest of the bow. This difference is mainly due to the wave-interference effects.
- e) In general, the predictions are fairly good with experiment results for the increasing Froude numbers.

References

- [1] Zhao, F., Zhu, S. P., and Zhang, Z. R. Numerical experiments of a benchmark hull based on a turbulent free-surface flow model. *Computer Modeling in Engineering and Sciences*, Vol. 9(3), pp. 273-285, 2005.
- [2] Korkmaz, K. B., Orych, M., and Larsson, L. CFD predictions including verification and validation of resistance, propulsion and local flow for the Japan bulk carrier (JBC) with and without an energy saving device. In *Proc. Tokyo 2015 Workshop on CFD in Ship Hydrodynamics*, 2015.
- [3] Jones, W. P., & Launder, B. E. The prediction of laminarization with a two-equation model of turbulence. *International Journal of Heat and Mass Transfer*, Vol. 15(2), pp. 301-314, 1972.
- [4] Launder, B. E., & Sharma, B. I. Application of the energy-dissipation model of turbulence to the calculation of flow near a spinning disc. *Letters in Heat and Mass Transfer*, Vol. 1(2), pp. 131-137, 1974.
- [5] Menter, F. R. Two-equation eddy-viscosity turbulence models for engineering applications. *AIAA Journal*, Vol. 32(8), pp. 1598-1605, 1994.
- [6] Spalart, P., and Allmaras, S. A one-equation turbulence model for aerodynamic flows. In *30th Aerospace Sciences Meeting and Exhibit*, Vol. 1, pp. 5-21, 1994.
- [7] Huang, P. G., Bardina, J., & Coakley, T. Turbulence modeling validation, testing, and development. *NASA Technical Memorandum, 110446*, p. 147, 1997.
- [8] Azcueta, R. Ship resistance prediction by free-surface RANS computations. *Ship Technology Research-Schiffstechnik*, Vol. 47(2), pp. 47-62, 2000.
- [9] Adjali, S., Imine, O., Aounallah, M., and Belkadi, M. Numerical simulation of free surface water wave for the flow around NACA 0012 hydrofoil and wigley hull using VOF method. *International Journal of Mechanical and Mechatronics Engineering*, Vol. 9(5), pp. 884-888, 2015.
- [10] Tarafder, M. S., & Al Mursaline, M. Numerical computation of low Reynolds number viscous flow past bluff bodies. *International Journal of Applied Mechanics and Engineering*, Vol. 25(3), pp. 133-157, 2020.
- [11] Tarafder M S, Mursaline M A (2019). Numerical analysis of turbulent flow around two-dimensional bodies using non-orthogonal body-fitted Mesh, *International Journal of Applied Mechanics and Engineering*, 24(2), pp. 387-410.

- [12] Pranzitelli, A., Nicola, C., and Miranda, S. Steady-state calculations of free surface flow around ship hulls and resistance predictions. *High Speed Marine Vehicles (IX HSMV), Naples, Italy*; 2011.
- [13] Perez, G., Tan, M., and Wilson, P. A. Validation and verification of hull resistance components using a commercial CFD code. *11th Numerical Towing Tank Symposium, Brest, France*; 2008.
- [14] Karim, M. M., Rahman, M. H., and Yasin, M. H. Numerical Prediction of Free-Surface Wave around Surface Piercing Marine Rudder. *11th International Conference on Marine Technology MARTEC*, pp. 9-17, 2018.
- [15] Karim, M. M., and Naz, N. Numerical Study on Flow Around Modern Ship Hulls with Rudder-Propeller Interactions. *Journal of Marine Science and Application*, Vol. 18(4), pp. 400-416, 2019.
- [16] Ozdemir, Y. H., Cosgun, T., Dogrul, A., and Barlas, B. A numerical application to predict the resistance and wave pattern of KRISO container ship. *Shipbuilding: Theory and Practice of Shipbuilding and Marine Engineering*, Vol. 67(2), pp. 47-65, 2016.
- [17] Ahmed, Y. M. Numerical simulation for the free surface flow around a complex ship hull form at different Froude numbers. *Alexandria Engineering Journal*, Vol. 50(3), pp. 229-235, 2011.
- [18] Wang, X., and Walters, K. Computational analysis of marine-propeller performance using transition-sensitive turbulence modeling. *Journal of Fluids Engineering*, Vol. 134(7), 2012.
- [19] Karim, M. M., Prasad, B., and Rahman, N. Numerical simulation of free surface water wave for the flow around NACA 0015 hydrofoil using the volume of fluid (VOF) method. *Ocean engineering*, Vol. 78, pp. 89-94, 2014.
- [20] Yao, C. B., & Dong, W. C. Method to calculate resistance of high-speed displacement ship taking the effect of dynamic sinkage and trim and fluid viscosity into account. *Journal of Shanghai Jiaotong University (Science)*, Vol. 17(4), pp. 421-426, 2012.
- [21] Tu, T. N., Phuong, N. T. H., Anh, V. T., Ngoc, V. M., Hai, P. T. T., and Chinh, C. H. Numerical Prediction of Ship Resistance in Calm Water by Using RANS Method. *Journal of Engineering and Applied Sciences*, Vol. 13(17), pp. 7210-7214, 2018.

- [22] Insel, M. and Molland, A. F. An Investigation into Resistance Components of High-Speed Displacement Catamarans. *Transaction of Royal Institute of Naval Architects*, Vol.134, pp. 1 – 20, 1992.
- [23] Kwag, Seung-Hyun. Computation of flows around a high speed catamaran. *KSME International Journal*, Vol. 15(4), pp. 465-472, 2001.
- [24] Tarafder, M. S., and Suzuki, K. Computation of wave-making resistance of a catamaran in deep water using a potential-based panel method. *Ocean Engineering*, Vol. 34(13), pp. 1892-1900, 2007.
- [25] Tu, J., Yeoh, G. H., and Liu, C. *Computational Fluid Dynamics: A Practical Approach*. Butterworth-Heinemann; 2018.
- [26] Reynolds, O. Iv. On the dynamical theory of incompressible viscous fluids and the determination of the criterion. *Philosophical Transactions of the Royal Society of London.(a.)*, Vol. 186, pp. 123-164, 1895.
- [27] Boussinesq, J. Théorie de l'écoulement tourbillant. *Mem. Presentes par Divers Savants Acad. Sci. Inst. Fr.*, 23, pp. 46-50, 1877.
- [28] Sayma, A. *Computational Fluid Dynamics*. Bookboon; 2009.
- [29] Salim, S. M., and Cheah, S. Wall Y strategy for dealing with wall-bounded turbulent flows. In *Proceedings of the International Multi Conference of Engineers and Computer Scientists*, Vol. 2, pp. 2165-2170, Hong Kong; 2009.
- [30] STAR-CCM+ User Guide, 2011. Version 11.02, CD-Adapco™, USA, 1-12352.
- [31] Frisk, D., and Tegehall, L. Prediction of high-speed planing hull resistance and running attitude. *A Numerical Study using Computational Fluid Dynamics. Master of Science, Department of Shipping and Marine Technology Chalmers University of Technology, Gothenburg, 2015.*
- [32] Gillmer, T. C., and Johnson, B. *Introduction to Naval Architecture (BOOK)*. Airlife Publishing, 1982.
- [33] Ship Resistance and Propulsion Calculators, <https://www.mermaid-consultants.com/ship-wave-making-resistance.html> [Last access in June 19, 2021]
- [34] Slideshare, <https://www.slideshare.net/ABHISHEKKUMAR790/wave-resistance> [Last access in June 19, 2021]
- [35] Xing-Kaeding, Y. Unified approach to ship seakeeping and maneuvering by a RANSE method. *Doctoral Dissertation*, Technische Universität Hamburg, 2006.

- [36] Moukalled, F., Mangani, L., and Darwish, M. *The Finite Volume Method in Computational Fluid Dynamics* (Vol. 113). Berlin, Germany:: Springer; 2016.
- [37] McDonald, P. W. The computation of transonic flow through two-dimensional gas turbine cascades. *ASME 1971 International Gas Turbine Conference and Products Show*. American Society of Mechanical Engineers Digital Collection; 1971, March.
- [38] MacCormack, R., & Paullay, A. Computational efficiency achieved by time splitting of finite difference operators. *10th Aerospace Sciences Meeting* (p. 154), 1972, January.
- [39] Rizzi, A. W., and Inouye, M. Time-split finite-volume method for three-dimensional blunt-body flow. *AIAA Journal*, Vol. 11(11), pp. 1478-1485, 1973.
- [40] Versteeg, H. K., and Malalasekera, W. *An Introduction to Computational Fluid Dynamics: The Finite Volume Method*. Second edition, Pearson Education Limited; 2007.
- [41] Patankar, S. V., and Spalding, D. B. A calculation procedure for heat, mass and momentum transfer in three-dimensional parabolic flows. *International Journal of Heat and Mass Transfer*, Vol. 15(10), pp. 1787-1806, 1972.
- [42] Biswas, G. Solution of Navier–Stokes Equations for Incompressible Flows using MAC and SIMPLE Algorithms. *Computational Fluid Flow and Heat Transfer*, eds K. Muralidhar and T. Sundararajan, Narosa Publishing House, pp. 229-274, 2003.
- [43] Stern, F., Wilson, R. V., Coleman, H. W., & Paterson, E. G. Comprehensive approach to verification and validation of CFD simulations—part 1: methodology and procedures. *J. Fluids Eng.*, Vol. 123(4), pp. 793-802, 2001.
- [44] Wilson, R. V., Stern, F., Coleman, H. W., & Paterson, E. G. Comprehensive approach to verification and validation of CFD simulations—Part 2: Application for RANS simulation of a cargo/container ship. *J. Fluids Eng.*, Vol. 123(4), pp. 803-810, 2001.
- [45] Procedures, I. R. *Uncertainty Analysis in CFD Verification and Validation Methodology and Procedures*; 2008.
- [46] Masuko, A., and Ogiwara, S. Numerical simulation of viscous flow around practical Hull form. *International Conference on Numerical Ship Hydrodynamics*, 5th; 1990.
- [47] Yao, C. B., and Dong, W. C. Method to calculate resistance of high-speed displacement ship taking the effect of dynamic sinkage and trim and fluid viscosity into account. *Journal of Shanghai Jiaotong University (Science)*, Vol. 17(4), pp. 421-426, 2012.

- [48] Kajitani, H., Miyata, H., Ikehata, M., Tanaka, H., Adachi, H., Namimatsu, M., and Ogiwara, S. The summary of the cooperative experiment on Wigley parabolic model in Japan. Tokyo University (Japan); 1983.
- [49] Barros, F.L. Study of kayak hull design on calm water resistance. *Thesis*. Faculdade de Engenharia da Universidade do Porto, Portugal, 2015.
- [50] Tarafder, M. S., and Khalil, G. M. Numerical analysis of free surface flow around a ship in deep water. *Indian Journal of Engineering and Materials Sciences*, Vol. 11, pp. 385-390, 2004.
- [51] Kim, W. J., Van, S. H., & Kim, D. H. Measurement of flows around modern commercial ship models. *Experiments in Fluids*, Vol. 31(5), pp. 567-578, 2001.
- [52] Zou, Lu, and Lars Larsson. Additional data for resistance, sinkage and trim. *Numerical Ship Hydrodynamics*, pp. 255-264. Springer, Dordrecht, 2014.
- [53] Procedures, ITTC–Recommended. Uncertainty analysis in CFD verification and validation methodology and procedures." (2008).
- [54] Takeshi, H., and Hino, T. ITTC Cooperative experiments on a Series 60 model at ship research institute-flow measurements and resistance test. *Proceeding 17th Int. Towing Tank Conference*, Washington DC, pp. 10-13, 1987.
- [55] Karim, M. M., and Naz, N. Computation of hydrodynamic characteristics of ships using CFD. *International Journal of Materials, Mechanics and Manufacturing*, Vol. 5(4), pp. 219-223, 2017.
- [56] Gadd, G E. A method of computing the flow and surface wave pattern around full forms, *Trans. Royal Institute of Naval Architects*, Vol 118, 1976.
- [57] Huang, F. *A practical computational method for steady flow about a ship*. PhD Dissertation, George Mason University; 2013.
- [58] Collatz, G. Mass-stabsuntersuchungen far ein Modell grosser V61ligkeit. Forschungszentrum des Deutschen Schiffbaus, Hamb'irg, Bericht Nr. 28 (1972).
- [59] Kumar, A. Derivation of transport equation for turbulent kinetic energy, k ; 2016. https://www.researchgate.net/publication/349338901_Derivation_of_Turbulence_Kinetic_Energy [Last access on 29 July 2021]
- [60] Tennekes, H., and Lumley, J.L. *A First Course in Turbulence*. The MIT press, 1972.
- [61] Wilcox, D. C. *Turbulence Modeling for CFD*. Third Edition. La Canada, CA: DCW industries; 2006.

- [62] Mansour, N. N., Kim, J., and Moin, P. Reynolds-stress and dissipation-rate budgets in a turbulent channel flow. *Journal of Fluid Mechanics*, Vol. 194, pp. 15-44, 1988.

Appendix A

Derivation of Turbulent Kinetic Energy, k

The derivation of turbulent kinetic energy is deduced following Kumar [18] based on the book by Tennekes and Lumley [60]. The continuity and momentum equations for unsteady, incompressible flow neglecting the body force terms [25]:

$$\frac{\partial u}{\partial x} + \frac{\partial v}{\partial y} + \frac{\partial w}{\partial z} = 0 \quad (\text{A.1})$$

$$\frac{\partial u}{\partial t} + u \frac{\partial u}{\partial x} + v \frac{\partial u}{\partial y} + w \frac{\partial u}{\partial z} = -\frac{1}{\rho} \frac{\partial p}{\partial x} + \nu \left(\frac{\partial^2 u}{\partial x^2} + \frac{\partial^2 u}{\partial y^2} + \frac{\partial^2 u}{\partial z^2} \right) \quad (\text{A.2})$$

$$\frac{\partial v}{\partial t} + u \frac{\partial v}{\partial x} + v \frac{\partial v}{\partial y} + w \frac{\partial v}{\partial z} = -\frac{1}{\rho} \frac{\partial p}{\partial y} + \nu \left(\frac{\partial^2 v}{\partial x^2} + \frac{\partial^2 v}{\partial y^2} + \frac{\partial^2 v}{\partial z^2} \right) \quad (\text{A.3})$$

$$\frac{\partial w}{\partial t} + u \frac{\partial w}{\partial x} + v \frac{\partial w}{\partial y} + w \frac{\partial w}{\partial z} = -\frac{1}{\rho} \frac{\partial p}{\partial z} + \nu \left(\frac{\partial^2 w}{\partial x^2} + \frac{\partial^2 w}{\partial y^2} + \frac{\partial^2 w}{\partial z^2} \right) \quad (\text{A.4})$$

Applying Reynolds decomposition and multiply Equation (A.2) by u'

$$\begin{aligned} u' \frac{\partial}{\partial t} (\bar{u} + u') + u' (\bar{u} + u') \frac{\partial}{\partial x} (\bar{u} + u') + u' (\bar{v} + v') \frac{\partial}{\partial y} (\bar{u} + u') + u' (\bar{w} + w') \frac{\partial}{\partial z} (\bar{u} + u') \\ = -\frac{u'}{\rho} \frac{\partial}{\partial x} (\bar{p} + p') + \nu u' \left[\frac{\partial^2}{\partial x^2} (\bar{u} + u') + \frac{\partial^2}{\partial y^2} (\bar{u} + u') + \frac{\partial^2}{\partial z^2} (\bar{u} + u') \right] \end{aligned} \quad (\text{A.5})$$

Taking the time average,

$$\begin{aligned} \overline{u' \frac{\partial}{\partial t} (\bar{u} + u') + u' (\bar{u} + u') \frac{\partial}{\partial x} (\bar{u} + u') + u' (\bar{v} + v') \frac{\partial}{\partial y} (\bar{u} + u') + u' (\bar{w} + w') \frac{\partial}{\partial z} (\bar{u} + u')} \\ = \overline{-\frac{u'}{\rho} \frac{\partial}{\partial x} (\bar{p} + p') + \nu u' \left[\frac{\partial^2}{\partial x^2} (\bar{u} + u') + \frac{\partial^2}{\partial y^2} (\bar{u} + u') + \frac{\partial^2}{\partial z^2} (\bar{u} + u') \right]} \end{aligned} \quad (\text{A.6})$$

Now simplify the above Equation (A.6) one by one applying some properties given below:

$$\left. \begin{aligned} \overline{\overline{\phi\psi}} &= \overline{\overline{\phi\psi}} \\ \overline{\overline{\phi\phi'}} &= \overline{\overline{\phi\phi'}} = 0 \\ \overline{\overline{\phi + \psi}} &= \overline{\overline{\phi + \psi}} \end{aligned} \right\} \quad (\text{A.7})$$

$$\overline{u' \frac{\partial}{\partial t} (\bar{u} + u')} = \overline{u' \frac{\partial \bar{u}}{\partial t}} + \overline{u' \frac{\partial u'}{\partial t}} = \overline{u' \frac{\partial u'}{\partial t}} \quad (\text{A.8})$$

$$\overline{u'(\bar{u}+u')\frac{\partial}{\partial x}(\bar{u}+u')} = \overline{\bar{u}u'\frac{\partial\bar{u}}{\partial x}} + \overline{u'^2\frac{\partial\bar{u}}{\partial x}} + \overline{\bar{u}u'\frac{\partial u'}{\partial x}} + \overline{u'^2\frac{\partial u'}{\partial x}} = \overline{u'^2\frac{\partial\bar{u}}{\partial x}} + \overline{\bar{u}u'\frac{\partial u'}{\partial x}} + \overline{u'^2\frac{\partial u'}{\partial x}} \quad (\text{A.9})$$

$$\overline{u'(\bar{v}+v')\frac{\partial}{\partial y}(\bar{u}+u')} = \overline{\bar{v}u'\frac{\partial\bar{u}}{\partial y}} + \overline{u'v'\frac{\partial\bar{u}}{\partial y}} + \overline{\bar{v}u'\frac{\partial u'}{\partial y}} + \overline{u'v'\frac{\partial u'}{\partial y}} = \overline{u'v'\frac{\partial\bar{u}}{\partial y}} + \overline{\bar{v}u'\frac{\partial u'}{\partial y}} + \overline{u'v'\frac{\partial u'}{\partial y}} \quad (\text{A.10})$$

$$\overline{u'(\bar{w}+w')\frac{\partial}{\partial z}(\bar{u}+u')} = \overline{\bar{w}u'\frac{\partial\bar{u}}{\partial z}} + \overline{u'w'\frac{\partial\bar{u}}{\partial z}} + \overline{\bar{w}u'\frac{\partial u'}{\partial z}} + \overline{u'w'\frac{\partial u'}{\partial z}} = \overline{u'w'\frac{\partial\bar{u}}{\partial z}} + \overline{\bar{w}u'\frac{\partial u'}{\partial z}} + \overline{u'w'\frac{\partial u'}{\partial z}} \quad (\text{A.11})$$

$$-\frac{u'}{\rho}\frac{\partial}{\partial x}(\bar{p}+p') = -\frac{u'}{\rho}\frac{\partial\bar{p}}{\partial x} - \frac{u'}{\rho}\frac{\partial p'}{\partial x} = -\frac{u'}{\rho}\frac{\partial p'}{\partial x} \quad (\text{A.12})$$

$$\begin{aligned} \overline{\nu u' \left[\frac{\partial^2}{\partial x^2}(\bar{u}+u') + \frac{\partial^2}{\partial y^2}(\bar{u}+u') + \frac{\partial^2}{\partial z^2}(\bar{u}+u') \right]} &= \overline{\nu u' \left[\frac{\partial^2\bar{u}}{\partial x^2} + \frac{\partial^2\bar{u}}{\partial y^2} + \frac{\partial^2\bar{u}}{\partial z^2} \right]} + \overline{\nu u' \left[\frac{\partial^2 u'}{\partial x^2} + \frac{\partial^2 u'}{\partial y^2} + \frac{\partial^2 u'}{\partial z^2} \right]} \\ &= \overline{\nu u' \left[\frac{\partial^2 u'}{\partial x^2} + \frac{\partial^2 u'}{\partial y^2} + \frac{\partial^2 u'}{\partial z^2} \right]} \end{aligned} \quad (\text{A.13})$$

Now rearrange all the term and Equation (A.6) becomes

$$\begin{aligned} \overline{u'\frac{\partial u'}{\partial t}} + \overline{u'^2\frac{\partial\bar{u}}{\partial x}} + \overline{\bar{u}u'\frac{\partial u'}{\partial x}} + \overline{u'^2\frac{\partial u'}{\partial x}} + \overline{u'v'\frac{\partial\bar{u}}{\partial y}} + \overline{\bar{v}u'\frac{\partial u'}{\partial y}} + \overline{u'v'\frac{\partial u'}{\partial y}} + \overline{u'w'\frac{\partial\bar{u}}{\partial z}} + \overline{\bar{w}u'\frac{\partial u'}{\partial z}} + \overline{u'w'\frac{\partial u'}{\partial z}} \\ = -\frac{1}{\rho}\overline{u'\frac{\partial p'}{\partial x}} + \overline{\nu u' \left[\frac{\partial^2 u'}{\partial x^2} + \frac{\partial^2 u'}{\partial y^2} + \frac{\partial^2 u'}{\partial z^2} \right]} \end{aligned} \quad (\text{A.14})$$

Apply the property:

$$u\frac{\partial u}{\partial x} = \frac{1}{2}\frac{\partial u^2}{\partial x} \quad (\text{A.15})$$

And Equation (A.14) becomes

$$\begin{aligned} \frac{1}{2}\frac{\partial\bar{u}^2}{\partial t} + \left(\bar{u}\frac{1}{2}\frac{\partial\bar{u}^2}{\partial x} + \bar{v}\frac{1}{2}\frac{\partial\bar{u}^2}{\partial y} + \bar{w}\frac{1}{2}\frac{\partial\bar{u}^2}{\partial z} \right) + \left(\bar{u}'^2\frac{\partial\bar{u}}{\partial x} + \bar{u}'v'\frac{\partial\bar{u}}{\partial y} + \bar{u}'w'\frac{\partial\bar{u}}{\partial z} \right) + \left(\bar{u}'^2\frac{\partial u'}{\partial x} + \bar{u}'v'\frac{\partial u'}{\partial y} + \bar{u}'w'\frac{\partial u'}{\partial z} \right) \\ = -\frac{1}{\rho}\overline{u'\frac{\partial p'}{\partial x}} + \overline{\nu u' \left[\frac{\partial^2 u'}{\partial x^2} + \frac{\partial^2 u'}{\partial y^2} + \frac{\partial^2 u'}{\partial z^2} \right]} \end{aligned} \quad (\text{A.16})$$

where,

$$\left(\bar{u}'^2\frac{\partial u'}{\partial x} + \bar{u}'v'\frac{\partial u'}{\partial y} + \bar{u}'w'\frac{\partial u'}{\partial z} \right) = \frac{1}{2}\left(\frac{\partial\bar{u}'^3}{\partial x} + \frac{\partial\bar{u}'^2v'}{\partial y} + \frac{\partial\bar{u}'^2w'}{\partial z} \right) - \frac{1}{2}\bar{u}'^2\left(\frac{\partial\bar{u}'}{\partial x} + \frac{\partial\bar{v}'}{\partial y} + \frac{\partial\bar{w}'}{\partial z} \right)$$

$$= \frac{1}{2} \left(\frac{\overline{\partial u'^3}}{\partial x} + \frac{\overline{\partial u'^2 v'}}{\partial y} + \frac{\overline{\partial u'^2 w'}}{\partial z} \right) \quad (\text{A.17})$$

and,

$$\nu u' \left[\frac{\partial^2 u'}{\partial x^2} + \frac{\partial^2 u'}{\partial y^2} + \frac{\partial^2 u'}{\partial z^2} \right] = \nu \left(\frac{\partial^2 \frac{1}{2} \overline{u'^2}}{\partial x^2} + \frac{\partial^2 \frac{1}{2} \overline{u'^2}}{\partial y^2} + \frac{\partial^2 \frac{1}{2} \overline{u'^2}}{\partial z^2} \right) - \nu \left(\left(\frac{\overline{\partial u'}}{\partial x} \right)^2 + \left(\frac{\overline{\partial u'}}{\partial y} \right)^2 + \left(\frac{\overline{\partial u'}}{\partial z} \right)^2 \right) \quad (\text{A.18})$$

So finally Equation (A.16) looks,

$$\begin{aligned} \frac{1}{2} \frac{\partial \overline{u'^2}}{\partial t} + \left(\overline{u} \frac{1}{2} \frac{\partial \overline{u'^2}}{\partial x} + \overline{v} \frac{1}{2} \frac{\partial \overline{u'^2}}{\partial y} + \overline{w} \frac{1}{2} \frac{\partial \overline{u'^2}}{\partial z} \right) &= \left(\overline{u'^2} \frac{\partial \overline{u}}{\partial x} + \overline{u'v'} \frac{\partial \overline{u}}{\partial y} + \overline{u'w'} \frac{\partial \overline{u}}{\partial z} \right) - \frac{1}{2} \left(\frac{\partial \overline{u'^3}}{\partial x} + \frac{\partial \overline{u'^2 v'}}{\partial y} + \frac{\partial \overline{u'^2 w'}}{\partial z} \right) \\ &- \frac{1}{\rho} \overline{u' \frac{\partial p'}{\partial x}} + \nu \left(\frac{\partial^2 \frac{1}{2} \overline{u'^2}}{\partial x^2} + \frac{\partial^2 \frac{1}{2} \overline{u'^2}}{\partial y^2} + \frac{\partial^2 \frac{1}{2} \overline{u'^2}}{\partial z^2} \right) - \nu \left(\left(\frac{\overline{\partial u'}}{\partial x} \right)^2 + \left(\frac{\overline{\partial u'}}{\partial y} \right)^2 + \left(\frac{\overline{\partial u'}}{\partial z} \right)^2 \right) \end{aligned} \quad (\text{A.19})$$

Similarly y and z component become when multiply by v' and w' respectively,

$$\begin{aligned} \frac{1}{2} \frac{\partial \overline{v'^2}}{\partial t} + \left(\overline{u} \frac{1}{2} \frac{\partial \overline{v'^2}}{\partial x} + \overline{v} \frac{1}{2} \frac{\partial \overline{v'^2}}{\partial y} + \overline{w} \frac{1}{2} \frac{\partial \overline{v'^2}}{\partial z} \right) &= \left(\overline{u'v'} \frac{\partial \overline{v}}{\partial x} + \overline{v'^2} \frac{\partial \overline{v}}{\partial y} + \overline{v'w'} \frac{\partial \overline{v}}{\partial z} \right) - \frac{1}{2} \left(\frac{\partial \overline{u'v'^2}}{\partial x} + \frac{\partial \overline{v'^3}}{\partial y} + \frac{\partial \overline{v'^2 w'}}{\partial z} \right) \\ &- \frac{1}{\rho} \overline{v' \frac{\partial p'}{\partial y}} + \nu \left(\frac{\partial^2 \frac{1}{2} \overline{v'^2}}{\partial x^2} + \frac{\partial^2 \frac{1}{2} \overline{v'^2}}{\partial y^2} + \frac{\partial^2 \frac{1}{2} \overline{v'^2}}{\partial z^2} \right) - \nu \left(\left(\frac{\overline{\partial v'}}{\partial x} \right)^2 + \left(\frac{\overline{\partial v'}}{\partial y} \right)^2 + \left(\frac{\overline{\partial v'}}{\partial z} \right)^2 \right) \end{aligned} \quad (\text{A.20})$$

$$\begin{aligned} \frac{1}{2} \frac{\partial \overline{w'^2}}{\partial t} + \left(\overline{u} \frac{1}{2} \frac{\partial \overline{w'^2}}{\partial x} + \overline{v} \frac{1}{2} \frac{\partial \overline{w'^2}}{\partial y} + \overline{w} \frac{1}{2} \frac{\partial \overline{w'^2}}{\partial z} \right) &= \left(\overline{u'w'} \frac{\partial \overline{w}}{\partial x} + \overline{v'w'} \frac{\partial \overline{w}}{\partial y} + \overline{w'^2} \frac{\partial \overline{w}}{\partial z} \right) - \frac{1}{2} \left(\frac{\partial \overline{u'w'^2}}{\partial x} + \frac{\partial \overline{v'w'^2}}{\partial y} + \frac{\partial \overline{w'^3}}{\partial z} \right) \\ &- \frac{1}{\rho} \overline{w' \frac{\partial p'}{\partial z}} + \nu \left(\frac{\partial^2 \frac{1}{2} \overline{w'^2}}{\partial x^2} + \frac{\partial^2 \frac{1}{2} \overline{w'^2}}{\partial y^2} + \frac{\partial^2 \frac{1}{2} \overline{w'^2}}{\partial z^2} \right) - \nu \left(\left(\frac{\overline{\partial w'}}{\partial x} \right)^2 + \left(\frac{\overline{\partial w'}}{\partial y} \right)^2 + \left(\frac{\overline{\partial w'}}{\partial z} \right)^2 \right) \end{aligned} \quad (\text{A.21})$$

Adding Equations (A.19), (A.20), and (A.21) and using the definition of turbulent kinetic energy:

$$k = \frac{1}{2} \left(\overline{u'^2} + \overline{v'^2} + \overline{w'^2} \right) \quad (\text{A.22})$$

The equation for turbulent kinetic energy stands:

$$\begin{aligned}
 & \frac{\partial k}{\partial t} + \bar{u} \frac{\partial k}{\partial x} + \bar{v} \frac{\partial k}{\partial y} + \bar{w} \frac{\partial k}{\partial z} \\
 &= - \left(\overline{u'^2 \frac{\partial \bar{u}}{\partial x}} + \overline{u'v' \frac{\partial \bar{u}}{\partial y}} + \overline{u'w' \frac{\partial \bar{u}}{\partial z}} + \overline{u'v' \frac{\partial \bar{v}}{\partial x}} + \overline{v'^2 \frac{\partial \bar{v}}{\partial y}} + \overline{v'w' \frac{\partial \bar{v}}{\partial z}} + \overline{u'w' \frac{\partial \bar{w}}{\partial x}} + \overline{v'w' \frac{\partial \bar{w}}{\partial y}} + \overline{w'^2 \frac{\partial \bar{w}}{\partial z}} \right) \\
 & - \frac{1}{\rho} \left(\overline{u' \frac{\partial p'}{\partial x}} + \overline{v' \frac{\partial p'}{\partial y}} + \overline{w' \frac{\partial p'}{\partial z}} \right) \\
 & - \frac{1}{2} \left(\overline{\frac{\partial u'^3}{\partial x}} + \overline{\frac{\partial u'^2 v'}{\partial y}} + \overline{\frac{\partial u'^2 w'}{\partial z}} + \overline{\frac{\partial u' v'^2}{\partial x}} + \overline{\frac{\partial v'^3}{\partial y}} + \overline{\frac{\partial v'^2 w'}{\partial z}} + \overline{\frac{\partial u' w'^2}{\partial x}} + \overline{\frac{\partial v' w'^2}{\partial y}} + \overline{\frac{\partial w'^3}{\partial z}} \right) \\
 & + \nu \left(\overline{\frac{\partial^2 \frac{1}{2} u'^2}{\partial x^2}} + \overline{\frac{\partial^2 \frac{1}{2} u'^2}{\partial y^2}} + \overline{\frac{\partial^2 \frac{1}{2} u'^2}{\partial z^2}} + \overline{\frac{\partial^2 \frac{1}{2} v'^2}{\partial x^2}} + \overline{\frac{\partial^2 \frac{1}{2} v'^2}{\partial y^2}} + \overline{\frac{\partial^2 \frac{1}{2} v'^2}{\partial z^2}} + \overline{\frac{\partial^2 \frac{1}{2} w'^2}{\partial x^2}} + \overline{\frac{\partial^2 \frac{1}{2} w'^2}{\partial y^2}} + \overline{\frac{\partial^2 \frac{1}{2} w'^2}{\partial z^2}} \right) \\
 & - \nu \left[\left(\frac{\partial \bar{u}'}{\partial x} \right)^2 + \left(\frac{\partial \bar{u}'}{\partial y} \right)^2 + \left(\frac{\partial \bar{u}'}{\partial z} \right)^2 + \left(\frac{\partial \bar{v}'}{\partial x} \right)^2 + \left(\frac{\partial \bar{v}'}{\partial y} \right)^2 + \left(\frac{\partial \bar{v}'}{\partial z} \right)^2 + \left(\frac{\partial \bar{w}'}{\partial x} \right)^2 + \left(\frac{\partial \bar{w}'}{\partial y} \right)^2 + \left(\frac{\partial \bar{w}'}{\partial z} \right)^2 \right] \tag{A.23}
 \end{aligned}$$

In the above Equation, for the left hand side, first term is **rate of change of k** and second term is called **transport of k by convection**. On the other part, for the right hand side, first term is **production of k by interaction of Reynolds stress and mean flow**, second term is **transport due to pressure**, third term is **transport due to viscous stress**, and the last term is **called rate of dissipation of k (ε)**.

Turbulent Transport and Pressure Diffusion

Turbulent transport of scalar quantities in a turbulent flow is that of diffusion [61] can be written,

$$\overline{-u'\phi'} = \nu_t \frac{\partial \phi}{\partial x} \quad \overline{-v'\phi'} = \nu_t \frac{\partial \phi}{\partial y} \quad \overline{-w'\phi'} = \nu_t \frac{\partial \phi}{\partial z} \tag{A.24}$$

Unfortunately, there is no corresponding straightforward analog for pressure-diffusion term. In the absence of definitive experimental data, the pressure-diffusion term has generally been grouped with the turbulent-transport term, and the sum assumed to behave as a gradient transport process. Masour, Kim and Moin [62] indicate that the term is quite small for simple flow. Thus, it is assumed that,

$$\begin{aligned}
 & \frac{\partial}{\partial x} \left[\frac{1}{2} (\overline{u'^3} + \overline{u'v'^2} + \overline{u'w'^2}) + \frac{1}{\rho} \overline{p'u'} \right] + \frac{\partial}{\partial y} \left[\frac{1}{2} (\overline{v'^3} + \overline{v'u'^2} + \overline{v'w'^2}) + \frac{1}{\rho} \overline{p'v'} \right] + \frac{\partial}{\partial z} \left[\frac{1}{2} (\overline{w'^3} + \overline{w'u'^2} + \overline{w'v'^2}) + \frac{1}{\rho} \overline{p'w'} \right] \\
 &= -\frac{\nu_t}{\sigma_k} \left(\frac{\partial^2 k}{\partial x^2} + \frac{\partial^2 k}{\partial y^2} + \frac{\partial^2 k}{\partial z^2} \right) \tag{A.25}
 \end{aligned}$$

Where σ_k (*turbulent Prandtl number*) is a closure coefficient.

The right hand side of Equation (A.23) can be more simplified. For doing that start with the last term of right hand side of Equation (A.23) which is actually the dissipation rate of turbulent kinetic energy.

$$\begin{aligned}
 & \nu \left[\left(\frac{\partial \overline{u'}}{\partial x} \right)^2 + \left(\frac{\partial \overline{u'}}{\partial y} \right)^2 + \left(\frac{\partial \overline{u'}}{\partial z} \right)^2 + \left(\frac{\partial \overline{v'}}{\partial x} \right)^2 + \left(\frac{\partial \overline{v'}}{\partial y} \right)^2 + \left(\frac{\partial \overline{v'}}{\partial z} \right)^2 + \left(\frac{\partial \overline{w'}}{\partial x} \right)^2 + \left(\frac{\partial \overline{w'}}{\partial y} \right)^2 + \left(\frac{\partial \overline{w'}}{\partial z} \right)^2 \right] = \varepsilon \tag{A.26} \\
 & \nu \left(\frac{\partial^2 \frac{1}{2} \overline{u'^2}}{\partial x^2} + \frac{\partial^2 \frac{1}{2} \overline{u'^2}}{\partial y^2} + \frac{\partial^2 \frac{1}{2} \overline{u'^2}}{\partial z^2} + \frac{\partial^2 \frac{1}{2} \overline{v'^2}}{\partial x^2} + \frac{\partial^2 \frac{1}{2} \overline{v'^2}}{\partial y^2} + \frac{\partial^2 \frac{1}{2} \overline{v'^2}}{\partial z^2} + \frac{\partial^2 \frac{1}{2} \overline{w'^2}}{\partial x^2} + \frac{\partial^2 \frac{1}{2} \overline{w'^2}}{\partial y^2} + \frac{\partial^2 \frac{1}{2} \overline{w'^2}}{\partial z^2} \right) \\
 &= \nu \left(\frac{\partial^2 k}{\partial x^2} + \frac{\partial^2 k}{\partial y^2} + \frac{\partial^2 k}{\partial z^2} \right) \tag{A.27}
 \end{aligned}$$

$$\begin{aligned}
 & \frac{1}{2} \left(\frac{\partial \overline{u'^3}}{\partial x} + \frac{\partial \overline{u'v'^2}}{\partial y} + \frac{\partial \overline{u'w'^2}}{\partial z} + \frac{\partial \overline{v'u'^2}}{\partial x} + \frac{\partial \overline{v'^3}}{\partial y} + \frac{\partial \overline{v'^2 w'}}{\partial z} + \frac{\partial \overline{u'w'^2}}{\partial x} + \frac{\partial \overline{v'w'^2}}{\partial y} + \frac{\partial \overline{w'^3}}{\partial z} \right) \\
 &= \frac{\partial}{\partial x} \left[\frac{1}{2} (\overline{u'^3} + \overline{u'v'^2} + \overline{u'w'^2}) \right] + \frac{\partial}{\partial y} \left[\frac{1}{2} (\overline{v'^3} + \overline{v'u'^2} + \overline{v'w'^2}) \right] + \frac{\partial}{\partial z} \left[\frac{1}{2} (\overline{w'^3} + \overline{w'u'^2} + \overline{w'v'^2}) \right] \\
 & - \frac{1}{\rho} \left(\overline{u' \frac{\partial p'}{\partial x}} + \overline{v' \frac{\partial p'}{\partial y}} + \overline{w' \frac{\partial p'}{\partial z}} \right) = -\frac{1}{\rho} \left[\left(\frac{\partial \overline{p'u'}}{\partial x} + \frac{\partial \overline{p'v'}}{\partial y} + \frac{\partial \overline{p'w'}}{\partial z} \right) - p' \left(\frac{\partial \overline{u'}}{\partial x} + \frac{\partial \overline{v'}}{\partial y} + \frac{\partial \overline{w'}}{\partial z} \right) \right] \\
 &= -\frac{1}{\rho} \left[\left(\frac{\partial \overline{p'u'}}{\partial x} + \frac{\partial \overline{p'v'}}{\partial y} + \frac{\partial \overline{p'w'}}{\partial z} \right) \right] \tag{A.28}
 \end{aligned}$$

$$\begin{aligned}
 & \left(\overline{u'^2} \frac{\partial \overline{u}}{\partial x} + \overline{u'v'} \frac{\partial \overline{u}}{\partial y} + \overline{u'w'} \frac{\partial \overline{u}}{\partial z} + \overline{u'v'} \frac{\partial \overline{v}}{\partial x} + \overline{v'^2} \frac{\partial \overline{v}}{\partial y} + \overline{v'w'} \frac{\partial \overline{v}}{\partial z} + \overline{u'w'} \frac{\partial \overline{w}}{\partial x} + \overline{v'w'} \frac{\partial \overline{w}}{\partial y} + \overline{w'^2} \frac{\partial \overline{w}}{\partial z} \right) \\
 &= \left[\left(2\nu_t \frac{\partial \overline{u}}{\partial x} - \frac{2}{3} k \right) \frac{\partial \overline{u}}{\partial x} + \nu_t \left(\frac{\partial \overline{u}}{\partial y} + \frac{\partial \overline{v}}{\partial x} \right) \frac{\partial \overline{u}}{\partial y} + \nu_t \left(\frac{\partial \overline{u}}{\partial z} + \frac{\partial \overline{w}}{\partial x} \right) \frac{\partial \overline{u}}{\partial z} \right] \\
 &+ \left[\nu_t \left(\frac{\partial \overline{u}}{\partial y} + \frac{\partial \overline{v}}{\partial x} \right) \frac{\partial \overline{v}}{\partial x} + \left(2\nu_t \frac{\partial \overline{v}}{\partial y} - \frac{2}{3} k \right) \frac{\partial \overline{v}}{\partial y} + \nu_t \left(\frac{\partial \overline{v}}{\partial z} + \frac{\partial \overline{w}}{\partial y} \right) \frac{\partial \overline{v}}{\partial z} \right]
 \end{aligned}$$

$$\begin{aligned}
 & + \left[\nu_t \left(\frac{\partial \bar{u}}{\partial z} + \frac{\partial \bar{w}}{\partial x} \right) \frac{\partial \bar{w}}{\partial x} + \nu_t \left(\frac{\partial \bar{w}}{\partial y} + \frac{\partial \bar{v}}{\partial z} \right) \frac{\partial \bar{v}}{\partial y} + \left(2\nu_t \frac{\partial \bar{w}}{\partial z} - \frac{2}{3}k \right) \frac{\partial \bar{w}}{\partial z} \right] \\
 = & 2\nu_t \left[\left(\frac{\partial \bar{u}}{\partial x} \right)^2 + \left(\frac{\partial \bar{v}}{\partial y} \right)^2 + \left(\frac{\partial \bar{w}}{\partial z} \right)^2 \right] + \nu_t \left[\left(\frac{\partial \bar{u}}{\partial y} \right)^2 + 2 \frac{\partial \bar{u}}{\partial y} \frac{\partial \bar{v}}{\partial x} + \left(\frac{\partial \bar{v}}{\partial x} \right)^2 \right] + \nu_t \left[\left(\frac{\partial \bar{u}}{\partial z} \right)^2 + 2 \frac{\partial \bar{u}}{\partial z} \frac{\partial \bar{w}}{\partial x} + \left(\frac{\partial \bar{w}}{\partial x} \right)^2 \right] \\
 & + \nu_t \left[\left(\frac{\partial \bar{v}}{\partial z} \right)^2 + 2 \frac{\partial \bar{v}}{\partial z} \frac{\partial \bar{w}}{\partial y} + \left(\frac{\partial \bar{w}}{\partial y} \right)^2 \right] - \frac{2}{3}k \left(\frac{\partial \bar{u}}{\partial x} + \frac{\partial \bar{v}}{\partial y} + \frac{\partial \bar{w}}{\partial z} \right) \\
 = & 2\nu_t \left[\left(\frac{\partial \bar{u}}{\partial x} \right)^2 + \left(\frac{\partial \bar{v}}{\partial y} \right)^2 + \left(\frac{\partial \bar{w}}{\partial z} \right)^2 \right] + \nu_t \left[\left(\frac{\partial \bar{u}}{\partial y} + \frac{\partial \bar{v}}{\partial x} \right)^2 + \left(\frac{\partial \bar{v}}{\partial z} + \frac{\partial \bar{w}}{\partial y} \right)^2 + \left(\frac{\partial \bar{w}}{\partial x} + \frac{\partial \bar{u}}{\partial z} \right)^2 \right] = Q \quad (\text{A.29})
 \end{aligned}$$

Rearranging all the terms and putting into Equation (A.23), the k Equation becomes,

$$\begin{aligned}
 \frac{\partial k}{\partial t} + \bar{u} \frac{\partial k}{\partial x} + \bar{v} \frac{\partial k}{\partial y} + \bar{w} \frac{\partial k}{\partial z} = & \nu \left(\frac{\partial^2 k}{\partial x^2} + \frac{\partial^2 k}{\partial y^2} + \frac{\partial^2 k}{\partial z^2} \right) - \frac{\partial}{\partial x} \left[\frac{1}{2} (\overline{u'^3} + \overline{u'v'^2} + \overline{u'w'^2}) + \frac{1}{\rho} \overline{p'u'} \right] \\
 & - \frac{\partial}{\partial y} \left[-\frac{1}{2} (\overline{v'^3} + \overline{v'u'^2} + \overline{v'w'^2}) + \frac{1}{\rho} \overline{p'v'} \right] - \frac{\partial}{\partial z} \left[\frac{1}{2} (\overline{w'^3} + \overline{w'u'^2} + \overline{w'v'^2}) + \frac{1}{\rho} \overline{p'w'} \right] + Q - \varepsilon \quad (\text{A.30})
 \end{aligned}$$

$$\begin{aligned}
 \frac{\partial k}{\partial t} + \bar{u} \frac{\partial k}{\partial x} + \bar{v} \frac{\partial k}{\partial y} + \bar{w} \frac{\partial k}{\partial z} = & \nu \left(\frac{\partial^2 k}{\partial x^2} + \frac{\partial^2 k}{\partial y^2} + \frac{\partial^2 k}{\partial z^2} \right) + \frac{\nu_t}{\sigma_k} \left(\frac{\partial^2 k}{\partial x^2} + \frac{\partial^2 k}{\partial y^2} + \frac{\partial^2 k}{\partial z^2} \right) + Q - \varepsilon \\
 \frac{\partial k}{\partial t} + \bar{u} \frac{\partial k}{\partial x} + \bar{v} \frac{\partial k}{\partial y} + \bar{w} \frac{\partial k}{\partial z} = & \frac{\partial}{\partial x} \left[\left(\nu + \frac{\nu_t}{\sigma_k} \right) \frac{\partial k}{\partial x} \right] + \frac{\partial}{\partial y} \left[\left(\nu + \frac{\nu_t}{\sigma_k} \right) \frac{\partial k}{\partial y} \right] + \frac{\partial}{\partial z} \left[\left(\nu + \frac{\nu_t}{\sigma_k} \right) \frac{\partial k}{\partial z} \right] + Q - \varepsilon \quad (\text{A.31})
 \end{aligned}$$

Equation (A.31) is the final expression for the turbulent kinetic energy, k .

Appendix B

Numerical Scheme to Predict Body Motion

The forces and moments acting on the free floating body are obtained from the flow around the body; at the same time, the fluid flow is influenced by the motion of the body. Therefore, the problem has to be solved in a coupled manner, considering the interaction of body and flow. Since the fluid flow has to be solved in an iterative manner due to its nonlinearity, the determination of the body motion can also be implemented in a similar way to take advantage of the iterative feature of the fluid solver.

Translational Motion

The governing equation [30] for the translation of the center of mass is given by

$$\frac{d\mathbf{V}}{dt} = \frac{\mathbf{F}}{m} \quad (\text{B.1})$$

After integrating the forces around the body surfaces, the velocity at the new time step $n + 1$ is predicted using the velocity at the previous time step n first, then corrected for later iterations by applying the trapezoidal rule to compute the derivative [35]:

$$\begin{aligned} \mathbf{V}_{n+1}^{i+1} &= \mathbf{V}_n + \frac{\mathbf{F}_n + \mathbf{F}_{n+1}^{i+1}}{2m} \Delta t \\ &= \underbrace{\mathbf{V}_n + \frac{\mathbf{F}_n}{m} \Delta t}_{\text{predictor}} + \underbrace{\frac{\mathbf{F}_{n+1}^{i+1} - \mathbf{F}_n}{2m} \Delta t}_{\text{corrector}} \end{aligned} \quad (\text{B.2})$$

When the velocities of the body have been obtained, the position of the body can be also determined in a similar way:

$$\begin{aligned} \mathbf{r}_{n+1}^{i+1} &= \mathbf{r}_n + \left(\mathbf{V}_n + \mathbf{V}_{n+1}^{i+1} \right) \frac{\Delta t}{2} \\ &= \underbrace{\mathbf{r}_n + \mathbf{V}_n \Delta t}_{\text{predictor}} + \underbrace{\frac{\mathbf{V}_{n+1}^{i+1} - \mathbf{V}_n}{2} \Delta t}_{\text{corrector}} \end{aligned} \quad (\text{B.3})$$

The incremental displacement of the rigid body can be computed:

$$\Delta \mathbf{r}_{n+1}^{i+1} = \mathbf{r}_{n+1}^{i+1} - \mathbf{r}_{n+1}^i \quad (\text{B.4})$$

Rotational Motion

The equation of rotation of the body is formulated in the Body Local Coordinate System with the origin in the center of mass of the body:

$$\mathbf{I} \frac{d\vec{\omega}}{dt} + \vec{\omega} \times \mathbf{I} \vec{\omega} = \mathbf{M} \quad (\text{B.5})$$

The discretized form [35] of Equation (B.5) reads

$$\begin{aligned} \mathbf{I}_{n+1}^i \cdot \boldsymbol{\omega}_{n+1}^{i+1} &= \mathbf{I}_n \cdot \boldsymbol{\omega}_n + (\mathbf{M}_n + \mathbf{M}_{n+1}^{i+1}) \frac{\Delta t}{2} \\ &\quad - \left(\boldsymbol{\omega}_n \times \mathbf{I}_n \cdot \boldsymbol{\omega}_n + \boldsymbol{\omega}_{n+1}^i \times \mathbf{I}_{n+1}^i \cdot \boldsymbol{\omega}_{n+1}^i \right) \frac{\Delta t}{2} \\ &= \underbrace{\mathbf{I}_n \cdot \boldsymbol{\omega}_n + (\mathbf{M}_n - \boldsymbol{\omega}_n \times \mathbf{I}_n \cdot \boldsymbol{\omega}_n) \Delta t}_{\text{predictor}} \\ &\quad + \underbrace{\frac{\mathbf{M}_{n+1}^{i+1} - \mathbf{M}_n}{2} \Delta t - \left(\boldsymbol{\omega}_{n+1}^i \times \mathbf{I}_{n+1}^i \cdot \boldsymbol{\omega}_{n+1}^i - \boldsymbol{\omega}_n \times \mathbf{I}_n \cdot \boldsymbol{\omega}_n \right) \frac{\Delta t}{2}}_{\text{corrector}} \end{aligned} \quad (\text{B.6})$$

\mathbf{I}_{n+1}^i is computed as follows,

$$\mathbf{I}_{n+1}^i = \mathbf{T}_{n+1}^i \cdot \mathbf{I} \cdot (\mathbf{T}_{n+1}^i)^{-1} \quad (\text{B.7})$$

The orientation of the body is determined by the tensor \mathbf{T} . The easiest approach to obtain the new orientation of the unit vector \mathbf{x}_{n+1}^i is

$$\mathbf{x}_{n+1}^i = \mathbf{x}_n + \frac{\Delta t}{2} (\boldsymbol{\omega}_n + \boldsymbol{\omega}_{n+1}^i) \times \mathbf{x}_n \quad (\text{B.8})$$

Appendix C

Residual Convergence

The satisfaction degree of the discretized equation in each control volume cell is represented by the residual. The residual plot is a monitor plot that is automatically created from the active residual monitors on semi-log axes when iterating starts. By default, all active residuals are displayed in the residual plot. Residual monitor keeps a record for each of the transport equations solved in the continua within the simulation. As the solution is time-dependent, the convergence occurs within each time-step. The continuity, momentum equations, turbulent quantity consisting in the residual are being converged when the difference between current and previous iteration results decrease. Following that the equation results are reaching values that are changing less and less.

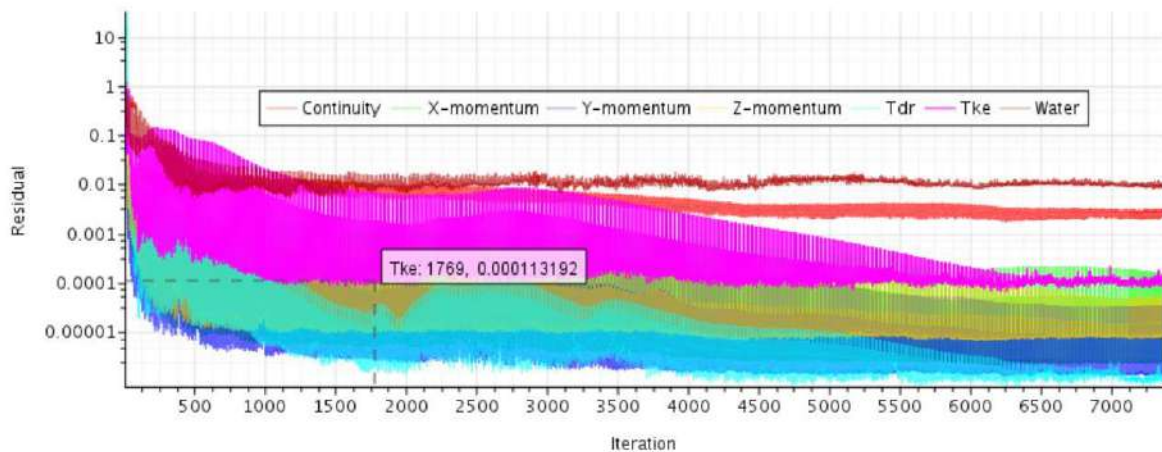


Fig. C.1: Residual convergence of Wigley hull

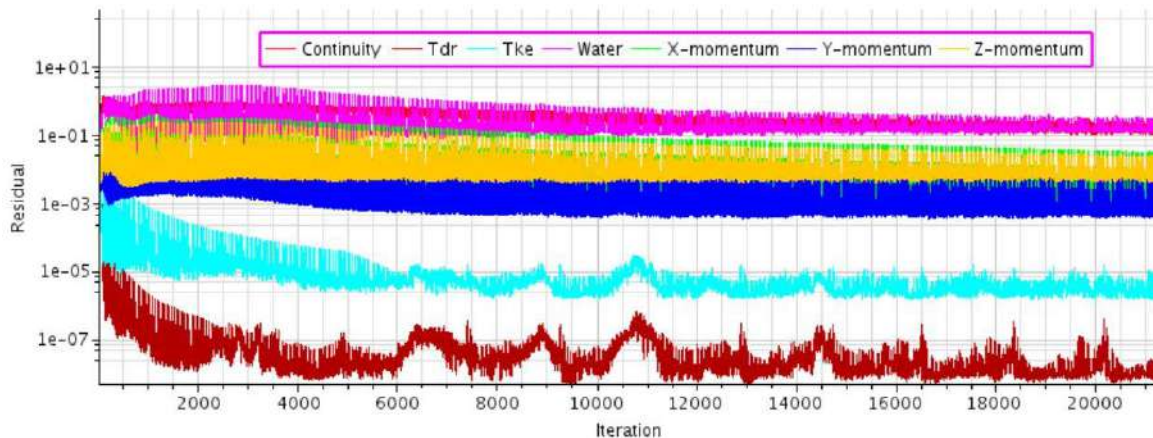


Fig. C.2: Residual convergence of KCS hull

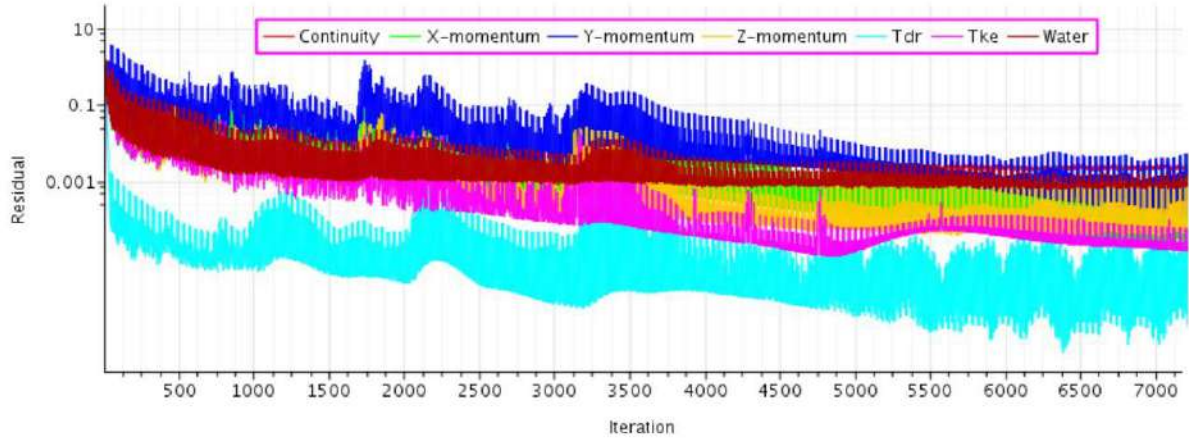


Fig. C.3: Residual convergence of Series 60 hull

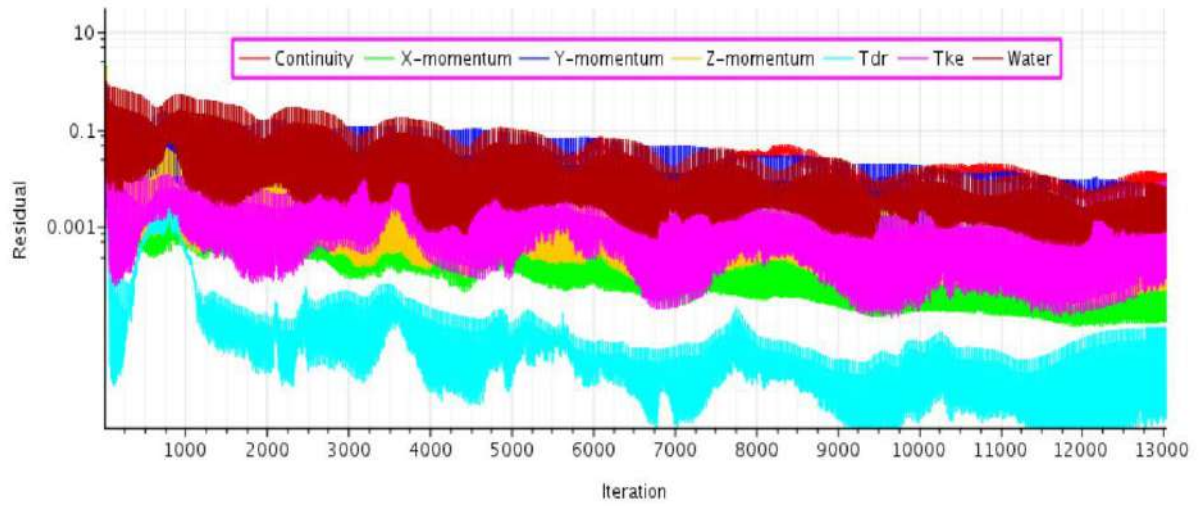


Fig. C.4: Residual convergence of HSVA tanker hull

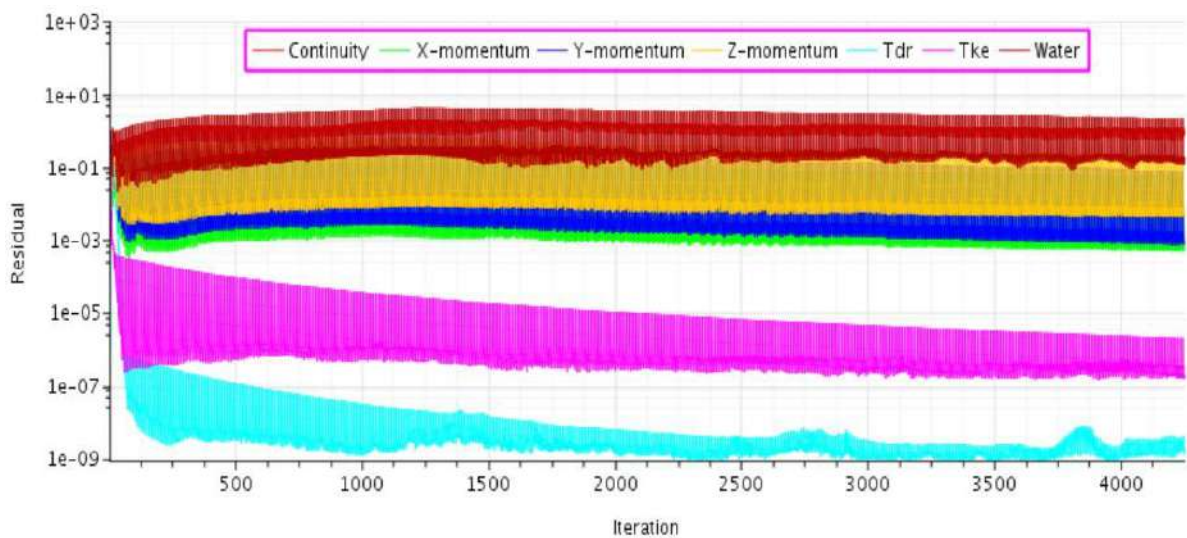


Fig. C.5: Residual convergence of Wigley catamaran hull

Appendix D

Time History of Resistance

Figure D.1 to D.4 shows how the resistance on hull converged towards the steady state solution. Among the resistance components, the frictional resistance becomes calm to an approximately constant value very quickly while the residual resistance fluctuates around the steady state value with reducing amplitude.

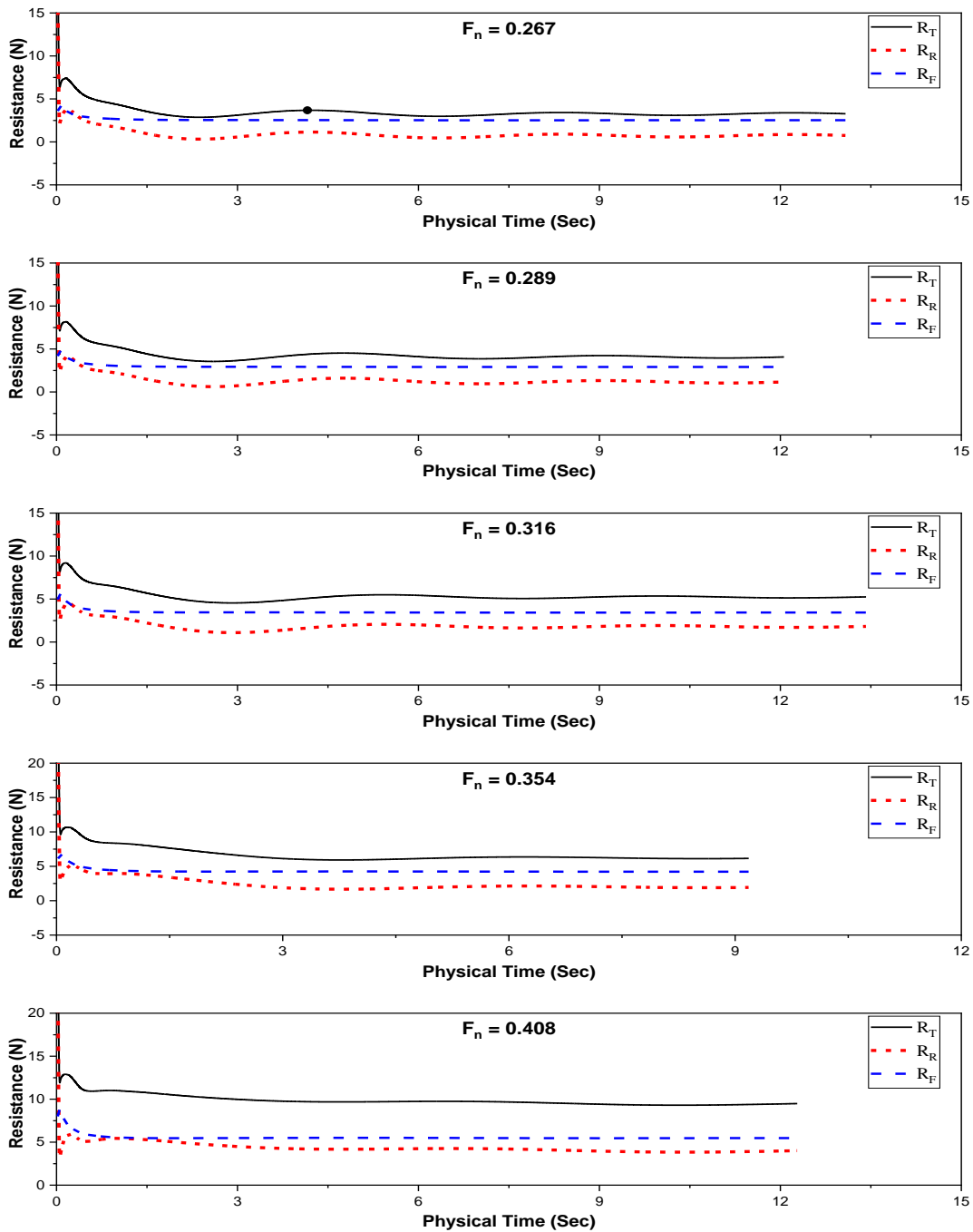


Fig. D.1: Time history of Total, Residual and Frictional Resistance of Wigley hull

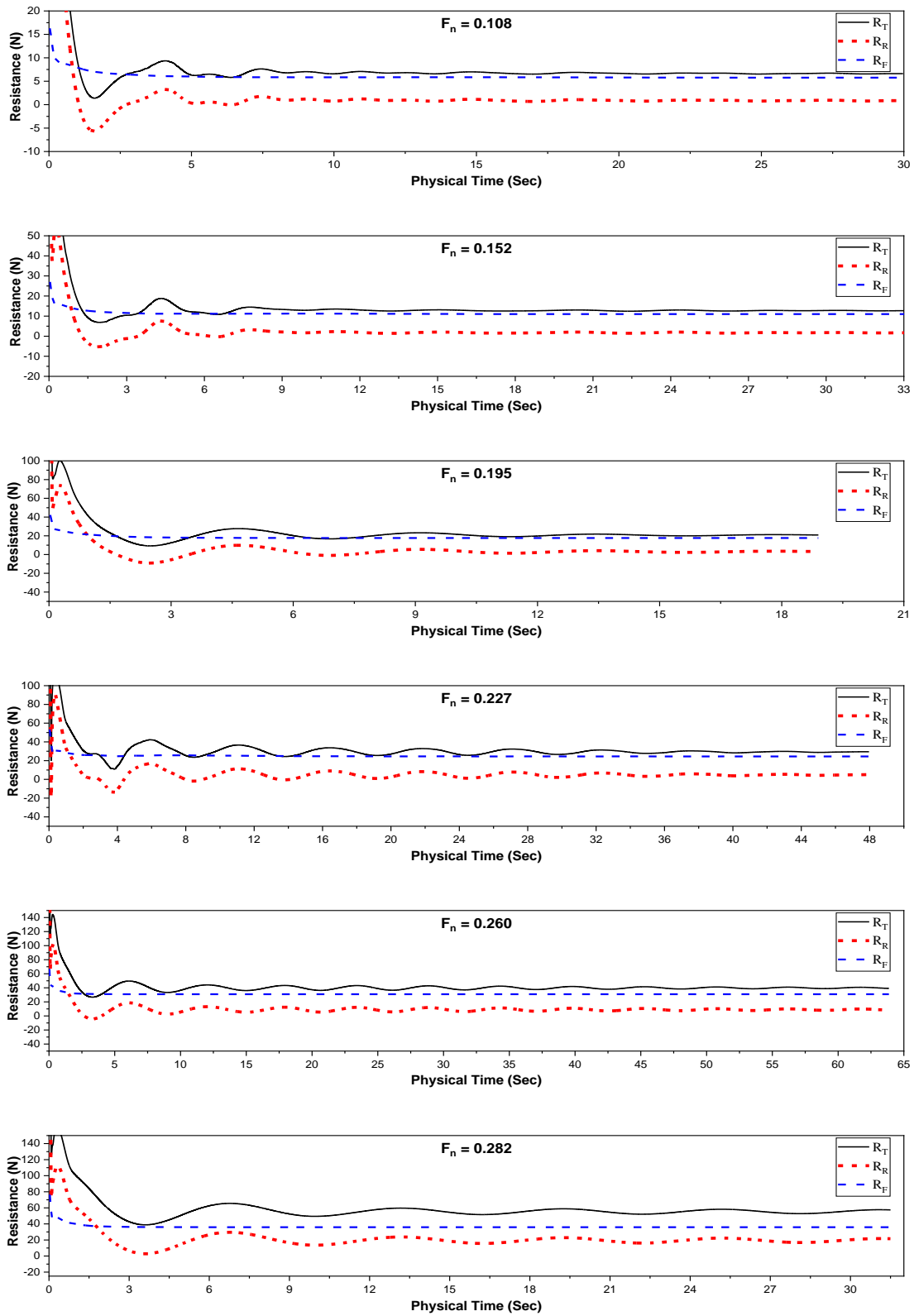


Fig. D.2: Time history of Total, Residual and Frictional Resistance of KCS hull

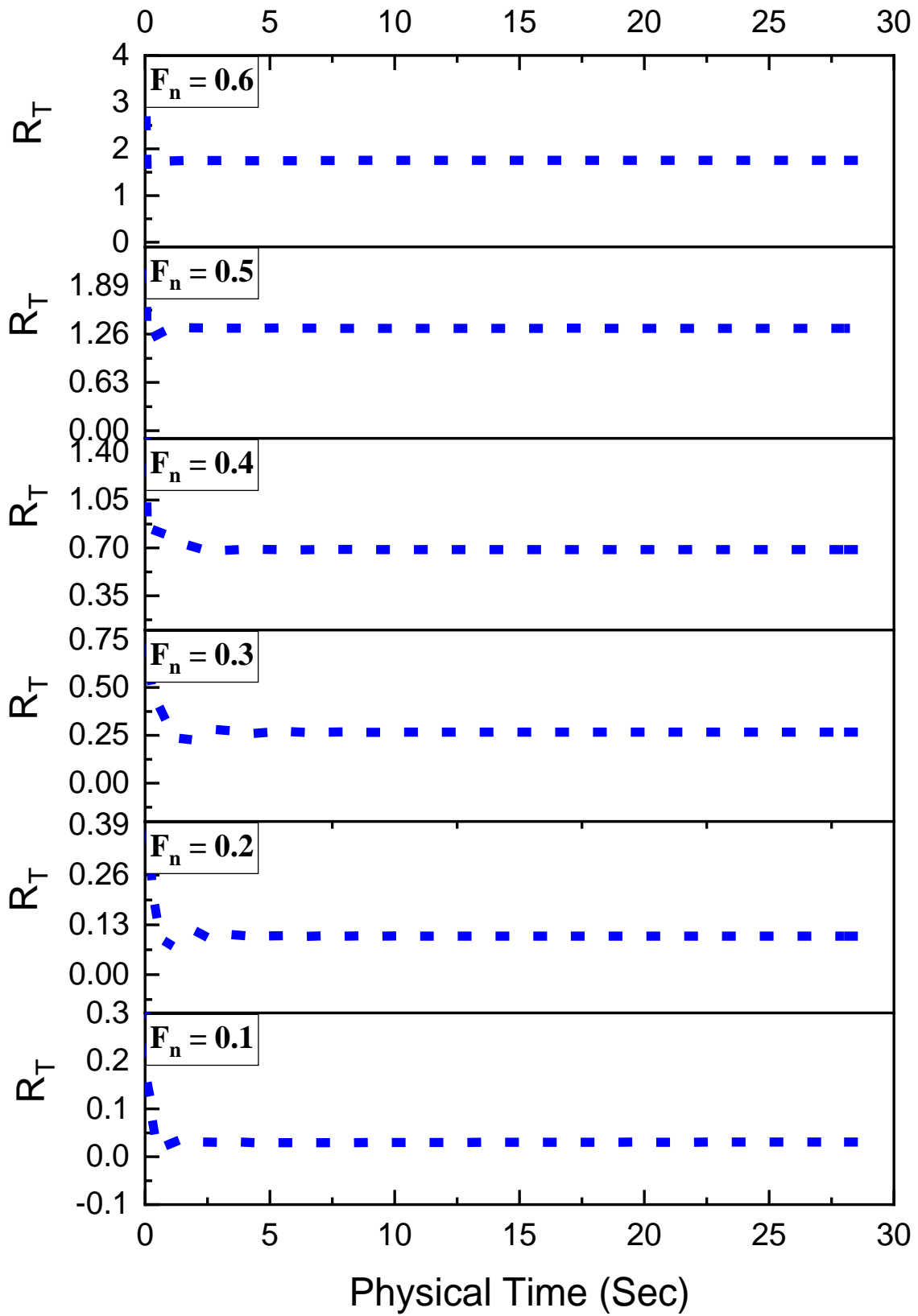


Fig. D.3: Time history of Total Resistance of Series 60 hull

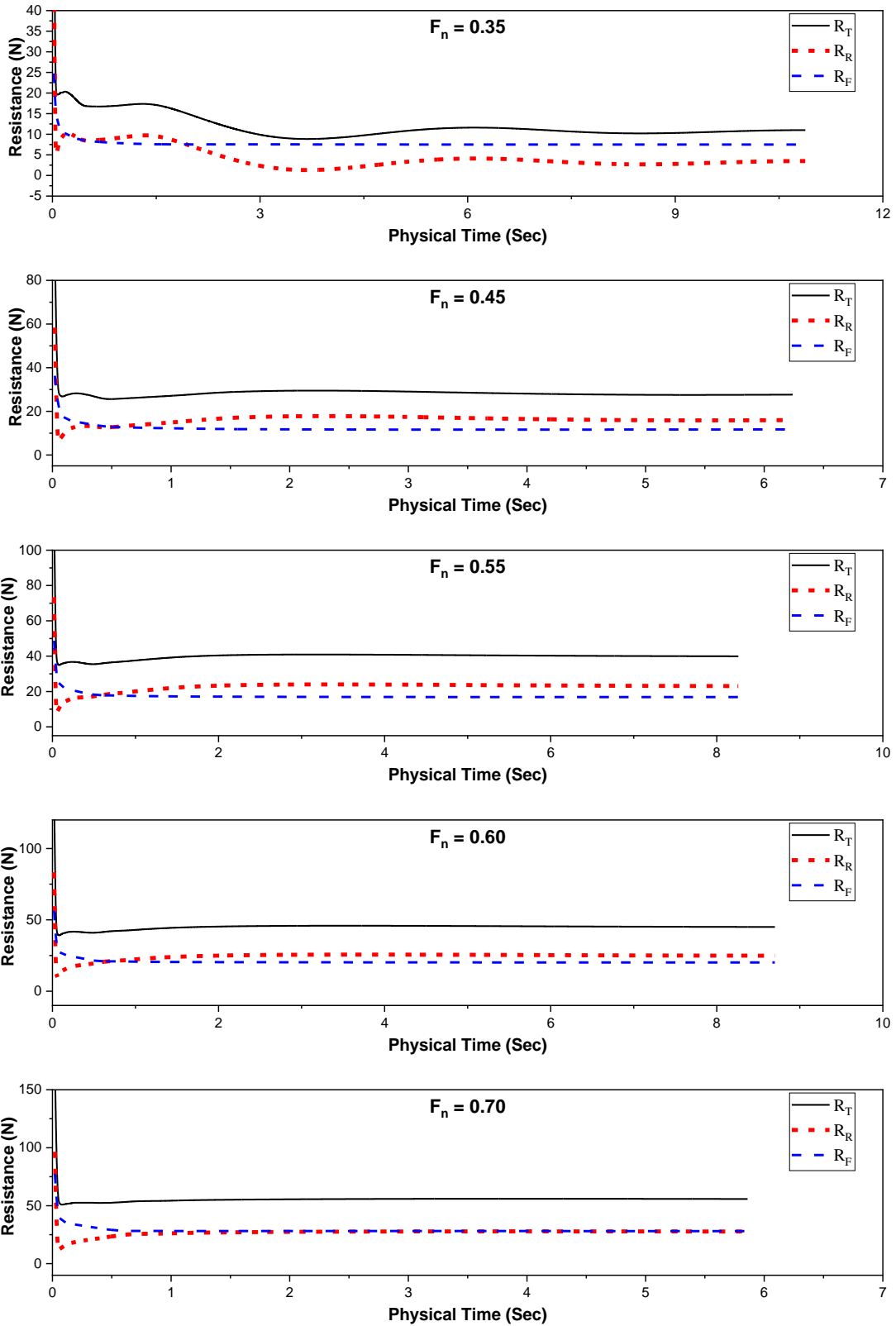


Fig. D.4: Time history of Total, Residual and Frictional Resistance of Catamaran hull

Appendix E

Outline of Simulation Setup

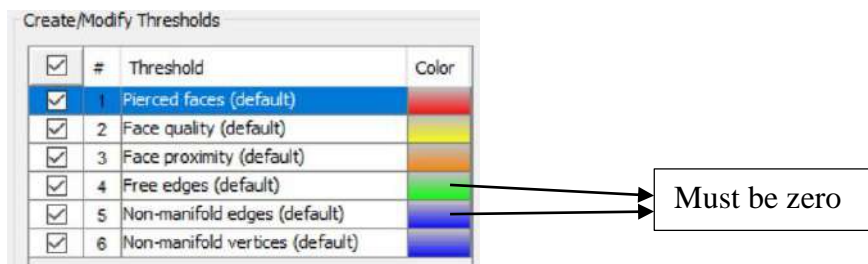
Creating a new Simulation

- Create a File > Serial > Ok

Importing the file/geometry

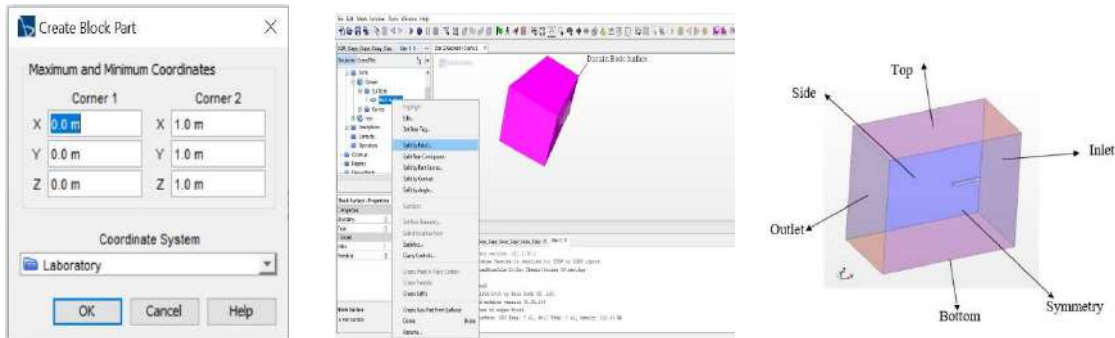
- File > Import > Import Surface mesh > Choose iges/parasolid/x_t extension file
- Make sure there are no free edges and non-manifold edges. This is done by expanding the part import located in the left side tree bar.

Geometry > Part > Right click on imported part > Repair Surface > Manage > Ok



Creating the Computational Domain and defined each boundary surface

- Geometry > Part > New Shape Part > Block > Give the three coordinate values of corner 1 & 2 (Make sure domain only includes the half body of the hull)
- Name the block as Domain. Expanded the domain > Surface > Block Surface > Split by Patch > Define the six surfaces with preferable name: Inlet, Outlet, Top, Bottom, Side, & Symmetry

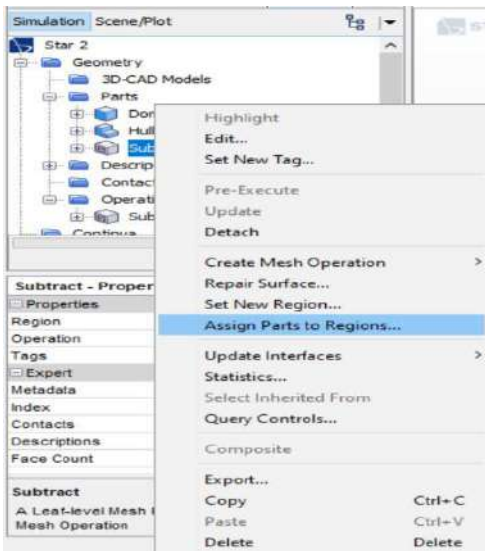


Subtracting the hull body from the domain

- Geometry > Operation > New > Boolean > Subtract
- From opening window select Domain and Hull as input parts and Domain as Target part and activate Execute operation upon creation then Ok.

Assigning Parts to Region

- Right clicke on the Subtract > Assign parts to Region



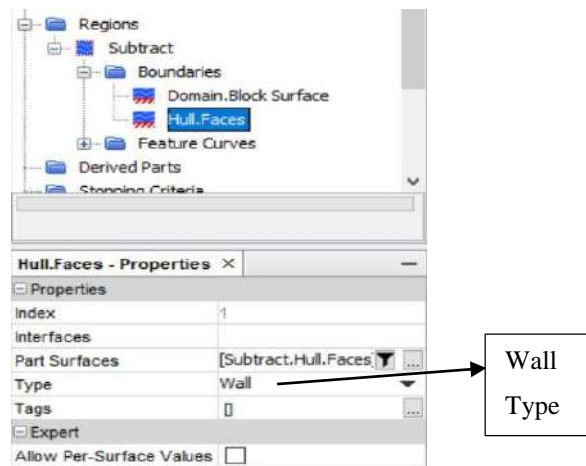
Activate the Subtract. In the Assign parts to region dialogue

- Select Create a region for each part
- Select Create a boundary for each part surface
- Select Do not create interface from contacts
- Apply and Close

Assigning Boundary Condition at each phase and on the hull surface

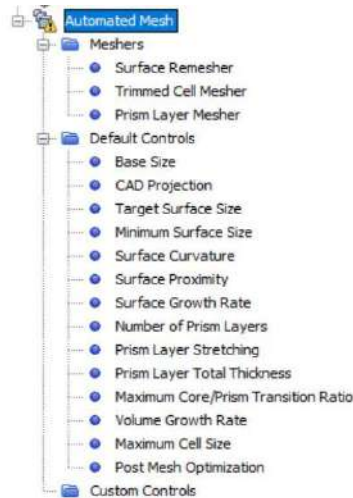
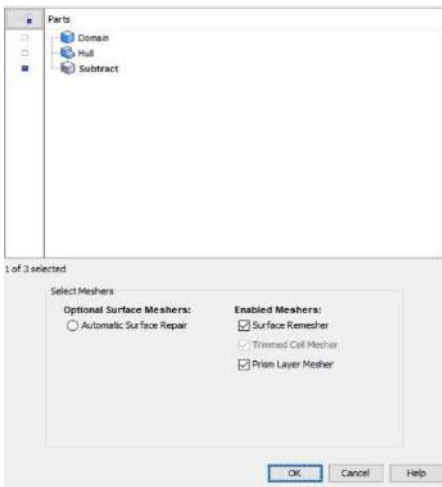
- Expand Region > Expanded Subtract > Expanded Boundaries
- Select Hull and in the properties select type as Wall, Similarly

Boundary	Type
Hull	Wall
Inlet	Velocity Inlet
Outlet	Pressure Outlet
Side	Symmetry
Symmetry	Symmetry
Top	Wall
Bottom	Wall



Generating the Volume mesh

- Expand Geometry > Right click on Operation > New > Mesh > Automated Mesh
- Select Subtract from the part
- Enable meshers:
 - ✓ Surface Remeshers
 - ✓ Trimmed Cell Mesher
 - ✓ Prism Layer Mesher



Global Mesh Setting

- Expand Geometry > Expand Operation > Expand Automated Mesh > Expand Default Controls and select the appropriate value.

Base Size	Hull Length / (40-60)
Target Surface Size	50
Minimum Surface Size	12.5
Number of Prism Layers	First Calculate the 1 st cell layer height from this Calculator . By doubling that get the thickness of 1 st layer perpendicular next to the solid wall. Using the stretching (geometric progression) factor (1.5) get the thickness of next layer and so on until the thickness get closer to the minimum surface size.
Prism Layer Stretching	1.5
Prism Layer Total Thickness	Sum up the thickness of all layers
Volume growth Rate	Default growth rate – Slow Surface growth rate - Slow
Maximum Cell Size	800

Keep all other setting as default values.

- Expand Geometry > Expand Operation > Expand Automated Mesh > Custom Control > Right click on Custom control > New > Surface Control

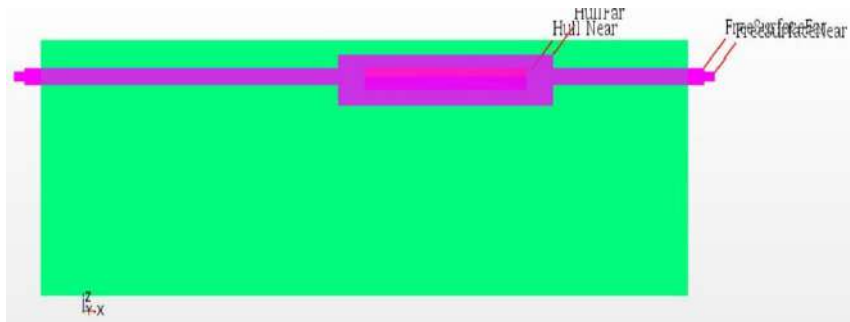
Do the work mentioned below as requirement

Surface Control	Control	Value
Part Surface: Hull	Target Surface Size: Custom	50
	Minimum Surface Size: Custom	25
Part Surface: Domain	Target Surface Size: Custom	800
	Minimum Surface Size: Custom	800
	Prism Layer: Disable	--

For mesh refinement create some rectangular block.

- Expand Geometry > Right click on part > New shape part > Block

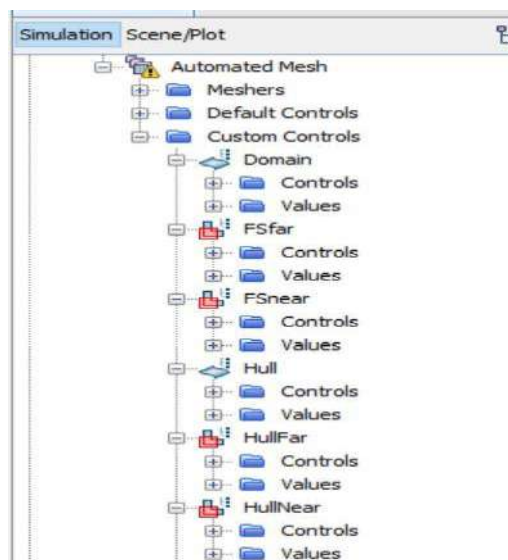
Small Block around the Hull	Set Corner 1 & 2
Large Block around the Hull	Set Corner 1 & 2
Thin Block around the free Surface position	Set Corner 1 & 2
Thick Block around the free surface position	Set Corner 1 & 2



- Expand Geometry > Expand Operation > Expand Automated Mesh > Custom Control > Right click on Custom control > New > Volumetric Control

Do the work mentioned below as requirement

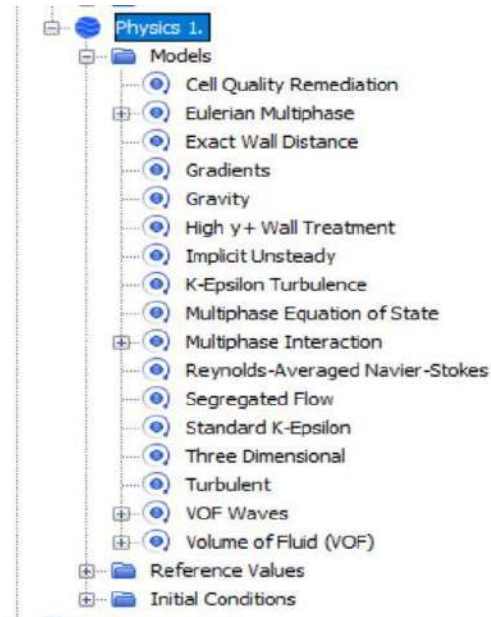
Volumetric Control	Control	Value
Part: Small Block	Trimmer: Customize anisotropic size	Relative X size: 50 Relative Y Size: 50 Relative Z Size: 100
Part: Large Block	Trimmer: Customize anisotropic size	Relative X size: 100 Relative Y Size: 100 Relative Z Size: 200
Part: Thin Block	Trimmer: Customize anisotropic size	Relative X size: 5 Relative Z Size: 10
Part: Thick Block	Trimmer: Customize anisotropic size	Relative X size: 12 Relative Z Size: 25



- Select Mesh > Generate Volume Mesh
The working process and the final total number of cells display in the output.
- After completing the volume mesh, right click anywhere in the geometry scene (right side) and Apply Representation > Volume Mesh.
The Volume mesh will be shown in the entire domain.

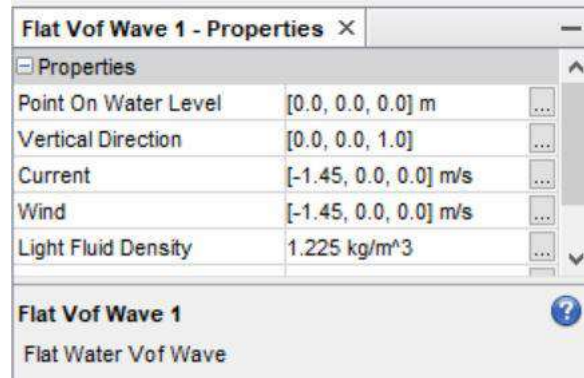
Physics Modeling

- Expand Continua > Expand Physics 1 > Right click on Model > Select Models
 - **Implicit Unsteady** from *Time* group
 - **Eulerian Multiphase** from *Material* group
 - **Volume of fluid (VOF)** from *Eulerian Multiphase Model* group
 - **Turbulent** from *Viscous Regime* group
 - **K-Epsilon Turbulence** from *Reynolds-Averaged Turbulence* group
 - **Standard K-Epsilon** from *K-Epsilon Turbulence Model* group
 - **High y+ wall treatment** from *K-Epsilon High y+ wall treatment* group
 - **Cell Quality Remediation, Gravity, and VOF Wave** from *Optional* group



- Expand Continua > Expand Physics 1 > Expand Models > Expand Eulerian Multiphase > Right click on Eulerian Phases > New > Rename Phase 1 as Water > Expand Water > Right click on Model > Select Models > Liquid from Material > Constant Density from Equation of State > Close
Again Expand Water > Expand Model > Expand Liquid (By default it is water) > put the values of Density and Dynamic Viscosity in the Material Properties.
- Expand Continua > Expand Physics 1 > Expand Models > Expand Eulerian Multiphase > Right click on Eulerian Phases > New > Rename Phase 1 as Air > Expand Air > Right click on Model > Select Models > Gas from Material > Constant Density from Equation of State > Close
Again Expand Air > Expand Model > Expand Gas (By default it is Air) > put the values of Density and Dynamic Viscosity in the Material Properties.

- Expand Continua > Expand Physics 1 > Expand Models > Expand VOF Waves > Right click on Waves > New > Flat
Select Flat VoF Wave 1 and give the values of Current and Wind as same in the accurate direction.



- Expand Continua > Expand Physics 1 > Expand Initial Conditions

Condition	Properties	
	Method	Scalar Function
Pressure	Field Function	Hydrostatic Pressure of Flat Vof Wave 1
Velocity	Field Function	Velocity of Flat Vof Wave 1
Composite: Water	Field Function	Volume Fraction of Heavy Fluid of Flat Vof Wave 1
Composite: Air	Field Function	Volume Fraction of Light Fluid of Flat Vof Wave 1

Setting up Damping option to avoid wave reflection from boundaries

- Expand Region > Expand Subtract > Expand Physics Conditions > VOF wave zone option and selected Damping.
- Expand Physics Value > VOF wave damping length > Put 2 to 3 times of wavelength.

Setting Boundary condition under the Region

- Expand Region > Expand Subtract > Expand Boundaries > Inlet > Physics Conditions > Velocity Specifications and select method to components
- Expand Region > Expand Subtract > Expand Boundaries > Inlet > Physics Conditions > VOF wave damping boundary option and select method to Yes.
- Physics Values > Velocity > Selected method to Field Function and select Velocity of Flat Vof Wave 1 as Vector function
- Volume Fraction > Composite > Water > Method to Field Function and Volume Fraction of Heavy of Flat Vof Wave 1 as Function

Similarly for the rest of the boundaries.

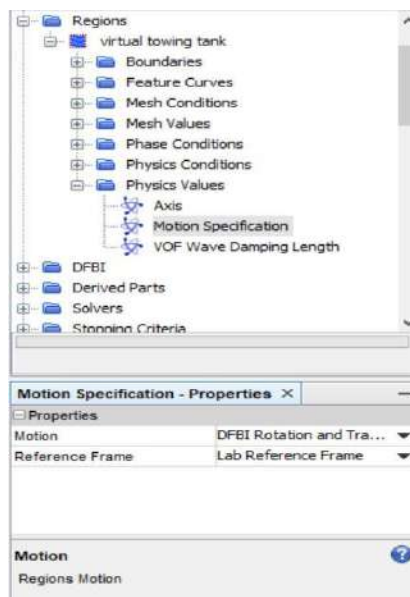
Boundary	Physics Conditions	Method	Physics Values	Method	Scalar Function
Outlet	Vof Wave Damping Boundary Option	Yes	Pressure	Field Function	Hydrostatic Pressure of Flat Vof Wave 1
			Volume Fraction: Water	Field Function	Volume Fraction of Water
			Volume Fraction: Air	Field Function	Volume Fraction of Air
Side	Vof Wave Damping Boundary Option	Yes	--	--	--
Symmetry	Vof Wave Damping Boundary Option	No	--	--	--
Top	Shear Stress Specifications	Slip	--	--	--
	Vof Wave Damping Boundary Option	No	--	--	--
Bottom	Shear Stress Specifications	Slip	--	--	--
	Vof Wave Damping Boundary Option	No	--	--	--

For the hull boundary/Surface kept all the values as Default values.

Setting Dynamic Fluid Body Interaction (DFBI) model

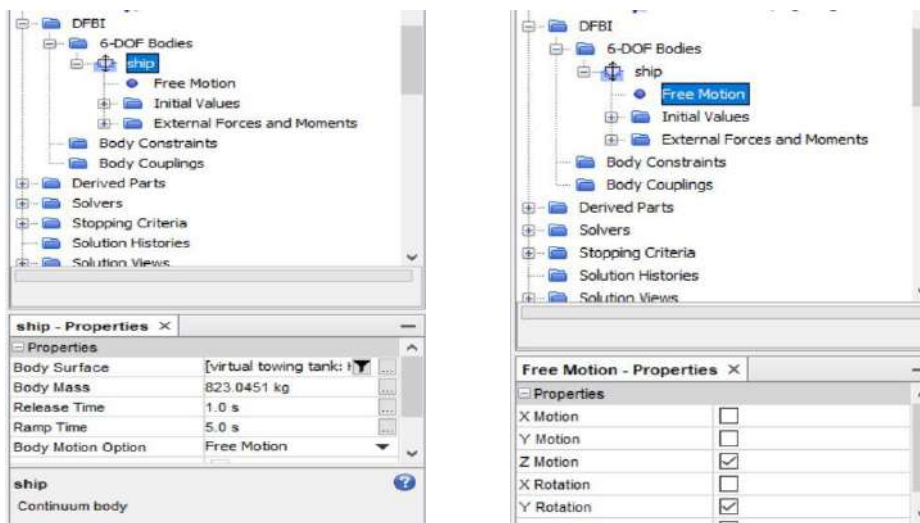
DFBI module simulate the free motion in response to the fluid force and moment act on the body.

- Expand Tools > Right click on Motions > Select DFBI Rotation and Translation
- Expand Regions > Expand Subtract > Expand Physics Values > Motion Specification and Select Motion to DFBI Rotation and Translation

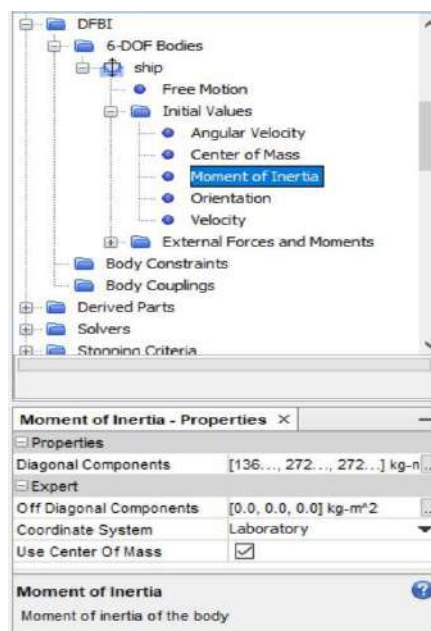


Assigning the Ship Hull in DFBI module

- Expand DFBI > Right Click on 6 DOF Bodies > New Body > 3D > Continuum Body > Rename the body as Ship
- Select Ship and in the properties put the values
 - ✓ Body Surface: Click on [...] and select all the hull boundary surface (if there are more than one)
 - ✓ Body Mass: Half of the mass of the hull
 - ✓ Release Time: 1 sec
 - ✓ Ramp Time: 5 sec
- Select Free Motion > In the properties activate Z motion and Y rotation. (Calculated Sinkage and Trim)



- Expand Initial Values > Select Center of mass and put the xyz coordinate > Select Moment of Inertia and put Diagonal Components values and also activate Use Center of mass



Solver Setting

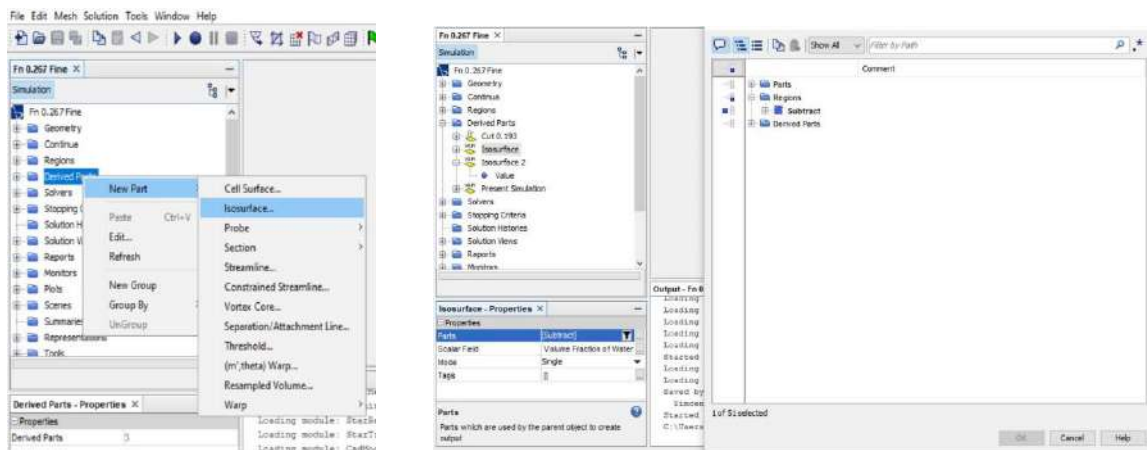
- Solvers > Implicit Unsteady > Set time step to 0.03 sec
- 6 DOF solver > Maximum number of Iterations equal to 5
- Segregated Flow > Velocity > Under-Relaxation factor equal to 0.7
- Segregated Flow > Pressure > Under-Relaxation factor equal to 0.4
- Segregated VOF > Single-step > Under-Relaxation factor equal to 0.8
- K-Epsilon Turbulence > Under-Relaxation factor equal to 0.8

Stopping Criteria

- Maximum Inner Iterations equal to 10 and activate the Enabled box.
- Maximum physical time equal to 200 sec and activate the Enabled box.
- Deactivate the Enabled box in the maximum steps.
- Activate the Enabled box in the stop File.

Creating the Iso Surface

- Right click on Derived Parts > New > Iso Surface
- In the part selected only Subtract under the Region, in the scalar field select Volume fraction of water and select the iso value equal to 0.5.

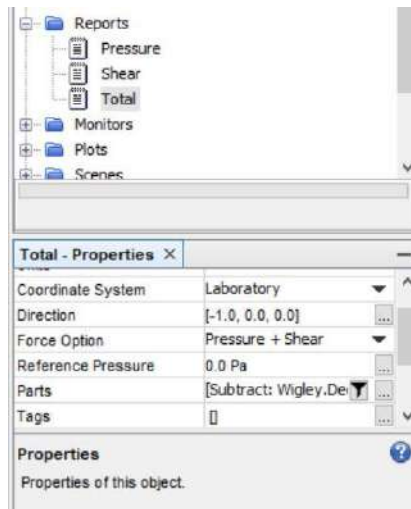


- Create another Iso surface (Rename it as **Present Simulation**) and in this time select all the boundaries associated with the hull body. Select volume fraction of water in the scalar field and put 0.5 in the Iso value.



Generating the Report

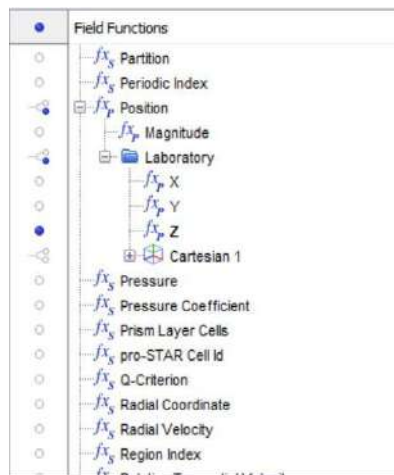
- Right click on Report > New Report > Force (rename it as Pressure force). Select this pressure force and in the properties
 - ✓ Set direction to the direction of flow [-1.0, 0.0, 0.0]
 - ✓ Set Force option to Pressure
 - ✓ Set parts to all the hull boundary surfaces.
- Copy and paste this pressure force twice (One for shear and another for Total Force). For shear force just set the force option to shear and for total force set the force option to shear + pressure.



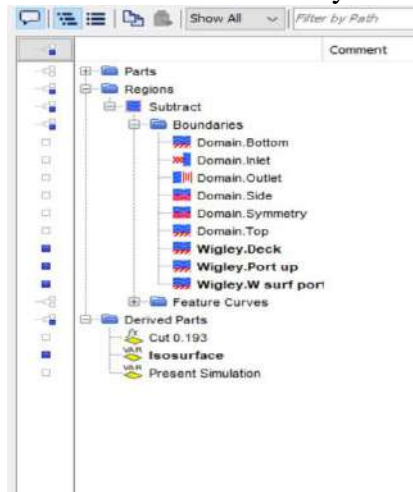
- Right click on Report > New Report > 6 DOF Body Orientation (rename it as Trim). Select this Trim and in the properties
 - ✓ Set Angle Report Option to Rotation Y axis
 - ✓ Activate Constrained angle Range
- Right click on Report > New Report > 6 DOF Body Translation (rename it as Sinkage). Select this Sinkage and in the properties
 - ✓ Set Direction to [0.0, 0.0, 1.0]

Making the Wave Contour Scene

- Right Click on Scene > New Scene > Scalar (Rename it as Wave)
- Expand Wave > Expand Displayers > Scalar 1
 - ✓ Set Contour Style to Smooth Filled + Lines
 - ✓ Set Transform to Symmetry 1
- Scalar 1 > Parts > Select the Iso Surface as Parts
- Scalar 1 > Scalar Field > Select Position [Z] as Function



- Outline 1 > Deactivate the Outline
- Outline 1 > Parts > Select all the hull boundary surface plus the iso surface



Plotting the Results

- Expand Reports > Multi Select Shear and Pressure and Right Click > Create Monitor and Plot from Report > Single Plot > Under the Plots rename it as Shear and Pressure Force.
- Reports > Right Click on Total Force > Create Monitor and Plot from Report > Under Plot rename it as Total Force.
- Expand Reports > Multi Select Trim and Sinkage and Right Click > Create Monitor and Plot from Report > Single Plot > Under the Plots rename it as Time and Sikage.

Before plotting Wave profile do some necessary steps

- Tools > Field Function > New > Scalar > User Field Function 1 > Rename as 2x/L
 - ✓ Function name to 2x/L
 - ✓ Definition to $((\$Position[0]*2)/-3)$ {Normalize the x coordinate by length of the hull}
- Tools > Field Function > New > Scalar > User Field Function 1 > Rename as h/L
 - ✓ Function name to h/L
 - ✓ $((\$Position[2])/3)$ { Normalize the wave height by length of the hull}
- Right click on Plots > New Plot > XY Plot (Rename it as Wave profile along the hull)
 - ✓ Rename Title as Wave profile along the hull
 - ✓ Parts to New Simulation (Already created in the derived parts as Iso surface)
 - ✓ X Type: Data type to scalar and Scalar function to 2x/L
 - ✓ Y Type: Data type to scalar and Scalar function to h/L

Save and Run the Simulation.

